NTNU – Trondheim
Norwegian University of
Science and Technology

Importance of Fluid-Structure Interaction on Dropped Lifeboats

A parametric study used to explore the importance of hydroelasticity on complex low rigidity structures using decision factors

Michael Piccard Handeland

Marine Technology
Submission date: June 2015
Supervisor: Sverre Steen, IMT
Co-supervisor: Jon Tøndevoldshagen, Fedem Technology AS

Norwegian University of Science and Technology
Department of Marine Technology

Abstract

Experimental methods have previously been used in the design of lifeboats; this approach is both time-consuming and expensive. The experimental approach is suitable to find the loads and accelerations on an existing design; however, it is not very useful for the development of a new design. In order to continue the innovation and development of lifeboat design there has been a shift towards the application of numerical tools. Today, Computational Fluid Dynamics (CFD), Finite Element Analysis (FEA), model and full-scale experiments are used in research, investigation and development of lifeboats. The use of CFD and FEA is increasing and there has been demonstrated a general good agreement between numerical results and full-scale tests. However, the elastic deformations on the hull during impact are normally ignored and the validity of this simplification is questioned since large deformations have been observed. A possible solution to this problem is to perform Fluid-Structure Interaction (FSI) analysis, where CFD and FEA are coupled. Today, the most common procedure is to use the pressure from the CFD analysis as boundary conditions for the FEA analysis. With this approach the deformations during impact are ignored. A more robust, but expensive, solution is to perform a two-way interaction analysis where information is exchanged between the CFD-domain and FEM-domain during the analysis. In this way the deformation during impact is addressed. For lifeboats, this method is most applicable during slamming or more specifically when hydroelasticity occurs. Hydroelasticity is a phenomenon which is propagated in the structure as fast vibrations, which will alter the dynamic loading and boundary condition on the structure.

The overall purpose of this thesis is to explore the importance of fluid-structure interaction, or hydroelasticity, on lifeboats. Specifically, the goal is to explore when it is important to account for hydroelasticity for complex low rigidity structures using decision factors. By exploring decision factors, one can more easily understand if it is necessary to account for hydroelasticity in numerical simulations. The main body of work has been divided into two main tasks: 1) A verification study and 2) a parametric study of different impact velocities, deadrise angles and material properties, in order to explore the importance of hydroelasticity using decision factors.

A brief introduction to the theory behind CFD and FEA is presented along with fluid-structure interaction and different coupling algorithms. Hydroelasticity is described and multiple decision factors are presented.

In this thesis, Star-CCM+, developed by CD-Adapco, is used in the CFD calculation while Abaqus, developed by Simula, is used in the FEA calculations. A co-simulation engine developed by Simula couples the two softwares together in order to exchange information. Star-CCM+ transfers the pressure and wall shear stress to Abaqus while Abaqus transfers the nodal

displacements to Star-CCM+.

In order to verify that these two softwares were able to recreate a hydroelastic event, a verification study of a full-scale test was performed. A full 3D FEA model and a full-scale test report were supplied by the manufacturer. A 3 meter free-fall drop test of a conventional lifeboat was performed, where the acceleration on multiple places on the boat was measured. The model was reduced to 2D and altered with respect to geometric stiffness using springs and additional mass. Convergence studies for both FEA and CFD were performed. The mass was tuned in such a way that the maximum acceleration in 2D would be equal to the maximum acceleration in 3D, this is necessary due to the pressure distribution in 3D. The acceleration from the co-simulation was compared to the acceleration at the same location in the full-scale test. The results are in good agreement with the test results and they yield approximately the same maximum acceleration and oscillation period even though the mass have been tuned. From the spectrum of the pressure time series we can observe that a hydroelastic event was recreated as we can observe several distinctive peaks. We can also see from the pressure time series the pressure oscillations which are associated with hydroelasticity. The results are considered satisfactory and it is believed that the method can be trusted.

A total of 120 simulations were performed with a range of six different deadrise angles, five impact velocities and four different material properties in the parametric study. In addition, 16 models with the verification study model are simulated where only the impact velocity is altered. The maximum strain in a node in a platefield was evaluated. The results demonstrates a clear trend that was consistent with previously published articles. As the deadrise angles decreases, the impact velocity increases, and the stiffness decreases, the importance of hydroelasticity will increase. The decision factor R_B defined in Bereznitski (2001) predicts that the response should be hydroelastic, while the factor R_F defined in Faltinsen (1999b) predicts that the response should almost be quasi-static. The quasi-static strains is found using Euler-Bernoulli beam theory. According to the results, all the simulations are dominated by hydroelasticity; hence R_B is the best suited decision factor for this problem. It is also observed that the when the importance of hydroelasticity increases, the maximum strain in the plate decreases in relationship to the quasi-static strain.

Error sources are discussed and it was discovered that the simulations are unstable, due to the fact that a repetition study yields a different maximum strain, while the profile of the strain time history is very similar. The uncertainty of the results was studied and it was discovered that the uncertainty for the mean of the nine simulations are 10.8 % within 95 % confidence interval. The main reasons are assumed to be the interaction with the eigenmode introduced by the springs, the presence of bifurcation points, and the capabilities of the implicit dynamic solver in Abaqus. Although instabilities and an uncertainty are observed, the results are regarded as representative and the model is able to describe hydroelastic events. This conclusion is supported by Faltinsen (2005) as he observed some variance for the strain when an experiment was performed with a given impact velocity.

The influence on the point of flow separation is investigated by applying different viscous models. It is concluded that the point of flow separation is not affected by different viscous models as the flow follows the hull and only separates at the edge. The effect from different viscous

regimes cannot be clearly observed on the translation, velocity or acceleration of the hull. This can be explained due to the fact that the pressure time history is fairly similar and only small differences in the magnitude of the pressure exist, this is not significant as it is the impulse of the slamming load which is important for the response. It is concluded that the difference from a laminar flow to a turbulence model is negligible.

Further work is also discussed.

Sammendrag

Tidligere ble kun eksperimentelle metoder brukt i design av livbåter, men denne tilnærmingen er dessverre både tidkrevende og dyr. Den eksperimentelle tilnærmingen kan også kun brukes til å finne laster og akselerasjoner på eksiterende design og er ikke veldig nyttig i utviklingen av nye design. For å fortsette innovasjon og utvikling av livbåter har det oppstått en retningsendring mot å bruke numeriske metoder. I dag er Computational Fluid Dynamics (CFD), Finite Element Analysis (FEA), modell- og full-skalaeksperimenter brukt i forskning og utvikling av livbåter. Bruken av CFD og FEA er økende og det har blitt demonstrert god overenstemmelse mellom numeriske resultater og fullskala forsøk. Normalt er elastiske deformasjoner på skroget under kollisjon med vannet ignorert og gyldigheten av denne forenklingen er tvilsom ettersom det har blitt observert store deformasjoner i forsøk. En mulig løsning på dette problemet er å utføre Fluid-Struktur-Interaksjons (FSI) analyse, hvor CFD og FEA blir koblet sammen. I dag er det mest vanlig å bruke trykket fra en CFD-analyse som randbetingelser for FEA-analysen, med med denne tilnærmingen blir deformasjonen under kollisjon med vannet ignorert. En bedre løsning som er mer kostbar beregningsmessig er å utføre en to-veis interaksjonsanalyse hvor informasjon blir utvekslet mellom CFD- og FEA-løsningen under analysen. På denne måten blir deformasjonene under kollisjonen tatt hensyn til. For livbåter er denne metoden mest relevant når den opplever kollisjon med vann, eller mer spesifikk: når hydroelastisitet oppstår. Hydroelastisitet er et fenomen hvor strukturen opplever raske vibrasjoner som vil endre den dynamiske lasten og randbetingelsene på strukturen.

Hensikten med denne oppgaven er å utforske viktigheten av fluid-struktur-interaksjon, hvilket innebærer å finne ut når det er viktig å ta hensyn til hydroelastisitet for komplekse lav-stivhetsstrukturer i numeriske simuleringer ved hjelp av beslutningsparametere. Ved å utforske beslutningsparametere kan man enklere få en forståelse for når det er nødvendig å ta hensyn til hydroelastisitet i numeriske simuleringer. Først vil en verifikasjonstudie bli gjennomført og deretter en parameterstudie hvor kollisjonhastigheten, dødreisvinkelen og materialegenskapene vil bli endret. Her vil viktigheten av hydroelastisitet bli utforsket med hjelp av beslutningsparametere.

En kort introduksjon til teorien bak CFD og FEA vil bli presentert sammen med FSI og forskjellig koblingsalgoritmer. Hydroelastisitet vil bli beskrevet, samt flere beslutningsparametere.

I denne oppgaven blir Star-CCM+, utviklet av CD-Adapco, brukt i CFD-beregninger, mens Abaqus, utviklet av Simula, blir brukt i FEA-beregninger. En ko-simuleringsmotor som er utviklet av Simula kobler de to programmene sammen slik at informasjon kan bli utvekslet mellom dem. Star-CCM+ overfører trykk og skjærkrefter til Abaqus, mens Abaqus overfører node-deformasjoner.

For å verifisere at de to programmene er i stand til å gjenskape en hydroelastisk hendelse vil en verifikasjonsstudie bli gjennomført. I denne studien vil en fullskala test bli forsøkt gjenskapt. Det ble gitt tilgang til en 3D FEA-modell og en fullskala testrapport. Disse ble brukt for å gjenskape et 3 meters frittfallslipp av en konvensjonell livbåt, hvor akselerasjonen flere steder i båten ble målt. Modellen ble redusert til 2D og modifisert med hensyn på geometrisk stivhet (ved hjelp av fjærer) og tilleggsmasse. Konvergensstudier for både CFD og FEA har blitt gjennomført. Tilleggsmassen er endret slik at den maksimale akselerasjon i 2D er lik den maksimale akselerasjonen i 3D, dette er nødvendig på grunn av fordeling av trykk i fullskala. Akselerasjonen fra simuleringen blir sammenlignet med akselerasjon fra fullskalatesten. Resultatene er i overensstemmelse med testresultatene og de viser omtrent samme maksimale akselerasjon og svingeperiode. Fra spekteret av tidsserien av trykket kan vi observere at en hydroelastisk kollisjon har blitt gjenskapt, ettersom det viser flere distinkte frekvenser. Resultatene blir ansett som tilfredsstillende og det menes at metoden kan stoles på.

Total er det simulert 120 forskjellige caser med seks forskjellige dødreisvinkler, fem kollisjonhastigheter og fire forskjellige materialegenskaper i parameterstudien. I tillegg er 16 simuleringer gjennomført med verifikasjonsmodellen hvor kun kollisjonhastigheten er endret. Den maksimale tøyningen i en node i et platefelt er evaluert. Resultatene viser en klar trend som er i samsvar med tidligere presentert forskning. Jo høyere hastighet, jo lavere dødreisvinkel og jo mykere materiale, jo viktigere blir hydroelastisitet. Resultatene viser at beslutningsfaktoren R_B som er definert i Bereznitski (2001) forutsier at responsen skal være dominert av hydroelastisitet, mens faktoren R_F definert i Faltinsen (1999b) forutsier at responsen snart burde være kvasi-statisk. De kvasi-statiske tøyningen er funnet ved hjelp av Euler-Bernoulli bjeketeori. I henhold til resultatene er responsen dominert av hydroelastisitet. Dermed blir R_B ansett for å være den beste egnet besultningsparameteren for dette problemet. Vi kan også observere at når viktigheten av hydroelastisitet øker vil den maksimale tøyningen i platen minke i forhold til den kvasi-statiske tøyningen.

Feilkilder er diskutert og det er oppdaget at simuleringene er ustabile ettersom en repetisjonstudie gir forskjellig maksimal tøyning, selvom profilen til de to simuleringene er veldig like. Det blir oppdaget at usikkerheten til gjennomsnittet av ni simuleringer er 10.8 % innenfor et 95 % konfidensintervall. Hovedgrunnene er antatt til å være interaksjon med egenmodene til fjærene, tilstedeværelsen av bifurkasjonspunkter og begrensinger til den dynamisk implisitte løseren i Abaqus. Selv om ustabilitetene er tilstede og en usikkerhet eksisterer blir resultatene ansett for å være korrekte og at modellen kan beskrive hydroelastisk kollisjon. Dette blir også støttet av Faltinsen (2005) ettersom han observerte en varians i målte tøyninger i en eksperimentell serie med en gitt kollisjonshastighet.

Påvirkningen på separasjonspunktet ved bruk av forskjellige viskøse modeller er også studert. Det blir konkludert at separasjonspunktet ikke blir påvirket av forskjellige viskøsemodeller ettersom strømningen følger skroget og kun separerer ved kanten. Effekten fra forskjellige viskøsemodeller er ikke veldig klar på forskyvningen, hastigheten og akselerasjonen på skroget. Dette kan bli forklart ut ifra trykktidsserien, ettersom de er relativt like og det kun eksisterer små forskjeller i størrelsen på trykket vil ikke dette påvirke skroget i en stor grad ettersom det er impulsen som er viktig for responsen under kollisjon med vann. Det blir konkludert med at

forskjellen mellom laminær strømning og turbulent strømning er neglisjerbar.

Videre arbeid blir også diskutert.

Preface

This thesis is the result of individual work performed in the spring semester of 2015, and is a continuation of the project thesis delivered during the autumn semester of 2014. This master thesis is the final part of the requirement to gain a Master of Science degree in Marine Technology with a specialization within Marine Hydrodynamics taken at Norwegian University of Science and Technology.

This work has been performed at the Norwegian University of Science and Technology, Department of Marine Technology, Trondheim and at Fedem Technologies, Trondheim. This work have been conducted with Professor Sverre Steen (NTNU) and Jon Tøndevoldshagen (Fedem) as supervisors.

The master thesis has been very challenging. I met great challenges when trying to reduce the problem from 3D to 2D and find the correct mass for the 2D-section. In the parametric study, I met many challenges with respect to stability in the co-simulation. I have spent over 5500 hours of simulation time during the semester and countless more hours post-processing the results. The numerical models are attached as electronic attachments and are briefly described in appendix H.

I would like to thank Sverre Steen (NTNU) for pointing me in the right direction and giving advice. I would also like to thank Asle Heide Vaskinn (Fedem) and Thomas Børvik Johnsen (Fedem) for giving me insight into FSI-simulations and much needed help along the way. Employees at Fedem also deserve my thanks, as they have helped me with various problems and gave me valuable insight into the programs. Lastly, I would like to extend my gratitude to the manufacturer, who gave me access to the test report and FEM model. A special thanks goes the support crew at CD-Adapco, who helped me gain a deeper understanding of the co-simulation engine for the coupled analysis. At last would I like to thank Erin Thomas for proofreading my thesis.

It is assumed that the reader has basic knowledge in fluid mechanics, structural mechanics and numerical simulations.

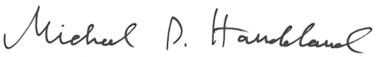

Michael Piccard Handeland
Trondheim, 08-06-2015

Scope of Work

NTNU Trondheim
Norwegian University of Science and Technology
Department of Marine Technology

MASTER THESIS IN MARINE TECHNOLOGY

SPRING 2015

FOR

Michael Piccard Handeland

Importance of fluid-structure interaction for impact loads on dropped lifeboats

Loads and responses of lifeboats used on offshore oil & gas installations has been a hot topic of research and investigations for several years, after it was discovered large structural deformations and unacceptably high acceleration levels in existing free-fall lifeboats. Both CFD, FEM and model and full scale experiments are used in the research and investigation of the performance of the lifeboats. The combination of CFD and FEM is increasingly in favor, and it has been demonstrated that generally good agreement between calculation and full scale measurements is obtained. However, the influence of elastic deformations of the hull structure from the hydrodynamic loads during impact is ignored in most numerical analyses, and the validity of this simplification is questioned in some cases, where large structural deformations are observed in full scale measurements.

The master thesis is a continuation of the project thesis, where the Fluid-Structure Interaction (FSI) on a dropped wedge was investigated using coupled calculations in Star CCM+ and Abaqus. The results were compared to experimental results with good agreement.

In the master thesis, the focus will be shifted from free-fall lifeboats to traditionally launced lifeboats. These boats need to be able to sustain a free drop of three meters, and large deformations of the hull have been measured in full scale during such drops. Due to the geometry and the way the boats are dropped, the problem is well suited for a 2-D study.

Therefore the main objectives of the proposed master thesis are:

- To determine the importance of fluid-structure interaction for the loads and deformations of the hull of dropped lifeboats. The result shall be validated against experiments as far as possible (limited by the availability of high-quality experimental results)
- To do a parametric study to determine how various geometric parameters influence the results and importance of FSI. The candidate will, in discussion with his supervisors, decide which parameters, but it is expected that deadrise angle will be one.

It is recommended to investigate the importance of flow separation point on the round bilge of these boats.

It is assumed that Star CCM+ will be used for CFD and Abaqus for FEM. The topic is proposed by Fedem Technologies, and people from Fedem will provide guidance to the candidate.

In the thesis the candidate shall present his personal contribution to the resolution of problem within the scope of the thesis work.

Theories and conclusions shall be based on mathematical derivations and/or logic reasoning identifying the various steps in the deduction.

NTNU Trondheim
Norwegian University of Science and Technology
Department of Marine Technology

The thesis work shall be based on the current state of knowledge in the field of study. The current state of knowledge shall be established through a thorough literature study, the results of this study shall be written into the thesis. The candidate should utilize the existing possibilities for obtaining relevant literature.

The thesis should be organized in a rational manner to give a clear exposition of results, assessments, and conclusions. The text should be brief and to the point, with a clear language. Telegraphic language should be avoided.

The thesis shall contain the following elements: A text defining the scope, preface, list of contents, summary, main body of thesis, conclusions with recommendations for further work, list of symbols and acronyms, reference and (optional) appendices. All figures, tables and equations shall be numerated.

The supervisor may require that the candidate, in an early stage of the work, present a written plan for the completion of the work. The plan should include a budget for the use of computer and laboratory resources that will be charged to the department. Overruns shall be reported to the supervisor.

The original contribution of the candidate and material taken from other sources shall be clearly defined. Work from other sources shall be properly referenced using an acknowledged referencing system.

The thesis shall be submitted electronically (pdf) in DAIM:

- Signed by the candidate
- The text defining the scope (signed by the supervisor) included
- Computer code, input files, videos and other electronic appendages can be uploaded in a zip-file in DAIM. Any electronic appendages shall be listed in the main thesis.

The candidate will receive a printed copy of the thesis.

Supervisor	: Professor Sverre Steen
Advisor	: Jon Tøndevoldshagen (Fedem)
Start	: 15.01.2015
Deadline	: 10.06.2015

Trondheim, 15.01.2015

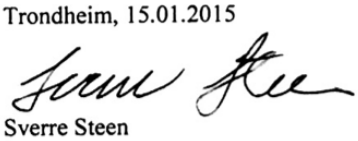

Sverre Steen
Supervisor

Contents

List of Figures

List of Tables

List of Symbols

Symbol	Units	Description
$\mathbf{u}$	$\mathrm{m\,s^{-1}}$	velocity vector
p	Pa	pressure
ρ	$\mathrm{kg\,m^{-3}}$	density
T	K	temperature
$\vec{V}$	$\mathrm{m\,s^{-1}}$	velocity vector
$\vec{g}$	$\mathrm{m\,s^{-2}}$	gravitational vector
μ	Pa s	dynamic viscosity
∇	-	difference operator
A	-	coefficient matrix
u	-	vector of unknowns
b	-	vector of known values
Δt	s	time step
Δx	m	mesh size in x-direction
Δy	m	mesh size in y-direction
Δx	m	mesh size in z-direction
V	$\mathrm{m^3}$	volume
S	$\mathrm{m^2}$	surface
$\mathbf{v}_b$	-	controle volume velocity
$\mathbf{n}$	-	normal vector
T	-	stress tensor
I	-	identity matrix
ϕ	-	scalar
Γ	$\mathrm{m^2\,s^{-1}}$	diffusivity coefficient
$\mathbf{b}_\phi$	-	source or sink of ϕ
α	-	volume fraction
ε	-	strain
$\mathbf{u}$	m	displacement vector
∇_s	-	difference operator
$\mathbf{b}$	N	body force
σ	Pa	stress
E	Pa	young's modulus
D	-	material matrix
K	-	stiffness matrix

r	m	nodal displacement
Q	N	external forces
δu	m	virtual displacement
$\mathbf{X}$	N	body forces
$\mathbf{T}$	N	surface tractions
$\mathbf{Q}$	N	load vector
δr	m	virtual nodal displacement
$\delta \varepsilon$	-	virtual strain
F^I	N	inertia force
$\ddot{u}$	$\mathrm{m\,s^{-2}}$	acceleration
N	-	interpolation functions
v	m	element nodal displacement
B	-	strain-nodal displacement relationship matrix
δv	m	virtual element nodal displacement
S	N	element force
k	-	element stiffness matrix
m	-	element mass matrix
P	-	element distributed load vector
K	-	system stiffness matrix
M	-	system mass matrix
C	-	system damping matrix
R_F	-	hydroelastic factor by Faltinsen (1999b)
R_B	-	hydroelastic factor by Bereznitski (2001)
R_P	-	hydroelastic factor by Panciroli (2005)
α	-	deadrise angle
β	-	deadrise angle (used in figures from various articles)
V	$\mathrm{m\,s^{-1}}$	impact velocity
L	m	length
I	m	second area of moment
h	m	thickness of plate
ρ_w	$\mathrm{kg\,m^{-3}}$	density of water
$\bar{m}$	-	mass matrix
D_x	-	material matrix in x-direction
D_y	-	material matrix in y-direction
B	-	coupled material matrix
ν	-	Poisson's ratio
ω_n	Hz	eigenfrequency
ϕ	-	eigenshape
F	N	force/load
P	Pa	pressure
q	Pa	pressure load
w	m	displacement
β	-	under-relaxation factor
$\tilde{w}$	m	unrelaxed displacement

G	Pa	shear modulus
α	-	mass material damping in Rayleigh damping
β	-	stiffness material damping in Rayleigh damping
duration	s	load duration used in R_B
period	s	first dry eigenperiod used in R_B
m	kg	mass
M	kg	mass
D	$\mathrm{N\,m^2}$	flexural stiffness or bending stiffness
T	s	eigenperiode
ε_m	-	maximum strain
Z_a	m	height
S	$\mathrm{m^3}$	sectional Modulus
m_{eq}	kg	equivalent mass
a	$\mathrm{m\,s^{-2}}$	acceleration
s	m	displacement
k	$\mathrm{N\,m^{-1}}$	spring stiffness
q	$\mathrm{N\,m^{-1}}$	distributed load
z	m	distance from the neutral axis
N	-	number of samples in the population
$\bar{\varepsilon}$	-	mean maximum strain
S_ε	-	standard deviation of the population
P_ε	-	precision limit for a single sample in the population
U_ε	-	uncertainty of a single sample in the population
$S_{\bar{\varepsilon}}$	-	standard deviation of the mean of the population
$P_{\bar{\varepsilon}}$	-	precision limit for the mean of the population
$U_{\bar{\varepsilon}}$	-	uncertainty for the mean of the population
t	-	value of the inverse t-distribution cumulative density function

List of Abbreviations

PDE	-	Partial Differential Equations
NS	-	Navier-Stokes
FVM	-	Finite Volume Method
RANS	-	Reynolds Averaged Navier Stokes Equation
ULS	-	Ultimate Limit State
ALS	-	Accidental Limit State
FEM	-	Finite Element Method
FEA	-	Finite Element Analysis
CFD	-	Computational Fluid Dynamics
FSI	-	Fluid-Structure Interaction
PTIL	-	Petroleum Safety Authority Norway
EFD	-	Experimental Fluid Dynamics
CFL	-	Courant-Fredrichs-Levi number

Chapter 1

Introduction and Motivation

Lifeboats are an essential part of any ship or offshore installation. The maritime and offshore industry have a huge focus on HSE (Health Safety Environment). It is therefore paramount that the lifeboats provide the safety they represent, even under extreme conditions. They are objects that we hope to never use, but when it is needed do they need to be working perfectly. Free-fall and conventional lifeboats are the last means of evacuation should a hazardous situation arise, (PTIL, 2014). This means that they are very important for the safety of the passengers and crew members' on board ships and offshore installations. The lifeboat must be designed in such a way that it can quickly and safely evacuate people. This means that a lifeboat must have sufficient structural integrity during impact, and is able move away from the vessel or installation after water entry and water exit. The lifeboat must fulfil certain requirements as defined in DNV-OS-E406 and Standard for Certification No.2.20 by DNV GL. These standards relate to structural integrity, water exit path, and accelerations.

In 2005, testing was performed on the free-fall lifeboats installed on Veslefrikk B in the North Sea. Severe damage was observed in the deck house of one of the lifeboats. A short time after, the same occurred on the Kristin field. After these incidents, the industry and the regulatory authority (PTIL) realized that something must be done. The industry established a project that revealed a vast number of weaknesses with existing lifeboat designs, (PTIL, 2014). It was quickly established that technical solutions for lifeboats were based upon rules and regulations that were not adapted for the harsh environment of the North Sea, (PTIL, 2014). This is due to the fact that lifeboats need to be operational under any weather condition. It has been revealed that the main issues with the lifeboat design relate to the structural strength of the deck house and hull, experienced G-forces for the passengers, propulsion and stability, (PTIL, 2014). As a consequence a limit exists for the number of people each lifeboat is able to evacuate. Thus does the installation need to operate with reduced manning during harsh weather conditions. This can have an impact on the safe operation on the installation, (PTIL, 2014). A free-fall lifeboat can be viewed in Figure 1.1.

Experimental methods have previously been used in design of lifeboats. In order to recreate the vast number of possible configurations with respect to weather conditions, the designer was relying on a vast number of tests. This is both time-consuming and expensive. However, the experimental approach is only suitable to find loads and accelerations on existing design and

Figure 1.1: Free-fall lifeboat installed on an offshore installation, (PTIL, 2014)

not very useful for the development of a new design, (Johannessen, 2012). In order to continue the innovation and development of lifeboats, there has been shift towards applying numerical tools in the design process.

Today, Computational Fluid Dynamics (CFD), Finite Element Analysis (FEA) along with model and full-scale experiments are used in research, investigation and development of lifeboats. The use of CFD and FEA is increasing. Normally, the pressure and shear forces from the CFD-solution act as boundary condition for the FEA model. Even though there has been demonstrated good agreement between simulations and full scale measurements, some concerns have been raised, mainly due to the fact that elastic deformation of the hull from the hydrodynamic loads during impact has been ignored in most numerical simulations. This simplification is in question because large structural deformations have been observed in full scale measurements. The problem arises because there exists a strong coupling between the structural solution and hydrodynamic solution that should be addressed during the simulation. This coupling appears for a wide range of problems and has been noted Fluid-Structure Interaction (FSI). The basis of numerical FSI is to perform a coupled analysis, where information is exchanged between the two "worlds" (hydrodynamic (CFD) and structural (FEA)) during the simulation. This can either be a one-way or two-way communication. This will lead to a significant increase in computational time and load. The two codes will now be running at the same time and data is transferred between them. Hence is it beneficial to find out when fluid-structure interaction is important and should be accounted for.

When an elastic body experiences impact with water, the body experiences a phenomenon referred to as hydroelasticity. This is a vibration problem that will alter the dynamic loads and the boundary condition of the body. The topic of hydroelasticity has been widely studied with both experimental, analytical and numerical methods in Kapsenberg (2011) and Faltinsen (2000). Analytical methods are able to find general trends which fit well with experiments as shown in Faltinsen (1999b). There have been great advances in the development of numerical FSI algorithms and numerical FSI is now considered to be a good alternative. Good numerical results have been achieved and validated with experiments as demonstrated in Arai M. (1998) and Panciroli et al. (2012). In addition, several numerical methods have been developed in Bereznitski (2001) and Panciroli (2005). However, large parts of the available work are based

on simple high rigidity structures, such as wedges or plate panels constructed in metals. Some work was also done on complex (hull sections, complete structures) high rigidity structures e.g. in Bloxom (2012). Very little was done on simple low rigidity structures such as composite plate wedges which were studied in Panciroli (2005). Even less was performed on complex low rigidity structures. These complex structures can, for example, be the hull of a glass-fiber reinforced composite lifeboat. Some work was done on decision factors for when it is important to account for hydroelasticity, but these are mainly related to simple high rigidity structures, (Faltinsen, 1999b), (Panciroli, 2005) and (Bereznitski, 2002).

The main goal of this master thesis is to explore the importance fluid-structure interaction on lifeboats. A suitable decision factor, which can decide when it is important to account for hydroelasticity for complex low rigidity structures, will be explored. In order to keep the problem simple, a 3D model will be reduced to 2D and a verification study will be performed. The numerical results from the verification study will be compared to a full-scale test. When the model is verified, a parametric study will commence. The results from the parametric study will be used to explore a suitable parameter to determine when it is important to account for hydroelasticity. This involves a comparison of results and a quasi-static approach. In addition, is it believed that the point of flow separation will influence the result.

This master thesis consists of several chapters:

- Chapter 2 will introduce Computational Fluid Dynamics (CFD). First CFD is presented, along with some areas of application and the marine CFD problem. Secondly, the theory behind CFD is presented. Thirdly, Star-CCM+ is presented, along with relevant equation and features for this thesis.
- Chapter 3 contains an introduction to the Finite Element Method and its applications to the maritime industry. The theory behind FEM is presented along with the governing equations. In the last section, Abaqus is presented, as well as the relevant features for this
- Chapter 4 presents a brief introduction to fluid-structure interaction with a focus on the different types of problems where FSI can be applied, different couplings, and coupling algorithms. The theory regarding hydroelasticity is presented.
- In chapter 5 a rigid CFD and FEM model are developed based on Marintek (2011) and Fedem (2011). Convergence studies are performed and the final models are converted in order to perform co-simulation. The acceleration from the co-simulation is compared to the benchmark measurement in Marintek (2011).
- Chapter 6 presents a parametric study where the impact velocity, deadrise angle and material properties are varied. The maximum strains are used to explore a decision factor.
- Chapter 7 explores the effect when using different viscous regimes on the point of flow separation.
- Chapter 8 makes conclusions based upon the results from chapter 5, 6 and 7.
- Chapter 9 suggests further work.

Chapter 2

Computational Fluid Dynamics

2.1 Introduction to Computational Fluid Dynamics

CFD is a numerical solution technique used to solve the governing viscous fluid-dynamic equation; the Navier-Stokes equation. When CFD first came into use some 25 years ago, it quickly became a powerful tool for engineers and designers in the aerospace and automotive industry, (Dejhalla, 2006). The computing power of today can solve a wide range of problems using CFD. A new trend is to combine CFD with a Discrete Element Method (DEM) - providing an opportunity to handle solids in the fluid, (Haidari, 2013). These solids can be bubbles or we can study the transport of solid particles (for example useful when studying ground water pollution from heavy metals). Development to implement CFD in marine technology has been surprisingly slow. The offshore and aviation industry are relatively young industries and they quickly implemented new tools to gain an advantage as they developed. The main reason is the lack of a historical database to rely on and they had to adapt a more scientific approach, (Dejhalla, 2006).

In marine applications, the main issue is the hydrodynamic problem; the ultimate goal is to calculate the global pressure and shear force on the hull in order to predict the resistance. We are also interested in the global fluid velocity components in order to obtain the inflow pattern on the propeller and the wave pattern, in order to design a proper propeller and bulb.

The main issues that arise in marine applications are the presence of a free-surface and free-surface waves. This has given rise to numerous problems and several methods have been proposed to address these problems - among these is the Volume-Of-Fluid (VoF) method, which is based upon eulerian multiphase flow. Wave run-up and green water slamming, along with severe wave breaking and the creation of a spray root, provide huge challenges in the free-surface dynamic problem. This is due to the associated high velocity and small spatial extent of the spray root. The potential theory is unable to capture these effects and today the only reasonable method is to use numerical tools in combination with the VoF-method. Another characteristic with marine applications is that we are only concerned with incompressible, steady or unsteady, laminar or turbulent flows at high Reynolds number.

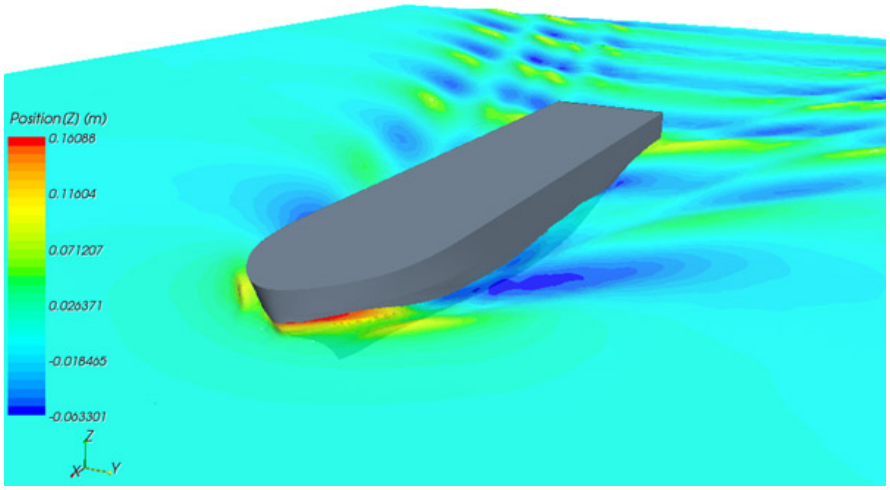

Figure 2.1: Results from CFD calculations performed on a ship, (CD-Adapco, 2014)

The development of the numerical solution techniques and fluid dynamics is a crucial aspect in the increased interest in CFD, the development of Reynolds-Averaged Navier-Stokes Equation (RANS) has been an important factor, (Gorski, 2001).

CFD is becoming an increasingly important tool in the design process for ships. This is due to the increasing demand to quickly get a ship from the drawing board to sea trials. CFD is used as a part in the design process to rapidly explore changes in geometry and see how changes affect the resistance and propulsion characteristics. Experimental fluid dynamics is still important and is still used to verify the final CFD design. We can in figure 2.1 see a CFD-calculation performed on a ship.

There are two areas of application that have received increased attention when it comes to the application of CFD to the seakeeping problem - namely large vessel motions and extreme loads in steep and breaking waves, (Dejhalla, 2006). The extreme loads are associated with slamming loads on ships and water impact. This interest is due to the fact that linear theories break down and we need to apply non-linear theory or numerical tools in order to capture the loads.

Nowadays the marine hydrodynamic community enters a new era. The possibility to apply CFD in design studies is great and there is much to be gained due to shorter computational time and more experience. The numerical models yield a more reliable and efficient solution for a wide range of problems. This does not mean that experimental fluid dynamics (EFD) is on the verge of extinction as EFD is the only way we are able to verify that our numerical model is able to capture the physics. As engineers we need to keep in mind that numerical methods and CFD can only give an approximation and that we are creating a model of the real world.

2.2 Theory Behind Computational Fluid Dynamics

Computational Fluid Dynamics (CFD) is a term used to describe the process to numerically solve the Navier-Stokes equation. This section will give a brief introduction to the CFD process. It will not focus on details, just provide an introduction.

2.2.1 Governing Equations

Fluid dynamics has three basic assumptions:

- Mass is conserved
- Energy is conserved
- Momentum is conserved

These assumptions gives arise to the governing equations for the fluid flow. Namely the continuity equation, momentum equation and the energy equation.

The fundamental equation for viscous fluid flow is the Navier-Stokes equation. This equation is derived by applying Newton's second law to fluid motion under the assumption that stress in the fluid arises due to the velocity gradient and a pressure term. The equation can therefore describe viscous flow. The solution of this equation can provide the velocity, pressure, density and the temperature in the fluid:

- $\mathbf{u} = [u(x,y,z,t), v(x,y,z,t), w(x,y,z,t)]$
- $p(x,y,z,t)$
- $\rho(x,y,z,t)$
- $T(x,y,z,t)$

In marine CFD, we are only interested in the velocity and pressure, as the density is assumed incompressible and up to this date, temperature has not been considered relevant.

The Navier-Stokes equation is a set of non-linear partial differential equations (PDEs) which can be written in several forms. This is the incompressible version of the NS-equation from Cengel (2010):

$$\rho \frac{D\vec{V}}{Dt} = -\vec{\nabla} p + \rho \vec{g} + \mu \nabla^2 \vec{V} \tag{2.1}$$

Up to this date, no general solution to the Navier-Stokes equation exists - only for simplified flows such as Stokes flow. This means to we need to turn to numerical solutions in order to achieve an approximate solution to the fluid flow.

2.2.2 Numerical Solution

According to Johannessen (2012) we need to have knowledge about several disciplines in order to achieve a good solution of the Navier-Stokes (NS) equation: Fluid Mechanics, Mathematics, Computer Science, Geometric Modeling and Meshing.

To solve the NS equation we need to discretize the solution domain and apply an equation solver. The discretization transforms the domain into discrete points which are described by algebraic equations. The equation solver will solve the equations and give an approximate solution. This process is given in figure 2.2.

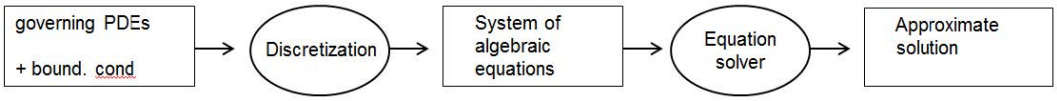

Figure 2.2: Workflow in a CFD-process, (Johannessen, 2012)

Johannessen (2012) had a good explanation regarding numerical solution. Sections 2.2.2 and 2.2.3 are adapted from his thesis.

The CFD process draws on solving the viscous flow equations namely the continuity, momentum and energy equation. They can be derived from the Navier-Stokes equation. The Navier-Stokes equation can have many forms but in the end, they describe the same flow. What set the different flows apart are the boundary conditions. In marine applications the most important boundary condition is the no-slip condition on the hull and the treatment of the free-surface and waves.

When solving a viscous flow problem, it is normal to perform a step-wise work flow. This flow is equal for all viscous and potential flows, and can be considered as a standard, (Johannessen, 2012):

1. Study the physical flow
   (a) Identify main flow phenomena
2. Construct a mathematical model
   (a) Analyze the partial differential equations
   (b) Define the physical boundary conditions
3. Formulate the numerical problem
   (a) Construct a mesh
   (b) Choose a time differencing scheme
   (c) Choose a space differencing scheme
   (d) Choose initial conditions
   (e) Choose the numerical boundary conditions
   (f) Solve numerical equations (iteration)
4. Implement the formulation in a computer code (CFD software)
5. Initiate the code and acquire an approximate solution
6. Post-process the result
7. Conclude

We apply, as previously mentioned, a space differencing scheme to discretize the domain into a computational domain. Several methods exist, but the most commonly used in CFD is the Finite

Volume Method (FVM). The space differencing scheme, in combination with the initial condition and boundary conditions, creates the discrete algebraic equation a computer can solve. The result is a set of discrete algebraic equations. This process is shown in figure 2.2. The system of algebraic equations is usually:

$$\begin{array}{ccccccccc} a_{11}u_1 & + & a_{12}u_2 & + & \cdots & a_{1n}u_n & = & b_1 \\ a_{21}u_1 & + & a_{22}u_2 & + & \cdots & a_{2n}u_n & = & b_2 \\ \vdots & & \vdots & & \vdots & \vdots & \vdots & \vdots \\ a_{n1}u_1 & + & a_{n2}u_2 & + & \cdots & a_{nn}u_n & = & b_n \end{array} \tag{2.2}$$

The equation solver will solve a system on the form $Au = b$. Where A is a coefficient matrix, u is the unknowns and b is known values (such as forces). Basically, there exist two types of solvers - direct solvers and iterative solver. The direct solver solves the system directly by inverting A. This is very slow and very computational costly for normal sized systems. The best approach is to use an iterative solver which iterates to an approximate solution.

2.2.3 Convergence of the Solution

For a numerical method or software to prove successful it has to successfully calculate the correct solution for known examples. Normally this relies on several aspects but the most important are:

- Consistency
- Stability
- Convergence
- Conservation
- Accuracy

Consistency

A numerical method is described as consistent if the approximate solution converge to the exact solution (provided by the PDEs) if the discretization tends to zero. This means $\Delta t \to 0$ and $\Delta x, \Delta y, \Delta z \to 0$. There will always be a difference between the numerical solution and the exact solution, but if the discretization tends to zero the difference will get smaller.

Stability

A numerical solution algorithm is stable if the solver does not amplify an error that might arise due to the discretization. If the method is unstable, this error cause the disturbance to grow infinitely making the solution diverge.

A common parameter used to characterize whether a transient solution method is stable or not is the Courant-Fredrichs-Levi (CFL) number. This number can be written in 1D:

$$\mathrm{CFL} = u\frac{\Delta t}{\Delta x} \tag{2.3}$$

u is the velocity, Δx is the smallest cell length in flow direction and Δt is the time step. This number expresses how much convection the cells experience per time step. This means that if $\mathrm{CFL} \leq 1$, the fluid moves less than one cell per time step. If we use an explicit time scheme, the stability condition requires that the CFL-number is less than one, due to the fact that we are only relying on previous results and differentiation. If we are applying a second-order time integration scheme, the CFL-number must be below 0.5. An implicit scheme is not that sensitive to the CFL-number and can handle higher CFL-numbers, this is due to the fact that we are making some assumptions (e.g. linear or constant acceleration) and that we know the force in the next time step. The time step is now only dependent on the required accuracy.

This means that an explicit scheme requires a very small time step, while implicit can handle larger time steps. The applications are therefore different - explicit schemes are usually used in analysis regarding impact due to the rapid changes, while implicit schemes are used for simulations with longer time aspects e.g. 3 hours simulations.

Convergence

The solution is converging if the solution of the algebraic equations tends towards the exact solution of the PDEs as the grid size goes towards zero. One should note that the solution only converges if the algorithm is both stable and consistent. Convergence is usually checked by performing a number of simulations using different mesh sizes and time steps.

Convergence is achieved through iterations and the rate of change towards the exact solution is of interest. This is also known as the convergence rate.

Conservation

The discrete algebraic equation needs to fulfil the conservation equations that are imposed in the PDEs. If these equations are satisfied within the whole domain, one can expect that an error will be due to improper distribution of the result over the domain.

Accuracy

A numerical scheme is only an approximation of the exact solution. The accuracy depends on the errors implemented in the solution algorithm and code, and when imposing boundary conditions. We also have four other types of errors:

- Modeling error

- Discretization error
- Iteration error
- Round-off error

The modeling error arises if there is a difference between the real world geometry and the computational geometry or when simplifications are introduced. Assumptions can also introduce modeling errors.

The discretization method will transform the domain into a computational domain and these elements or control volumes have their limitations. This will give rise to discretization errors.

The solution algorithm (the process which solves the discrete equations) can introduce errors and this is known as iteration error or convergence errors.

Round-off errors might arise due to the limitations of the hardware and software. The hardware errors are a result of the capability of the machine to store and transfer values. While badly written software might introduce round-off errors when treating values with different magnitude.

2.3 Star-CCM+

Star-CCM+ is a CFD-software developed by CD-Adapco. The purpose of the software is to introduce an advanced CFD-software a common engineer can use. Star-CCM+ also has the capability to solve problems with solid stress and heat transfer. Star-CCM+ contains a complete package with everything included, such that the whole process from the creation of the geometry to the post-processing can be done within the software.

Star-CCM+ utilizes the Finite Volume Method to discretize the computational domain and the governing equations. This means that Star-CCM+ applies the divergence theorem so that volume integrals in the PDEs are converted to surface integrals. This, in combination with the initial conditions and boundary conditions creates the discrete algebraic equation a computer can solve.

This section will give a brief introduction to the governing equations in Star-CCM+ and the different steps in the procedure. The thesis written by Johannessen (2012) contains a good explanation regarding Star-CCM+ and section 2.3 is adapted from his work. Some sections have been included regarding the HRIC-scheme (High Resolution Interphase Capturing) and the co-simulation module with Abaqus.

2.3.1 Governing Equations

Star-CCM+ is, as previously mentioned, based upon the finite volume method. The starting point is the Navier-Stokes equation on conservative integral form. The domain is then subdivided into a finite number of control volumes. These volumes can be of arbitrary shape. The volumes are then subjected to the PDEs and transformed using the divergence theorem and FVM

to a discrete system. It is normally assumed that the flow is governed by the three-dimensional Reynolds-Averaged Navier-Stokes equation. The governing equations are:

Mass conservation:

$$\frac{d}{dt}\int_V \rho dV + \int_S \rho(\mathbf{v}-\mathbf{v}_b)\mathbf{n}dS = 0 \tag{2.4}$$

Momentum conservation:

$$\frac{d}{dt}\int_V \rho\mathbf{v}dV + \int_S \rho\mathbf{v}(\mathbf{v}-\mathbf{v}_b)\mathbf{n}dS = \int_S (T-pI)\mathbf{n}dS + \int_V \rho\mathbf{b}dV \tag{2.5}$$

Generic transport equation for scalar quantities:

$$\frac{d}{dt}\int_V \rho\phi dV + \int_S \rho\phi(\mathbf{v}-\mathbf{v}_b)\mathbf{n}dS = \int_S \Gamma\nabla\phi\mathbf{n}dS + \int_V \rho\mathbf{b}_\phi dV \tag{2.6}$$

Space conservation law:

$$\frac{d}{dt}\int_V dV - \int_S \mathbf{v}_b\mathbf{n}dS = 0 \tag{2.7}$$

In the equations ρ is the density, v the fluid velocity, v_b the velocity of the control volume, $\mathbf{n}$ the unit normal vector of the control surface, T the stress tensor, p the pressure, I the unit tensor, ϕ a scalar, Γ the diffusivity coefficient, $\mathbf{b}$ the body force and, b_ϕ sources and sinks of ϕ.

Since slamming is associated with multiphase flow between air and water, the phase fraction must be calculated with an additional equation:

$$\frac{d}{dt}\int_V \alpha dV + \int_S \alpha(\mathbf{v}-\mathbf{v}_b)\mathbf{n}dS = 0 \tag{2.8}$$

Where α is a volume fraction between air and water. The two liquids (water and air) are considered two immiscible parts of one fluid, where the fluid properties are assumed to vary according to the volume fraction of the mixture. The properties that change are the density ρ and viscosity μ:

$$\rho = \rho_1\alpha + \rho_2(1-\alpha) \tag{2.9}$$

$$\mu = \mu_1\alpha + \mu_2(1-\alpha) \tag{2.10}$$

The segregated iterative solver (solves velocity and pressure separated because we cannot solve pressure and velocity coupled using the VoF-method) in Star-CCM+ solves the Navier-Stokes equations. A linearized momentum component is first solved using an existing pressure and mass transport through the cell faces. Then an algorithm (SIMPLE) is used to correct the pressure - a schematic view can be viewed in figure 2.3.

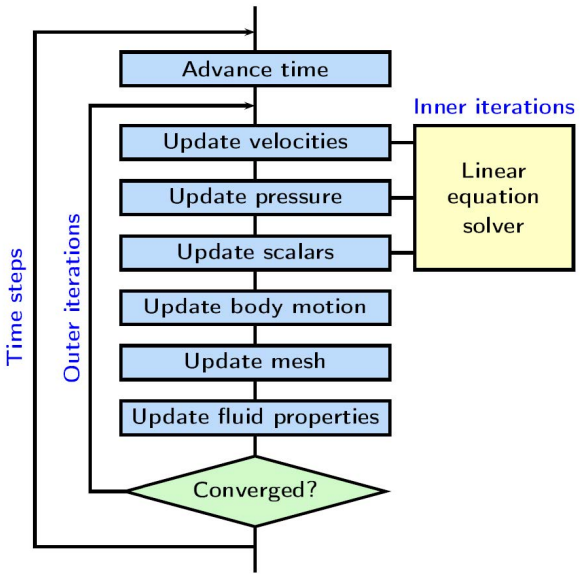

Figure 2.3: Flow chart for the solution algorithm, from Johannessen (2012)

2.3.2 Modeling in Star-CCM+

The first step in a CFD-simulation is to define the geometry and domain. The geometry can be imported from other external CAD-software (Computer Assisted Drawing) or created locally in Star-CCM+. Star-CCM+ has a build-in 3D-CAD environment. This is very useful when modeling the geometry and yields great advantages with respect to adaptability - we can quickly change and modify the geometry if we are doing a design study. The 3D-CAD engine in Star-CCM+ can create models from scratch and also modify existing CAD-models. A good feature is that we do not have to enter the CAD-module in order to change a parameter - this can be done in the simulation window. This is a feature that enables you to quickly change parameters and re-run the analysis - overall decreasing the solution time.

2.3.3 Boundary Conditions

In order to achieve a physical correct solution it is paramount to apply the correct boundary conditions on the correct surfaces. Star-CCM+ has a vast variety of boundary conditions but the most important in this thesis are the velocity inlet, pressure outlet, wall, symmetry plane or co-simulation. The velocity inlet creates an inlet with a fluid flow in a specified direction, with a specified speed. The pressure outlet is an outlet where the outlet pressure is specified. The wall condition implied that the normal and tangential velocity on the boundary is zero. This physically means that no fluid is allowed to flow through the boundary and implies a no-slip condition. The symmetry plane condition is used to simplify the problem by implying symmetry, thus drastically reducing the number of cells. The condition states that no flow is allowed through the plane, but the fluid can flow parallel to the plane without introducing shear force. This is equivalent to mirroring the surface around the plane. The co-simulation boundary condition states that the displacement of this boundary is determined by the co-simulation engine.

2.3.4 Mesh

A good mesh is critical to obtain good results. Meshing is the process of dividing the domain into cells where the PDEs will be applied. There are two cycles of meshing that must be performed. The first is the surface mesh. This is crucial in order to create a volume mesh. The surface mesher creates a mesh on the defined faces (surfaces) in the domain; the surface mesh facilitates growth of the cells used in the volume mesh. There are several surface mesh modules in Star-CCM+, but the most important one is the *Surface Remesher*.

The volume mesh is the work horse of the FVM. Star-CCM+ has basically three different types of volume meshers.

The tetrahedral mesh is a fast method to generate the mesh. It requires the least amount of memory, but it is the least accurate and needs over six times more cells to obtain a solution with the same degree of accuracy as polyhedral. However, it is useful on complex geometries, but it is dependent on a high quality surface mesh.

The polyhedral mesher is more balanced than the tetrahedral mesher. This mesher uses more memory but it is much more accurate and we can therefore use fewer cells. It is also useful on complex geometries, but it is dependent on a high quality surface mesh.

The trimmer mesher uses hexahedral cells to generate the mesh. It has the same properties when it comes to accuracy as the polyhedral mesher, but it does not require a high quality surface mesh in order to create a volume mesh. This mesher is also more convenient as it is capable to capture the free-surface more easily. Due to the box-shape of the elements, the free-surface will be more defined.

2.3.5 Physics

Star-CCM+ have several options when it comes to modeling the physics. Here are the most relevant for the work.

- Space, time and motion
- Flow and energy
- Multiphase flow
  - Volume of Fluids
- Dynamic Fluid Body Interaction
- Co-Simulation with Abaqus

When choosing the modules, some are selected using the auto-select feature. This lets the program select appropriate modules, which is advised by CD-Adapco (2014).

Space, Time and Motion

We need to activate the space-module in three-dimensions due to the fact that VoF-waves only exist in three dimensions. In the time module we have three choices, but the only model we can apply is the implicit unsteady, since we cannot define multiphase flow using an explicit unsteady solver, (CD-Adapco, 2014). In a co-simulation analysis, the most important module in the motion section is the morpher. This will be applied under the FSI-analysis and is basically a way to deform the mesh due to the fluid-structure interaction deformations.

Flow and Energy

In this section, we choose which flow regime governs our simulation. Important choices are segregated or coupled flow (if the solver solves the pressure and velocity coupled or not). We can only use the segregated solver, as the VoF-solver cannot solve the pressure and velocity in a coupled manner. We need to select the type of viscous regime (inviscid, laminar or turbulent). The equation of state defines if the flow is incompressible or not. We also must include gravity.

Multiphase Flow

For marine applications is one of the most important choice the eulerian multiphase flow module and, the Volume-of-Fluids model based on the former. This is applicable for a system which contains two or more immiscible fluid phases (such as air and water). This enables us to study the interface and motion of these two layers. In this way, can we study the free-surface and waves. Waves (including a flat surface) are especially defined in the VoF-Waves section. The spatial distribution between the two phases is defined as a volume fraction. To calculate, this distribution Star-CCM+ solves the transport equation for the phase volume fraction. In order to achieve a sharp interface between the two phases, a 2nd-order discretization scheme is used. Star-CCM+ also utilizes a HRIC (High Resolution Interphase Capturing) Convention Discretization Scheme. This scheme utilized a correction in order to provide a sharp interphase between air and water. This HRIC-scheme only becomes active when the CFL-number is below 0.5. If the CFL-number is between 0.5 and 1, a combination between HRIC and upwind discretization is used and, if the CFL-number is above 1 only upwind discretization is used to obtain the interphase between the phases.

Dynamic Fluid Body Interaction

This module allows you to model the motion of a rigid body and the response due to pressure, wall shear forces, and other forces that are defined within the module. Star-CCM+ calculates the total force acting on the body and then calculates the trajectory based upon this force. This module is applied to get a free-falling object in Star-CCM+.

Figure 2.4: Activate physics modules in FSI-analysis

Co-Simulation

The co-simulation module is a module that enables communication between Abaqus and Star-CCM+ using the co-simulation engine provided by Simula. In figure 2.4, the activated physics modules during a FSI analysis are shown. It is important to emphasize that the model in Star-CCM+ and Abaqus needs to be topologically equal. This signifies that they need to be equal and in the same location in space. In a co-simulation analysis it is also important to define a coupling surface in Star-CCM+ this also needs to be equal to the surface defined in Abaqus. If this is not the case, the mapping and exchange of information will not work. The Cell Quality Remediation module allows use of low quality cell, which may occur during deformation of the mesh.

2.3.6 Convergence

In order to determine if our solution is converging we have to monitor the residuals. The residual demonstrates the difference in equilibrium in the discretization method, or the difference between the internal forces and external forces. If we have an exact solution the residual will be equal to zero. The residuals should drop in the order of 10^2 in a time step in order to achieve a converging solution. It has been demonstrated that a drop of 10^1 is sufficient, (Johannessen, 2012).

Chapter 3

The Finite Element Method

3.1 Introduction to the Finite Element Method

The Finite Element Method (FEM) is a widely used tool for performing calculations on structures. The main concern in these calculations is strength considerations that are used in design studies and verification of marine structures such as ships, platforms, risers, and other structures. FEM is also associated with non-linear analysis, such as ultimate limit state (ULS), which deals with collapse of marine structures. We are also concerned with the accidental limit state (ALS), e.g. the capability to survive an accident with a certain probability level. Today, FEM is a widely used tool due to the robustness, proven capabilities, and accuracy. FEM was developed at University of California - Berkeley mainly due to demands from the aerospace industry and NASA. Due to developments in computer science and the capacity of modern computers, FEM is now available for the everyday non-specialist. There exists a wide range of available and proven commercial software, such as Abaqus, LS-DYNA, and ANSYS. Even though the capabilities of FEM have been proven, care should be taken. FEM provides a numerical approximation and it has its limits. Experience and knowledge are paramount to verify the final result. An example of wrong use is the Sleipner accident. The engineers used Finite Element Analysis (FEA) software called NASTRAN to perform the strength calculations on the Condeep platform, Sleipner. When the platform was moved out of the dry dock and ballasted, it experienced a catastrophic failure and sunk to the bottom of a fjord in Norway. The incident occurred due to the strength calculations perform in NASTRAN. Afterwards it has been shown that the software extrapolated the shear deformations to a brace. The consequence was that the program underestimated the shear deformation in the brace with 50 %, leading to the failure of the structure.

Today, many of these errors have been eliminated, but care is still advised. FEA is a great tool that provides excellent results for strength calculations, but care should be taken, as results are approximations.

3.2 Theory Behind the Finite Element Method

The finite element method is a numerical solution technique used to solve and find an approximation to the boundary value problem of a partial differential equation. The method subdivides the structure into a finite number of elements and aims to minimize an error function called residual. This section focuses on finite elements applied to structural problems. It should be noted that this method is applicable to many other problems. For example solving, heat convection problems or solving the Navier-Stokes equation.

3.2.1 Governing Equations

This subsection is based on the books of Fish and Belytschko (2007) and Langen and Sigbjornsson (1986).

Basic formulation

The finite element method for structural problems is based upon several assumptions:

- Deformations are small
- Linear elastic behaviour
- No gap or overlap occurs during deformation of the solid

Other assumptions are described below.

Kinematic compatibility This states that we can express the strains, ε, in the structure based on the displacements u. Note that the expression varies with what type of elements and formulation (e.g. non-linear geometry) we are using. We may obtain this relationship for a bar-element (1D):

$$\varepsilon_{xx} = \frac{\partial u_x}{\partial x} \tag{3.1}$$

Where u_x is the displacement in x-direction and ε_{xx} is the strain in x-direction.

Or on matrix form (2D):

$$\varepsilon = \begin{bmatrix} \varepsilon_{xx} \\ \varepsilon_{yy} \\ \gamma_{xy} \end{bmatrix} = \nabla_s \mathbf{u} = \nabla_s \begin{bmatrix} u_x \\ u_y \end{bmatrix} \tag{3.2}$$

Where $\mathbf{u}$ is the displacement vector, γ_{xy} is the shear strain and the operator ∇_s can we written as:

$$\nabla_s = \begin{bmatrix} \frac{\partial}{\partial x} & 0 \\ 0 & \frac{\partial}{\partial y} \\ \frac{\partial}{\partial y} & \frac{\partial}{\partial x} \end{bmatrix} \tag{3.3}$$

Equilibrium This implies that the structure is in equilibrium in all parts of the structure. Based upon equilibrium of a finite element with respect to the internal forces (stresses) and the external forces we may write:

$$\nabla_s^T \sigma + \mathbf{b} = 0 \tag{3.4}$$

Where ∇_s^T is the transposed matrix defined earlier. $\mathbf{b}$ and σ are vectors containing the body forces and stresses.

Stress-Strain relationship This states that we can express the stress using Hooke's law of elasticity.

$$\sigma = E\varepsilon \tag{3.5}$$

Or

$$\sigma = D\varepsilon \tag{3.6}$$

Where E is the modulus of elasticity and D is a material matrix based on E and the Poisson ratio ν. In equation 3.5, the strain ε is a scalar for 1D-problems, while in equation 3.6 the strain ε a is vector with the strain components in different directions for 2D or 3D-problems.

We have now developed the weak form of the structural problem based upon kinematic compatibility, equilibrium and a stress-strain relationship, where equation 3.4 is the governing equation.

Energy Methods

The finite element method for structural analysis is based on the principle of virtual displacements. This principle states that:

> The total virtual work performed by a system in equilibrium when it is subjected to virtual compatible displacements is equal to zero, (Langen and Sigbjornsson, 1986).

We can according to Langen and Sigbjornsson (1986) write the equation of motion for a static system as:

$$Kr = Q \tag{3.7}$$

Where K is the stiffness matrix, r is the nodal displacement and Q is an external load vector. When a static system is subject to a virtual displacement field that satisfies the geometrical boundary conditions we may write:

$$\int_V \delta u^T \mathbf{X} dV + \int_S \delta u^T \mathbf{T} dS + \delta r^T \mathbf{Q} = \int_V \delta \varepsilon^T \sigma dV \tag{3.8}$$

Where the left side of equation 3.8 represents the external virtual work and the right the internal virtual work. $\mathbf{X}$ is the volume forces, $\mathbf{T}$ is the surface tractions, $\mathbf{Q}$ is the load vector, u^T is the displacement vector, ε is the strain vector and σ is the stress vector. $\delta\varepsilon$ is the virtual strain, δr is the virtual nodal displacement which complies with the virtual displacement δu.

For a system subject to dynamic loads an additional term arises due to d'Alembert principle:

$$dF^I = \rho \ddot{u} dV \tag{3.9}$$

The virtual work can now be written as:

$$\int_V \delta u^T \mathbf{X} dV + \int_S \delta u^T \mathbf{T} dS + \delta r^T \mathbf{Q} - \int_V \delta u^T \rho \ddot{u} dV = \int_V \delta \varepsilon^T \sigma dV \tag{3.10}$$

3.2.2 Numerical Solution

The Finite Element Analysis (FEA) can roughly be subdivided into four steps.

1. Discretization
2. Element analysis
3. System analysis
4. Solve the dynamic system

Discretization

The discretization deals with the process to subdivide the structure or system into a finite number of elements. These elements are interconnected through nodes which are located at the element boundaries.

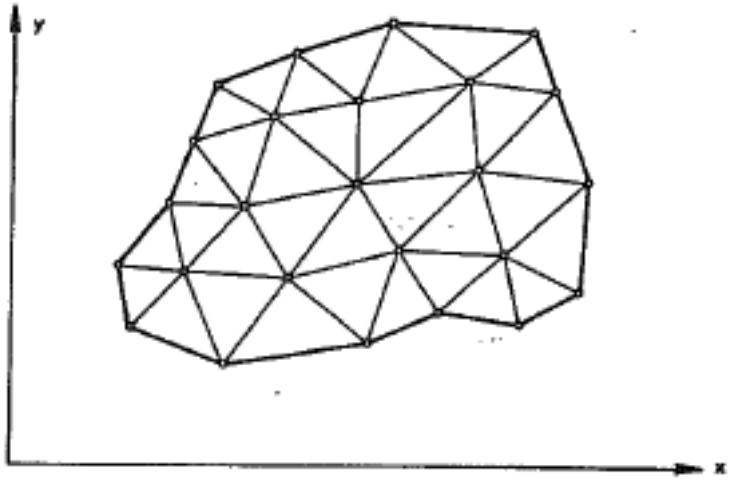

Figure 3.1: Subdivision of an arbitrary structure into finite elements, (Langen and Sigbjornsson, 1986)

A such subdivision can be viewed in figure 3.1. This meshing procedure is crucial to achieve an accurate solution. In order to create the mesh, we need to decide what type of elements to use and the required degree of accuracy. We also need to know something about the behaviour of the structure in order to create a high quality mesh for accurate eigenvalue analysis and dynamic

analysis. The process to create a high quality mesh demands knowledge from the user and can take quite some time. Therefore experience and knowledge are crucial in order to reduce the time.

The number of unknowns is decided from the mesh. In structural analysis they are represented by nodal displacements and rotations, and give arise to the number of degrees-of-freedom (DOFs) of the system.

Element Analysis

The displacement within an element can be described through the nodal displacement and a set of interpolation functions.

$$u(x,y) = Nv \tag{3.11}$$

Where u is the displacement, v is a vector containing the nodal displacements and N is a matrix with the interpolation function. These interpolation functions make it possible to describe the displacement within the element expressed by the nodal displacement. These are basically shape functions that are constructed in such a way that $N_i(x,y) = 1$ when it is evaluated at node i and zero at all other nodes. We can write

$$u = \begin{bmatrix} u(x,y,z) \\ v(x,y,z) \\ w(x,y,z) \end{bmatrix} = Nv = [N_1 N_2 ... N_n]v \tag{3.12}$$

Where

$$N = \begin{bmatrix} N_i^1(x,y,z) & 0 & 0 \\ 0 & N_i^2(x,y,z) & 0 \\ 0 & 0 & N_i^3(x,y,z) \end{bmatrix} \tag{3.13}$$

The interpolation functions can have different order and properties.

From equation 3.2 we can see the relationship between the strain and displacement. We know that the strain is a function of the displacement. We have established that it is possible to describe the displacements within an element by a set of interpolation functions and the nodal displacements. We may write the following relationship:

$$\varepsilon = f(u) = f(Nv) = f(N)v = Bv \tag{3.14}$$

This equation expresses the relationship between the strain and the nodal displacements.

From the stress-strain relationship described in equation 3.6, we can obtain the stresses in the element.

$$\sigma = D\varepsilon = DBv \tag{3.15}$$

The size and composition of the vectors and matrices ε, B, σ and D varies according to which theory or model we apply. There exist great differences between plate, shell, beam or bar elements. This implies that we use different types of interpolation functions and DOFs for

different types of problems. For example, a shell utilizes the nodal rotations and accounts for shear deformation, while a bar does not account for these factors. In order to decide which element we should use, a basic understanding of the structure and the expected response is crucial. For a deeper understanding please refer to Langen and Sigbjornsson (1986).

We can now establish a dynamic equilibrium equation of each element based on equation 3.10:

$$\int_V \delta u^T \mathbf{X} dV + \int_S \delta u^T \mathbf{T} dS + \delta r^T \mathbf{Q} + \delta v^T \mathbf{S} - \int_V \delta u^T \rho \ddot{u} dV = \int_V \delta \varepsilon^T \sigma dV \tag{3.16}$$

Where **S** is a vector with nodal forces which corresponds to the nodal displacements.

If we assume virtual kinematic compatibility:

$$\delta u = N \delta v \tag{3.17}$$

We can combine equation 3.12, 3.14, 3.15 and 3.17 into equation 3.16 and get:

$$\delta v^T (S + \int_V N^T X dV + \int_S N^T T dS - \int_V \rho N^T N dV \ddot{v} - \int_V B^T D B dV v) = 0 \tag{3.18}$$

This implies that we only have a non-trivial solution when $\delta v \neq 0$, hence the expression within the parentheses has to be zero in order to fulfil the equilibrium. We can write:

$$S = kv + m\ddot{v} + P \tag{3.19}$$

Where

$$k = \int_V B^T D B dV \tag{3.20}$$

is the element stiffness matrix and

$$m = \int_V \rho N^T N dV \tag{3.21}$$

is the consistent mass matrix (meaning that the mass is distributed over the element with the same interpolation functions as k is derived from) and the load vector

$$P = -\int_V N^T X dV - \int_S N^T T dS \tag{3.22}$$

which represent the distributed load on the element.

As previously mentioned, the order and shape of the interpolation functions vary according to which elements we are applying. It should be noted that B is usually the derivative of the interpolation function. The full relationship for different element types can be found in Langen and Sigbjornsson (1986).

System Analysis

When we have computed the stiffness, mass and load matrices for every element in the structure we can assemble the elements together in order to perform calculations on the structure in total. The boundary conditions are also implemented in this step. This is done by demanding compatibility between the DOFs at each element node. The nodal displacement for a node that is shared between several elements should be equal. Equilibrium at each node is then assured.

This compatibility, or topological connectivity, can be expressed:

$$v_i = a_i r \tag{3.23}$$

v_i is the DOF in the individual element while r is the DOF in the whole system. a_i is a connectivity matrix. The equilibrium at each node then becomes:

$$Q = \Sigma_i a_i^T S_i \tag{3.24}$$

By introducing equations 3.19 and 3.23 we get:

$$M\ddot{r} + Kr = Q \tag{3.25}$$

Where K, M and Q are the stiffness, mass matrix and load vector of the system, respectively.

The stress can be calculated from the given relationship $v_i = a_i r$ such that:

$$\sigma(x,y,z) = DB(x,y,z)v \tag{3.26}$$

Eigenfrequency Analysis

We can write the equation of motion for an undamped free-oscillating system as:

$$M\ddot{r} + Kr = 0 \tag{3.27}$$

If we now assume that r is harmonic we can write:

$$r = \phi \sin(\omega t) \tag{3.28}$$

$$\ddot{r} = -\omega^2 \phi \sin(\omega t) \tag{3.29}$$

We may then write:

$$(K - \omega^2 M)\phi = 0 \tag{3.30}$$

This is the general eigenvalue problem. This equation only has a non-trivial solution when $\det(K - \omega^2 M) = 0$. Where ω is the undamped eigenfrequency of the system and ϕ is the corresponding eigenvector.

This equation is solved numerically with different methods.

Damping Models

The most commonly used damping model in structural dynamics is the Rayleigh damping model, (Langen and Sigbjornsson, 1986). The damping coefficient C is a linear combination of the mass and the stiffness matrix.

$$C = \alpha M + \beta K \tag{3.31}$$

α and β are the damping coefficients. It can be shown that the damping supplied by α gives a damping ratio which is inversely proportional to the response frequency, while β is linearly proportional to the response frequency. In this way can α and β be used to damp out different eigenfrequencies.

3.2.3 Accuracy of the solution

Element requirements

Convergence of FEM implies that the discretization gets finer and finer, such that we approach the exact solution. Convergence is achieved if the element can satisfy the following requirements:

1. Compatibility
   (a) The displacement field must be continuous within the element
   (b) The strain on the boundary between two elements should be finite.
2. Completeness
   (a) The displacement model (interpolation functions) must be able to describe rigid body motion
   (b) The displacement model must be able to describe constant strain within the element
3. Invariance
   (a) The response of an element must be independent in relation to the position in the global coordinate system

Errors

We have three types of error associated with FEM.

Modeling error. Errors which arise due to the choice of mathematical equations and assumptions. These assumptions are associated with the type of element - thin plate, thick plate, beam, shell, solid, elastic model or use of non-linearities or damping model.

Discretization error. When we subdivide the structure into elements we need to have a fine enough mesh in order to achieve an accurate solution. This error approaches zero as the mesh gets finer.

Computer error. These types of errors arise due to the storage capacity of computers and its capability to store only a finite number of digits. These types of error grow in significance when the mesh gets smaller.

3.3 Abaqus

Abaqus is a commercial software which utilizes the finite element method in structural analysis. It has a wide range of possibilities from static analysis to dynamic implicit, dynamic explicit, buckling or eigenfrequency analysis. Abaqus also has the possibility to consider non-linear geometry, materials and solution algorithms. The program is widely applied in the industry and it is considered to be a leading software along with LS-DYNA, ANSYS and SESAM. This is due to the vast possibilities when it comes to modeling. We have the possibility to model cracks, pre-deformed structures, non-linear geometry, non-linear material, non-linear boundary conditions and fatigue damage.

Important aspects for a FEM program are the element library, capabilities, and solution algorithms. This section will describe a general walkthrough of the program emphasizing aspects that are important for an FSI-analysis.

3.3.1 Analysis Work Flow Procedure

The analysis work flow procedure in Abaqus is streamlined as in Star-CCM+. Figure 3.2 shows the modeling window in Abaqus. The section will briefly go through the different parts and make comments who to perform a FSI-analysis in Abaqus.

1. **Parts**. The first thing you do is to use Abaqus' own CAD-environment to model the structure; here you choose what type of part you are modeling (solid, shell, plate, beam). This is important because, for example, a plate or shell does not represent a physical thickness, while a solid structure does. It is also possible to import an existing CAD-model or FEM-model.

2. **Materials**. We define the material that is used in the analysis. The most important aspects here are the density, mechanical properties, and material damping.

3. **Section**. We connect a material to a part - making it a section.

4. **Assembly**. Real structures consist of several sections; in this section do we tie all the sections together. One important aspect here is that we need to define a *Surface* that corresponds to the coupled surface in Star-CCM+. This surface has to be topological equal in order to achieve a data exchange. Only one coupled surface can be specified and this surface has to contain all the surfaces that are going to be coupled with Star-CCM+. The assembled section must be in the same location in space as in Star-CCM+.

5. **Step**. Here we define what type of analysis that you are going to perform. The options

applied in this thesis are *Static - General*, *Dynamic - Implicit*, and *Frequency*. The non-linear geometry model is applied here.

6. **Loads**. We can define the loads which are going to be applied in the model. As the pressure and the shear forces are transferred from Star-CCM+ the only load applied is gravity.
7. **BCs**. Here we apply boundary conditions, which are essential in order to be able to solve the system. These conditions need to correspond to the conditions applied in Star-CCM+. In this thesis, symmetry conditions have been used. This is done in order to model the hull subject to free-fall.
8. **Predefined Fields**. In order to release the hull at an initial velocity condition we need to apply an initial velocity as a predefined field.
9. **Mesh**. In this section we decide the mesh density and what kinds of elements to use. This module is located within each part.
10. **Job**. Here you create and run the job to begin the analysis. The results can be viewed in the post-processor.

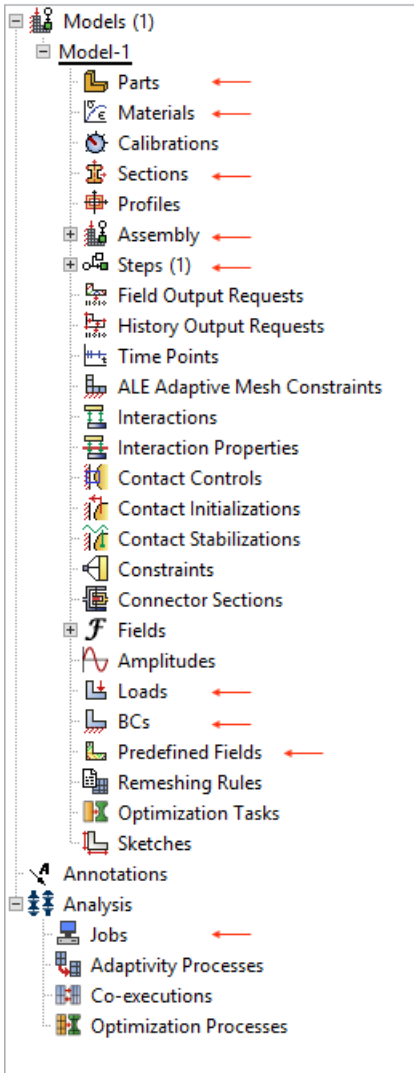

Figure 3.2: Picture of the workbench in Abaqus - the arrows represents the most important sections

Chapter 4

Fluid-Structure Interaction

4.1 Introduction to Fluid-Structure Interaction

The following section is an adaptation from CD-Adapco (2014), Zienkiewicz et al. (2013) and Piro and Maki (2013). Fluid-Structure Interaction (FSI) means that there is a mutual interaction between a fluid-solid boundary or a gas-solid boundary. This means that there exists a coupling between the two domains and that they must be solved in a coupled manner in order to obtain satisfactory results. This coupling signifies that they influence each other - the fluid influences the structure through pressure forces and the structure influences the fluid through structural deformations. We can distinguish between a static FSI coupling and a dynamic FSI coupling. The static coupling involves typical interaction between the aerodynamic and elastic forces of a wing; however, this coupling can be dynamic as well, e.g. flutter. This will not be the focus of this master thesis. The dynamic fluid-solid interaction is usually associated with fluid-solid interaction with a rigid or elastic body. A rigid body can typically be an offshore platform, ship, or parts in a pump. These problems are usually characterized by the fact that the deformation on the body from the fluid flow does not influence the fluid flow. The other kind of problem involves an elastic body. This means that the fluid flow deforms the body and the structural deformation influences the fluid flow. This implies that there exists a coupling between the fluid solution and the solid solution, as the fluid will cause a deformation on the body and this deformation will cause a change in the fluid flow which again will cause a different deformation of the body. This is denoted as a strong coupling between the two domains. We can also have a weak coupling. This master thesis will focus on strong fluid-solid interaction coupling, but the method is also capable of handling heat transfer.

The consequences of fluid-structure interaction can be severe. An example is the collapse of the Tacoma Narrows Bridge in 1940. Turbulent wind interfered with the eigenfrequency of the bridge, leading to the collapse of the bridge.

There exist a vast number of applications of FSI for marine technology, for example, Vortex Induced Vibrations (VIV), where a cylinders starts to vibrate due to shedding of vortices. Another example is impact of wedges or lifeboats where the hull deforms during impact. Another hot topic is FSI applied to the analysis of high-speed crafts or ships which experience springing,

whipping, or hydroelasticity, (Faltinsen, 2005).

Other applications of fluid-structure interaction analysis can be analysis of artificial heart valves, parachuting or wind turbines.

We can apply fluid-structure interaction to a wide range of problems. This master thesis will focus on FSI applied to marine technology or more specifically the phenomenon of hydroelasticity.

4.2 Theory behind Fluid-Structure Interaction

In this thesis the fluid domain is solved with CFD calculations, while the solid domain is solved with FEA calculations. These two solution domains create the foundation for the numerical fluid-structure interaction analysis. This section will focus on the type of problems we can solve, what distinguishes them, and solution algorithms and coupling schemes.

4.2.1 One-Way Interaction

One-way interaction problems indicate that there is a small interaction between the fluid and solid. This means that the fluid can impose some response to the structure, but the response is not significant enough to change the fluid flow. A classic example is an analysis of a piston in an internal combustion engine. The piston has a huge impact on the flow in the engine, but the fluid does not deform the piston. A one-way interaction implies that we only send information from one code to another, (CD-Adapco, 2014).

Figure 4.1 shows the typical coupling scheme for a one-way interaction problem. This coupling scheme will lead to problems gaining a solution when dealing with highly coupled problems e.g. hydroelasticity.

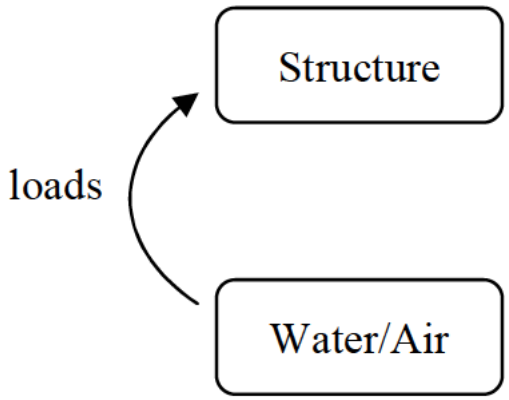

Figure 4.1: Schematic drawing of a one-way coupling scheme, (Bereznitski, 2002)

4.2.2 Two-way Interaction

Two-way interaction indicates that the fluid pressure and shear forces introduce a deformation in the solid (or rigid body motion) and this deformation leads to a change in the fluid flow. This means that we need to iterate in order to achieve a satisfactory solution. A classic example is a free-fall drop of a wedge into water. As the wedge progresses through the water, the pressure and viscous forces will slow the wedge down and the wedge may start to vibrate. Two-way interaction implies that we send information between two codes - see figure 4.3. We must distinguish between a *weak* coupling and *strong* coupling.

The *weak* coupling relates to a steady-state solution and can almost be viewed as a one-way interaction problem. One example is a pipe with a bend containing a fluid flow; the bend significantly alters the flow pattern and the change in flow pattern influences the curvature of the bend (given a reasonable flexible body). We are interested in the steady-state solution. The deformation velocity of the bend will drop to zero when steady-state is achieved. In a typical algorithm formulation, the CFD-solver will calculate the pressure and export the result to a file, while the FEM-solver imports the pressure and calculates the deformations based on the pressure. The deformations are then exported and used to deform the structure in the CFD-solver. This procedure is continued until a steady-state condition is achieved. This implies that the time scale of the problem is not relevant. The coupling scheme used is typically explicit, as the deformation solution depends on pressure solution in the previous step. This is also called a staggered coupling. For an explicit coupling, the exchange of information performed once per coupling time step, (CD-Adapco, 2014).

The *strong* coupling relates to dynamic problems, where the hydrodynamic and dynamical loads can change dramatically over time. This implies that the time scale of the problem is relevant. In this type of coupling algorithm, the data is stored in the computer's memory. The exchange will therefore occur at regular intervals, called coupling step or coupling time step. At the coupling step, information is transferred between the CFD-solver and the FEM-solver. Depending on the coupling strength (how tightly coupled the problem is) of the problem, it may be necessary to perform the exchange several times during the time step in order to achieve convergence and stability, (CD-Adapco, 2014). This type of coupling is denoted an implicit coupling or referred to in the literature as "iterative staggered", "iterative successive substitution" or "multiple iterative coupling", (Zienkiewicz et al., 2013). This coupling is necessary when dealing with the interaction of a light structure in a heavy and incompressible fluid. A good example of this is when an aluminum plate interacts with air versus water. The air is a light fluid and the coupling is not that imminent, and the problem can almost be considered steady-state. While water is a heavy fluid that is incompressible. An implicit coupling scheme is necessary for this problem since the deformations and fluid flow can change dramatically over time; to assure the strong coupling we need to perform several exchanges within each time step. A ship is another example. A ship only floats because it is lighter than the water it displaces. Hence this is a strongly coupled problem. In order to achieve an implicit coupling a co-simulation engine is needed, (CD-Adapco, 2014). We can in figure 4.2 see a schematic drawing of an implicit coupling.

Figure 4.3 shows the typical coupling scheme for a two-way interaction problem. This could be

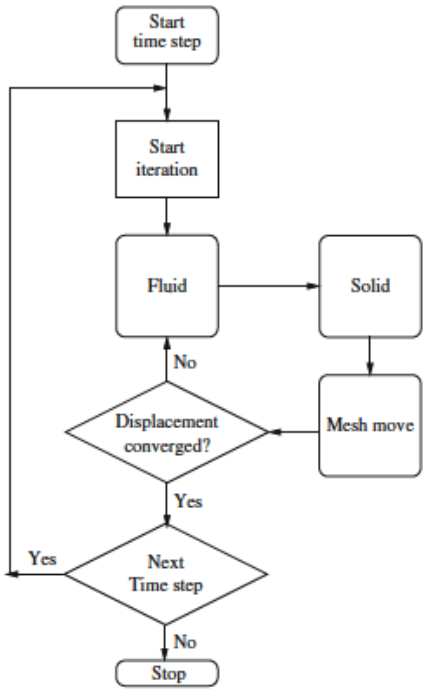

Figure 4.2: Schematic drawing of an implicit coupling scheme, (Zienkiewicz et al., 2013)

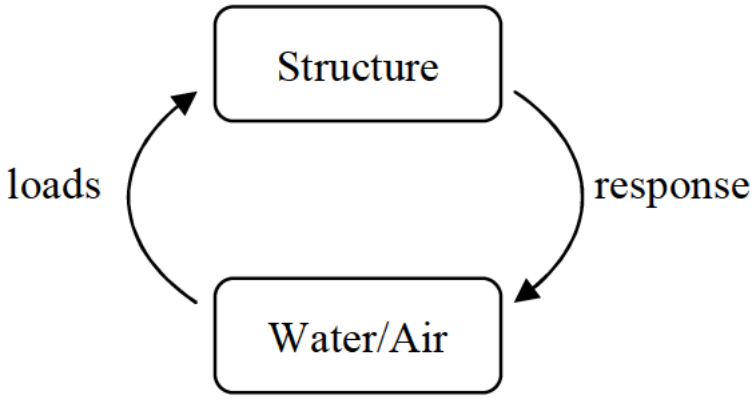

Figure 4.3: Schematic drawing of a two-way coupling scheme, (Bereznitski, 2002)

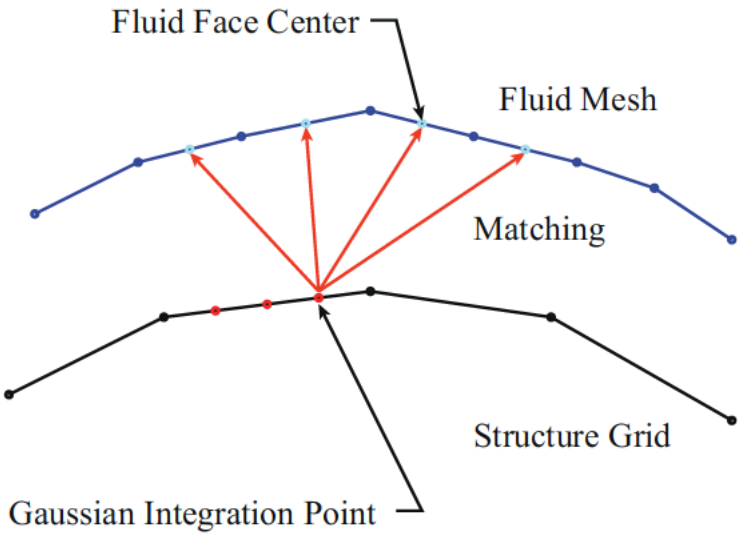

Figure 4.4: Schematic drawing of the mapping process between a structural mesh and a fluid mesh, (Piro and Maki, 2013)

utilized to solve a problem where it is necessary to account for hydroelasticity.

4.2.3 Dynamic Mesh Evolution

In an FSI analysis the structure will be imposed to deformations and rigid body motions. This indicates that a deformation of the mesh is necessary and we need to apply some techniques in order to properly adapt the mesh to the motion. One technique is known as morphing. Here, the fluid mesh vertices are moved in such a way that they stay conformal or mapped with the structural mesh nodes after deformation. In this way the nodes are topologically constant over time and a complete remeshing is not needed. In FEA, this is known as Arbitrary-Lagrangian-Eulerian (ALE) formulation. CFD uses a space-conservative law in order to obtain the arbitrary motion of the vertices while they stay conformal. The solver solves an additional transport equation to find the arbitrary motion. This "law" is able to describe the motion and deformation of the structure on the fluid mesh in such a way that there is still a conformal mapping between the models. In order to get the exchange of information to work we need to have a correspondence between the nodes in the fluid mesh and the nodes in the structural mesh. This is known as mapping and is essential if we want to transfer data correctly, (CD-Adapco, 2014). In figure 4.4 can we see an illustration regarding the mapping.

4.3 Hydroelasticity

Slamming is a phenomenon that occurs when an object, such as a wedge, experiences impact with water, leading to pressure peaks. Another definition of slamming is a rapid change in wetted surface, (Greco, 2012). The peak pressure has a small spatial extent and moves rapidly along the surface, (Faltinsen, 1999a). The fluid flow creates a spray root which is thin and moves

very fast. This makes tracking incredibly difficult and leads to difficulties for most numerical codes. The existing linear theories break down and we usually turn to non-linear boundary element method (BEM) theory or numerical tools, (Faltinsen, 2000).

There exists several types of slamming for ships; we mainly talk about bottom, bow flare, bow stem or wet-deck slamming, (Faltinsen, 2000). Wet-deck slamming is also named green-water impact, as it is associated with nearly horizontal slamming. Another type of slamming is sloshing. Sloshing arises due to large wave-induced vessel motion leading to slamming on tank walls. For lifeboats slamming is associated with water impact of the wedge-shaped hull or slamming on the deck house. There are also similarities between slamming on ships and offshore installations. On offshore installations breaking waves on a column of a semi-submersible can lead to vertical slamming. This can also be critical for marine risers. Another design aspect is the air gap. In order to prevent slamming from occurring on the bottom side of the deck.

There are several physical effects that arise during slamming. When the angle between the body and the water is small enough can air be entrapped, (Panciroli, 2012). From Greco (2012), we can observe that the compressibility of air influences the airflow and this airflow may influence the water flow, which again can influence the compressibility (water is usually assumed incompressible) of water. This compressibility may lead to an initial acoustic phase associated with a pressure peak, however this peak has a small time scale and will die out quickly. Other physical phenomenon may occur - air bubbles may collapse leading to a local hydroelastic effect. Other effects include that the entrapped air bubbles can start to oscillate due to compressibility leading to further vibration problems. The vibration of the structure and the pressure oscillation may lead to cavitation and ventilation. Cavitation means that the pressure is so low that the water starts to boil. This can typically happen if we are close to the free surface and the result is that we experience pressure oscillations. Ventilation means that the pressure is below the atmospheric pressure. The result is that air is attracted to the area with low pressure (between the structure and the free-surface), leading to further oscillation problems. In fluid-structure interaction experiments, according to Panciroli (2012) we can mainly observe two effects: (1) a repeated impact and separation of the fluid spray root between the fluid and the structure, (2) cavitation due to low pressure in areas of the wetted area.

Hydroelasticity is a study were the motion and distortion of deformable bodies due to environmental loads are assessed, (Panciroli, 2005). More specifically, it is the dynamic interaction between water and a structure, (Panciroli, 2005). The main characteristic of hydroelasticity is that the dynamic loading will be altered, and this is propagated through pressure vibrations and fast vibrations in the structure. Faltinsen (2000) showed that hydroelasticity is strongly dependent on the ratio between the load period or wetting time and the first natural periode of the structure. This means that hydroelasticity might occur during slamming, depending on the duration of the slamming event. If the load period is above the natural period, hydroelasticity can be neglected and the slamming load can be considered a quasi-static load, (Panciroli, 2005) and (Bereznitski, 2001). When the load period, is short we must consider the possibility that hydroelasticity might occur, (Faltinsen, 2000). Kapsenberg (2011) shows that a hydroelastic analysis of an elastic body will yield a lower magnitude of deformation compared to classical beam theory. In extreme cases, a quasi-static analysis can overestimate the deformation by a

factor of 10. Arai M. (1998) showed that a one-way interaction analysis provided reasonable results for a structure with a high rigidity, while a two-way interaction method was necessary in order to get a better prediction when the structure has a low rigidity.

According to Faltinsen (2005) can the hydroelastic slamming event be divided into two phases; the structural inertia phase and the free-vibration phase. Since it takes some time to accumulate deformations in the plate, the pressure load needs to balance the structural inertia forces. During impact, the plate will experience a large impulse in a short time compared to the eigenperiod. The consequence is that the space velocity of the plate is equal to zero, $\dot{w} - V = 0$. Here $\dot{w}$ is the plate velocity and V is the rigid body impact velocity. At the end of the structural inertia phase, the whole plate is wetted. The plate now starts to vibrate as a free-vibration wet beam with an initial velocity and zero deflection. The maximum strain occurs during the free-vibration phase. It has been shown that the details of the pressure distribution during the structural inertia phase is not important, but the size of impulse ($J = \int F dt$, F is the impact force, dt is time and J is the impulse) is. The very large pressures that appear initially are very sensitive to small alterations in physical conditions and they appear to behave somewhat stochastically. It has been shown that the variance among measured strain exists but is small for a given impact velocity, even though the maximum pressure was very different each time.

You may have understood that hydroelasticity implies a strong coupling between the hydrodynamic and structural problem. This means that the hydrodynamic loads influence and activate the structural elastic vibrations and eigenmodes. In return, these vibrations will influence the fluid flow and the pressure, which will affect the vibrations. Therefore, a strong implicit coupling is necessary, as described earlier in this chapter. A typical pressure-time plot will show a trend demonstrating that in the beginning, the pressure is associated with the slamming pressure, while afterwards the pressure will oscillate due to hydroelastic effect, (Greco, 2012).

The most important parameters in order to describe hydroelasticity according to Faltinsen (2000) are the deadrise angle α, impact velocity V, the first dry natural period of the structure T_n, the bending stiffness EI and the length of the beam or plate. Another important parameter is the ratio between the wetting time and lowest natural frequency of the structure.

Faltinsen (2000) developed a parameter to decide if hydroelasticity is important. He demonstrated that hydroelasticity becomes important when:

$$\tan\alpha < 0.25V\sqrt{\frac{\rho L^3}{EI}} \tag{4.1}$$

Or

$$R_F = \frac{\tan\alpha}{V\sqrt{\frac{\rho L^3}{D}}} \tag{4.2}$$

Figure 4.5 shows the nondimentional strains from a series of experiments. We can observe that for $R_F < 0.25$ do the structure experiences a fully elastic response while $0.25 < R_F < 1.5$ is a transition area. For $R_F > 1.5$ is the response quasi-static.

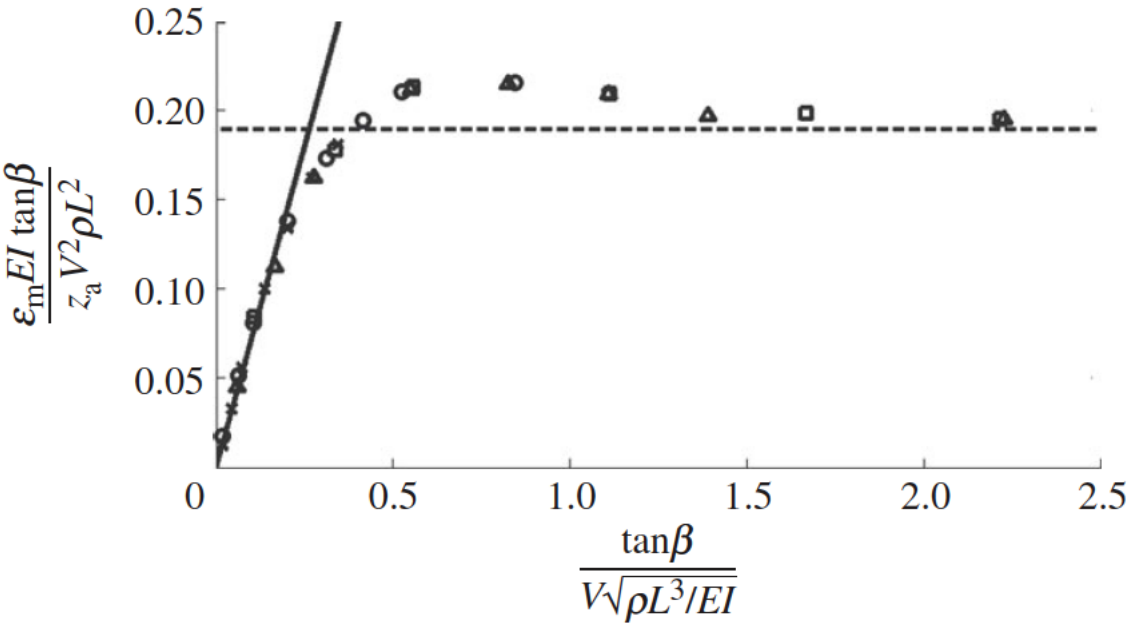

Figure 4.5: Nondimentional strain results with different impact velocities and deadrise angles from Faltinsen (1999b)

Panciroli (2005) rewrote the formula for a wedge consisting of composite plates:

$$R_P = \frac{\tan\alpha\sqrt{M}}{VT} \tag{4.3}$$

In figure 4.6 we can observe the nondimentional stress from a series of numerical simulations presented in Panciroli (2005). We can observe that when $R_P > 200$ the response of the structure is quasi-static.

Bereznitski (2001) reformulated the formula to be more general:

$$R_B = \frac{\text{duration}}{\text{period}} \tag{4.4}$$

Where *duration* is the duration of the load from a rigid CFD-analysis and *period* is the first dry natural period of the structure. An analogy for using the load duration is the difference when we load the structure with a load similar to a hammer blow or if we gently apply the load. If we load the structure quickly, in comparison to the eigenperiod, the structure will experience a shock and start to vibrate, but if we load it gently will it simply follow the load, since the inertia force is able build up. Figure 4.7 shows that that hydroelasticity becomes negligible when $R_B > 2$.

Here α is the deadrise angle, V is the impact velocity, E is the modulus of elasticity of the structural material (Young's modulus), ρ is the density of the water, L is the length of the beam/plate, M is the total mass of the structure, D is the bending stiffness (EI) and T is the first natural period of the structure.

The common denominator of these three methods is that they utilize the ratio between the load-

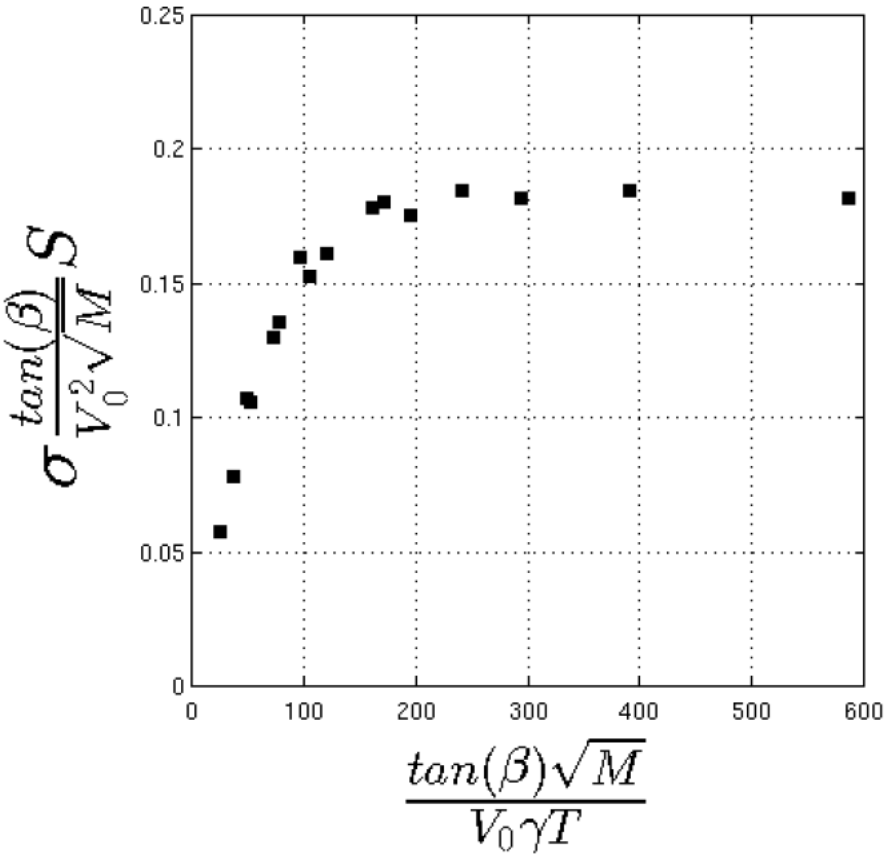

Figure 4.6: Nondimentional stress results from analysis in Panciroli (2005)

ing period and the first dry eigenperiod. The formula, developed by Faltinsen (2000), can give a quick estimation, while the formula developed by Bereznitski (2001), requires more knowledge of the problem. Bereznitski (2001) presents a procedure to determine if hydroelasticity should to be accounted for. This procedure can be viewed in figure 4.8 and the ratio is the factor R_B.

We can understand that when the response is regarded quasi-static, we can apply a one-way interaction analysis method in order to solve the problem. This is solved much faster than a hydroelastic problem. Based on this, one can easily understand why it is important to know when one should account for hydroelasticity. If the problem is regarded as hydroelastic, is it necessary to use a two-way interaction method. This is due to the strong coupling between the structure and the fluid when the fast vibrations appear. This approach is much more computationally expensive.

For a plate subjected to a hydroelastic load, we write the equation of motion as:

$$\bar{m}\frac{\partial^2 w}{\partial t^2} + D_x\frac{\partial^4 w}{\partial x^4} + 2B\frac{\partial^4 w}{\partial x^2 \partial y^2} + D_y\frac{\partial^4 w}{\partial y^4} = p(x,y,t,w) \tag{4.5}$$

Where $\bar{m}$, D_x, B and D_y is the mass and material properties of the plate respectively, $p(x,y,t,w)$ is the pressure as a function of the deflection w.

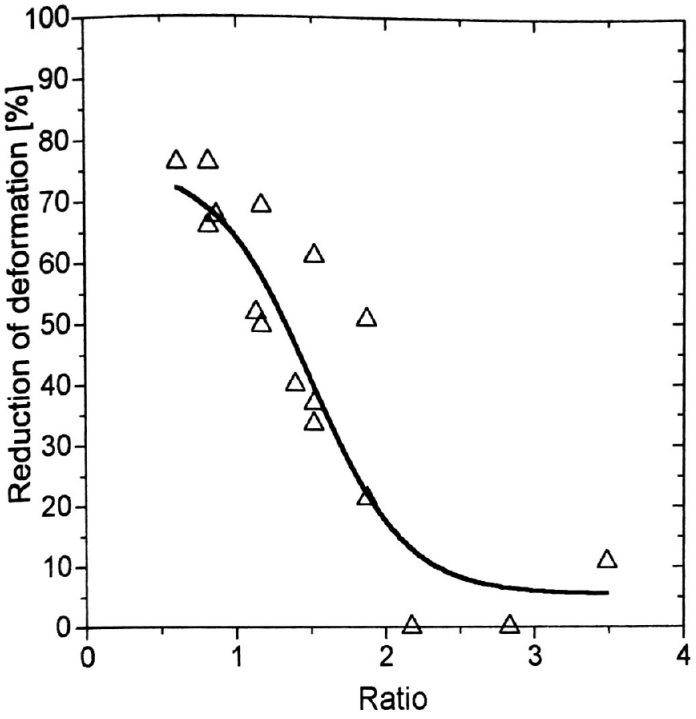

Figure 4.7: Comparing deformations from an FSI analysis to a quasi-static analysis, from Bereznitski (2001)

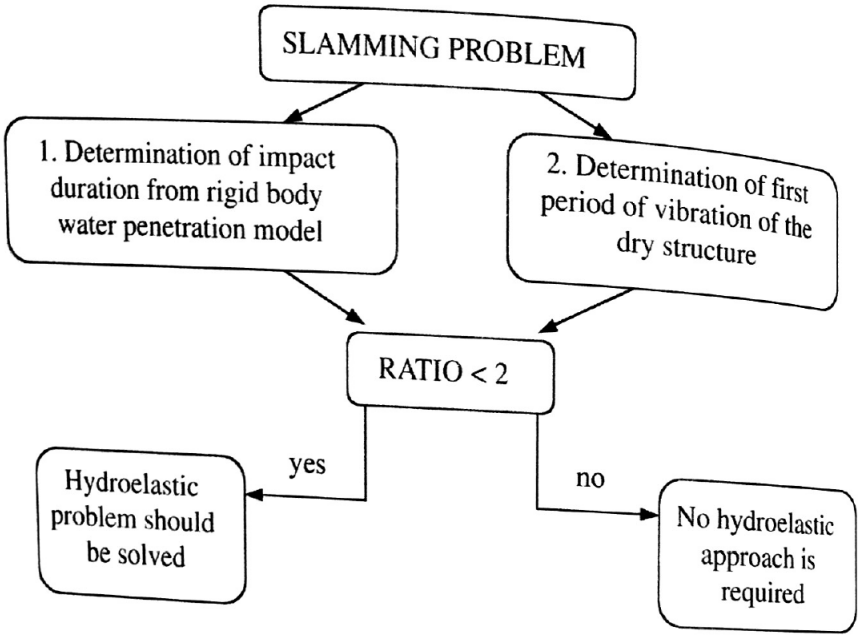

Figure 4.8: Procedure to determine when fluid-structure interaction may be important for structural response, (Bereznitski, 2001)

Chapter 5

Verification Study

5.1 Motivation

The scope of this master thesis is to use coupled FEM and CFD to find the importance of fluid-structure interaction on lifeboats. In order to capture the effect of hydroelasticity in numerical simulation, we need to perform a coupled analysis. Star-CCM+ and Abaqus will be used in order to describe the fluid-structure interaction when a conventional lifeboat experiences impact with water. The co-simulation engine developed by Simula will couple the two codes together. We use the CFD-solver to calculate the pressure acting on the structure and the FEM-solver to calculate the deformations due the pressure; the co-simulation engine is used to couple the two codes together.

Because CFD and FEM are numerical tools, we are required to verify if the software is able to produce correct and consistent results. Therefore, it is important to perform a verification study to verify whether the software is able to recreate a benchmark case. This study is also paramount to find the correct settings of the software such as time step, applied physical models, and mesh. It is normal to use existing benchmarks, such as recognized analytical theories, tests, or experiments to verify the software.

This chapter will focus on the creation of a numerical fluid-structure interaction (FSI) model and performing convergence studies. Secondly, the model will be applied on a benchmark case so the reader can gain confidence in the model. This is important, as the model will be used in the next stage of the thesis. In Handeland (2014) wedge was impact studied and the results from a numerical two-way fluid-structure interaction presented, the results were in good agreement with the benchmark case.

The reason for applying a two-way numerical fluid-structure interaction analysis is that a one-way or file coupled analysis is not fully able to recreate the acceleration and strain history. This was shown by Arai M. (1998).

In this thesis, the following has been assumed:

- Symmetry with respect to the z-axis (the y-direction is downwards)

- 2D theory can be applied

5.2 Benchmark Case

The benchmark case is based on a full-scale drop test of a conventional lifeboat, as described in Marintek (2011). An equivalent test can be viewed in figure 5.3. The manufacturer has chosen to remain anonymous, but the author was granted access to the test report. This test is based upon a series of standard tests. Marintek have installed four accelerometers in various positions during the tests. Their location can be viewed in figure 5.1. The test that will be

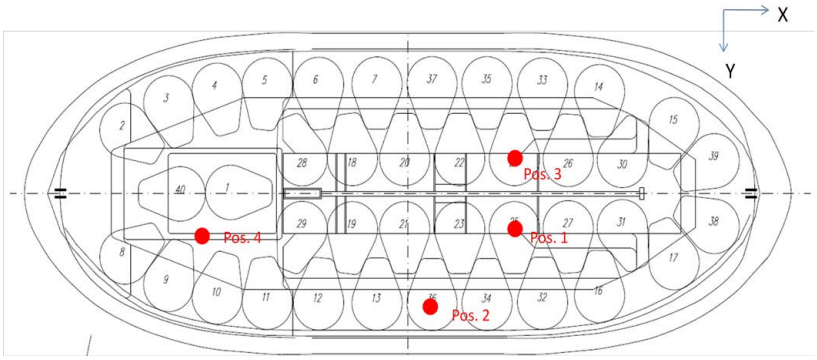

Figure 5.1: Locations of accelerometers in the full-scale test, (Marintek, 2011)

recreated is a free-fall drop test from 3 meters; a 2D-section will be based upon the location of the accelerometer in position 2 (see figure 5.1). The fairly homogeneousness of the hull at the location in position 2 makes the section suitable for a 2D analysis.

Figure 5.2: Lifeboat prior to free-fall drop of 3 m, (Marintek, 2011)

Figure 5.3: Impact during drop test of a conventional lifeboat, (Safety, 2015)

The lifeboat is 7.46 m long, 2.80 m wide and 3 m high. The total mass is equal to 8190 kg. The acceleration in position 2 in the 3 meter drop test can be viewed in figure 5.4. The logging

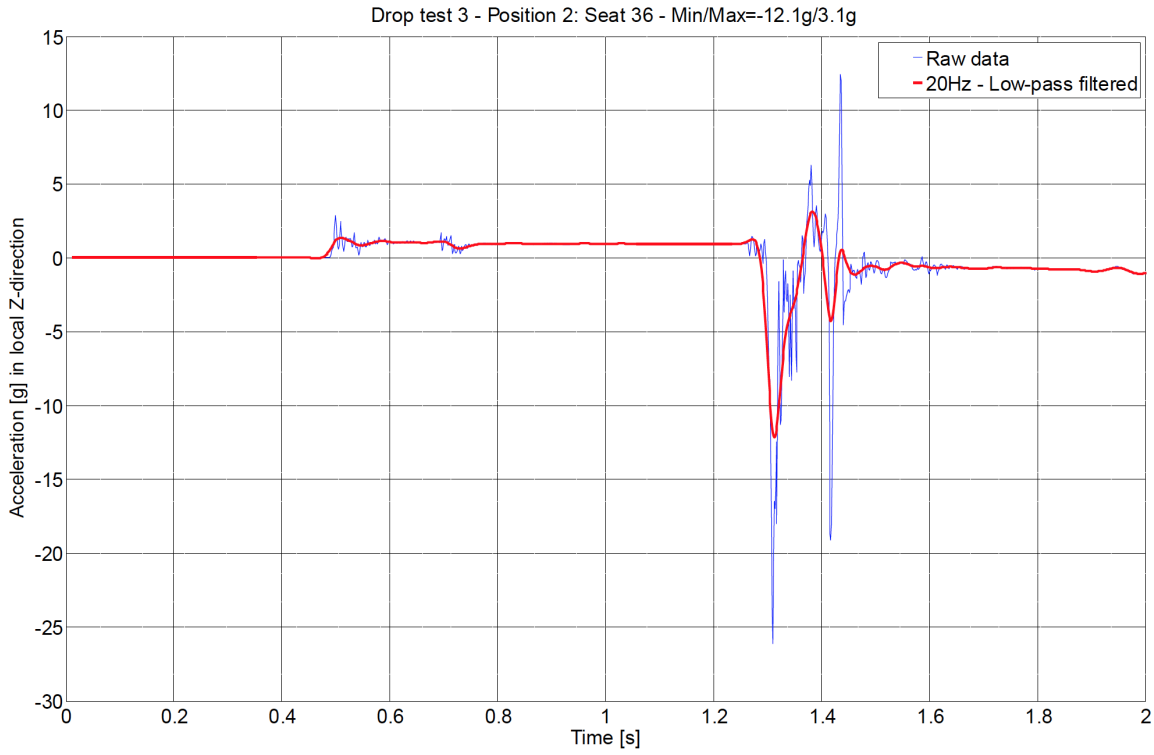

Figure 5.4: Acceleration in position 2 in the 3 meter free-fall drop test in Marintek (2011)

frequency was 800 Hz and an analog Butterworth low-pass filter with a frequency of 200 Hz was applied to the measured data.

An argument for evaluating the rigid-body deceleration is based on the work of Arai M. (1998). It was showed that the deceleration of the rigid body may have a strong influence on the stains. Based on the work it is important to develop a correct model to use in chapter 6.

5.3 Rigid Model

In order to create a numerical model that can be used in the fluid-structure interaction model, is it paramount to create a CFD-model and an FEM-model of the problem that is rigid and perform convergence studies on these models, (CD-Adapco, 2014). The applied loading and boundary conditions should be equal to the boundary conditions applied in the co-simulation model. Fedem have already performed a rigid analysis on the given lifeboat, (Fedem, 2011). They supplied a full FEM and CAD (Computer Assisted Drawing) model in 3D of the lifeboat. This was paramount in order to save time.

5.3.1 FEM-Model

As previously mentioned, a FEM-model of the lifeboat is supplied. This model is a detailed 3D-model of the hull. The mesh can be viewed in figure 5.5.

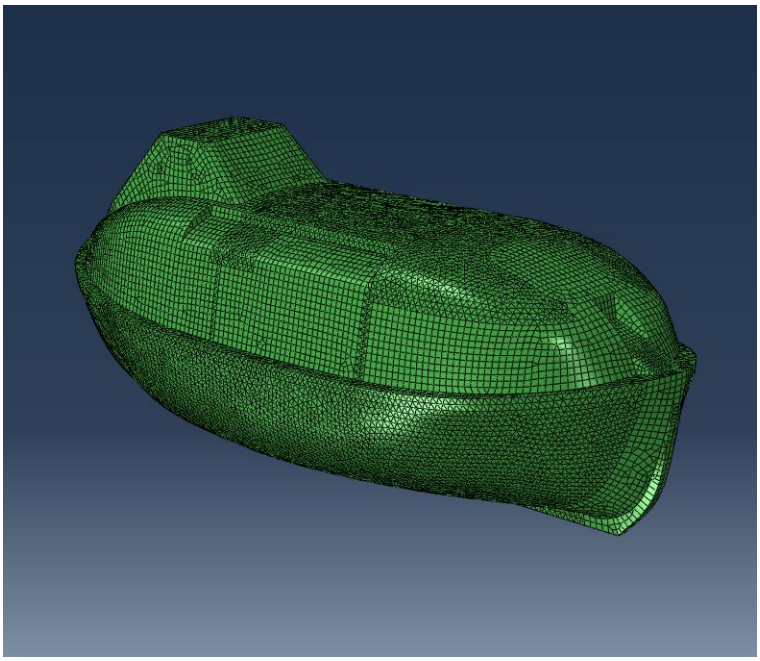

Figure 5.5: Structural mesh in 3D of the lifeboat

In order to create the 2D-model, the location on the hull where the accelerometer was placed in the full-scale test was located. Then a cutting plane was defined and the intersecting lines on this plane were projected to this plane, thereby creating a sketch. The sketch can be viewed in figure 5.6. This sketch was then extruded to create a shell body. The buoyancy foam is created by extruding the inner part to a solid body. The extruding depth is set to 50 [mm]. The model only has one part - which is computationally effective as it is not necessary to apply an interaction constraint. In addition, it is necessary to define the surface that will be coupled with Star-CCM+ later.

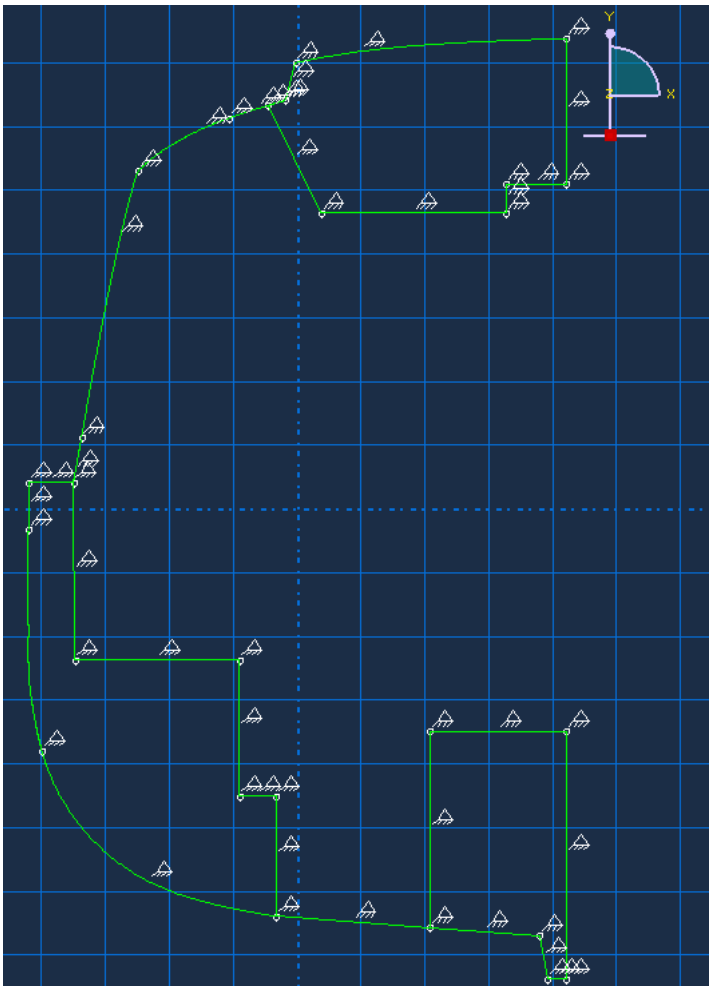

Figure 5.6: Sketch of 2D-section

Material Model

A modern lifeboat is normally constructed from composites or sheet metal. In this case, the lifeboat is made from laminate composites and buoyancy foam. Four different materials are present:

- Spray Laminate
- CSM
- Uni-directional Epoxy-Glass
- Buoyancy Foam

The material properties are extracted from Fedem (2011). Rayleigh damping is included as recommended by employees at Fedem. The values for the damping were found in Shim (1999) and Kyriazoglou (2007). The material properties are presented in appendix A.

With the material properties defined, it is possible to develop the sections in Abaqus. The analysis report, (Fedem, 2011), indicates that we need to develop ten different sections. One section is the solid buoyancy foam, while the nine others are composite shell section which are

defined in Fedem (2011). These are defined as described in the report with a local material coordinate system. This coordinate system can be seen in figure 5.7. This is necessary, as the materials are anisotropic. The sections are not presented due to anonymity.

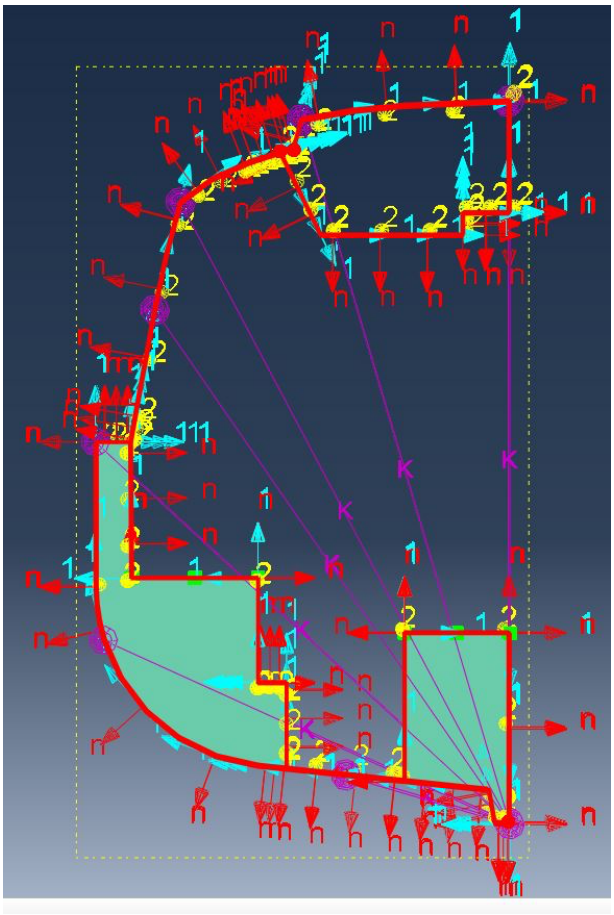

Figure 5.7: Local material coordinate system with springs

Non-linear Geometry

During the dynamic co-simulation, the section will be subjected to large rigid-body motion and displacements. It is important to turn on non-linear geometry in order to capture the change in geometry during impact. The non-linear geometry option is enabled in order to update the geometrical stiffness matrix due to the change in equilibrium.

Element Choice

The co-simulation engine demands that the model in Star-CCM+ and Abaqus is topological equal. It is necessary that the model in Abaqus encloses a volume.

Since the section encloses a volume, we can use both shell and solid elements. The solid section that contains the buoyancy foam is modeled using the solid C3D8R elements. This is an 8-node solid element with reduced integration in order to provide hourglass control. The

composite shell sections are modeled using S4R shell elements. This is a 4-node shell element with reduced integration in order to provide hourglass control and remove shear lock-in.

Static Convergence

In order to perform a convergence study, a pressure load was applied at the bottom of the lifeboat section. The load was set to 0.1 MPa. The load condition can be seen in figure 5.8. The

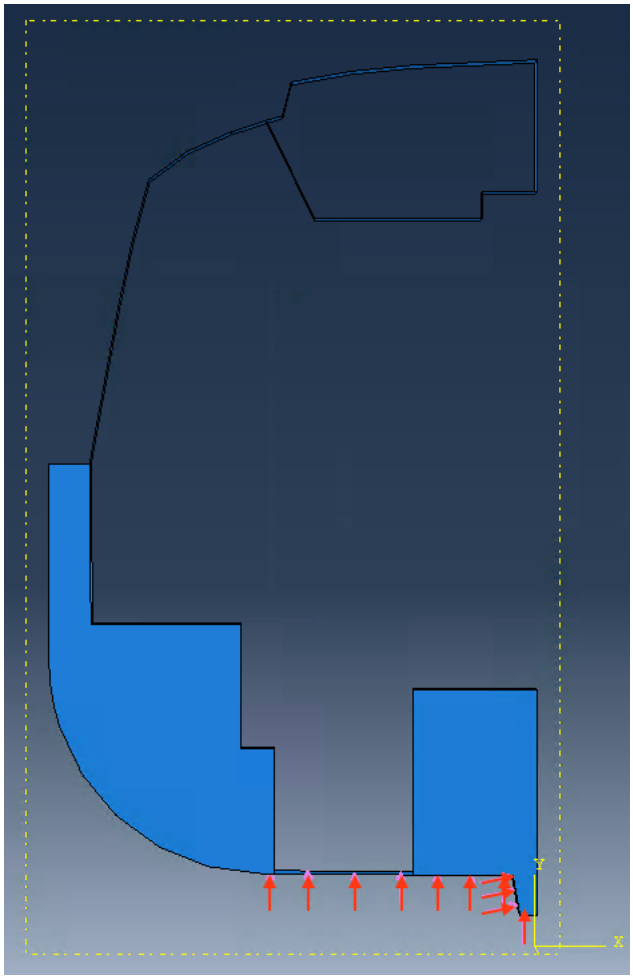

Figure 5.8: Applied static convergence load (arrows on the bottom of the structure)

boundary condition for the front and back is set to symmetry around the Z-axis, while the side on the right is defined as rigid (no rotation and translation). The stresses at a point on the keel and a point at the roof have been evaluated to determine convergence.

The global seed size dictates the mesh. This ensures that all the elements in the model are of approximately the same size.

In table 5.1 can we see the result of the convergence test for the FEM-model. Based on the theory presented in chapter 3, it is obviously preferable to choose the smallest global seed size. However, this is not the best choice considering the computational aspects of the problem. When you are dealing with a coupled analysis, a mapper will be present. It is important to create a mesh that will easily conform to the mesh in the CFD model. In this thesis, the two latter are

Table 5.1: Results of convergence study of FEM-model

Global Seed Size	σ_{Keel}	σ_{Roof}
10	23.39	8.48
20	23.00	8.60
25	22.80	8.67
30	22.60	8.75
40	22.22	8.85

regarded important as the next chapter will contain many simulations applied in a parametric study and we have to keep this in mind. We can also see that the difference in the stress at the keel from 25 to 10 is only 2.3 %. The difference is therefore neglected. The global seed size is chosen to be 25, as this gives two elements in the depth of the model and it gives reasonable answers compared to a finer mesh. The final mesh can be seen in figure 5.9.

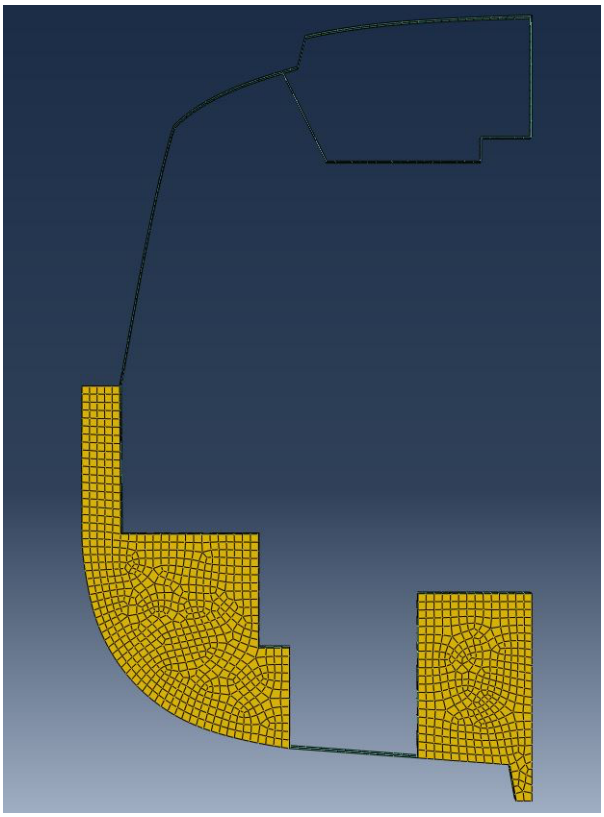

Figure 5.9: Final FEM mesh

Eigenvalues

Since the structure is complex, it will have several eigenmodes. Table 5.2 shows some of the first eigenmodes of the structure. Due to the presence of springs, several of the eigenmodes will appear unrealistic. In figure 5.10, we can see the first dry eigenmode and in figure 5.11 can we see an unrealistic eigenmode.

Table 5.2: Eigenfrequencies of the structure

Mode	Eigenfrequency [Hz]
1	5.51
2	5.85
3	8.63
4	10.3
5	16.6
6	20.3
7	34.4

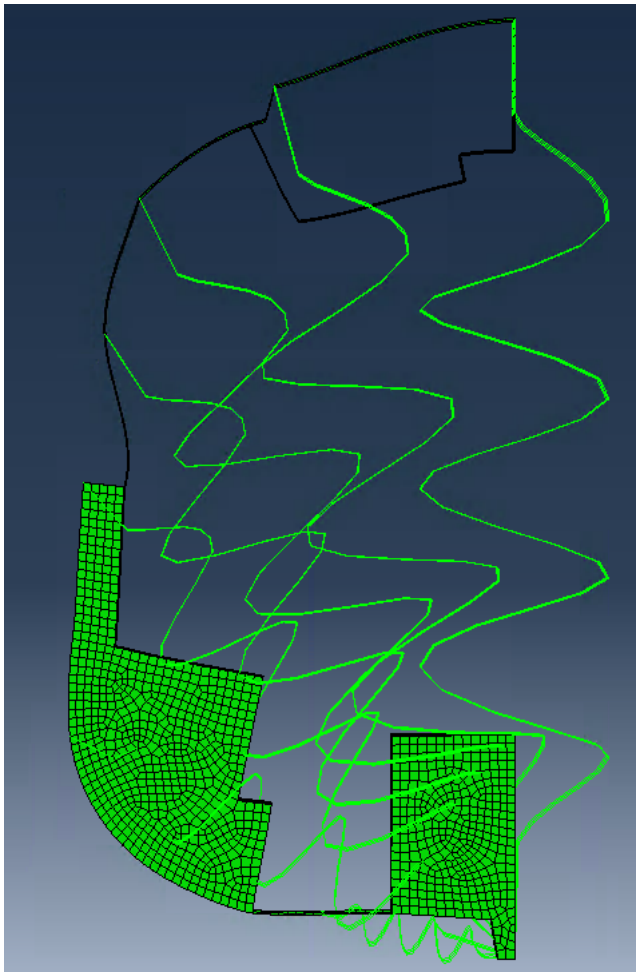

Figure 5.10: First dry eigenmode - 5.51 Hz. Note that the springs are viewed in this figure

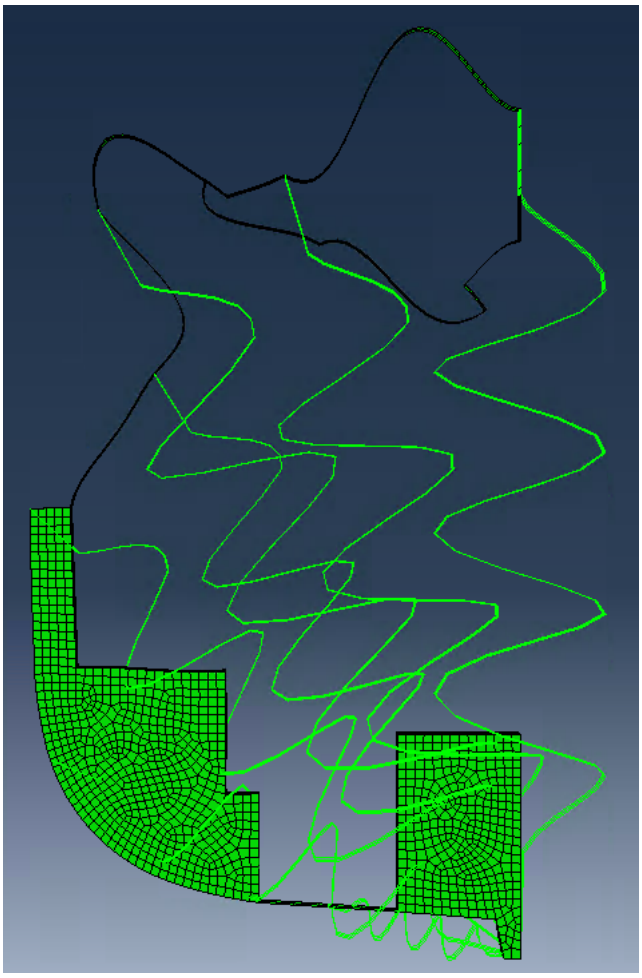

Figure 5.11: A unrealistic eigenmode - 38.4 Hz. Note that the springs are viewed in this figure

5.3.2 CFD-Model

Geometric Model

The CFD-model is based on the FEM-model. The final assembly is exported as a CAD-body and then imported into Star-CCM+. This CAD-body is further processed in Star-CCM+. The sheet body from Abaqus is transformed into a solid body and a boolean operation subtracts the solid body from a solid box named *overset mesh*. In this way, the wet surface on the hull will still be defined and we can easy create the overset mesh region. This method assures that the surface in the CFD model is exactly the same as the coupled surface in the FEM-model, which is required by the mapper.

As mentioned, the CFD-model incorporates an overset mesh region. The region is connected to the wet surface of the hull. The size of this region is created in such a way that there is at least 0.75 m from a point on the wet surface to the outer part of the overset mesh region. This makes the region 2.15 m wide and 4 m high.

In the rigid case, the keel is 3 meters above the free surface in order to determine the impact velocity, which is going to be used in the flexible model. In the flexible case, the model will be translated to 10 cm above the free surface in order to save computational time.

As mentioned, the hull section is now placed within an overset mesh domain and this domain is again placed within a background mesh region. This is very convenient, as we only have to apply the morpher within the overset mesh domain, which will save computational load. The hull is subject to free-fall using a body-fixed mesh combined with the *DFBI-Rotation and Translation* model to simulate the behavior of the section during free-fall and impact. The section is assumed to weight 27.446 kg, this is based upon the report (Fedem, 2011). Table 5.3 can be related to figures 5.12 and 5.13. The first six boundary conditions are related to the background mesh, while the last three are related to the overset mesh box. The overset mesh box can be viewed in the figure 5.13. The WetSurface is indicated in figure 5.13, while the Overset Mesh Interface is not indicated in the figure.

Table 5.3: Boundary Conditions for rigid hull

Name	Boundary Condition	Boundary Specification
Bottom	Velocity Inlet	Velocity of Flat Wave
Top	Pressure Outlet	Hydrostatic Pressure of Flat Wave
SideLeft	Symmetry	[-]
Front	Symmetry	[-]
Back	Symmetry	[-]
SideRight	Symmetry	[-]
WetSurface	Wall	No-Slip
Symmetry	Symmetry	[-]
Overset Mesh Interface	Overset Mesh	[-]

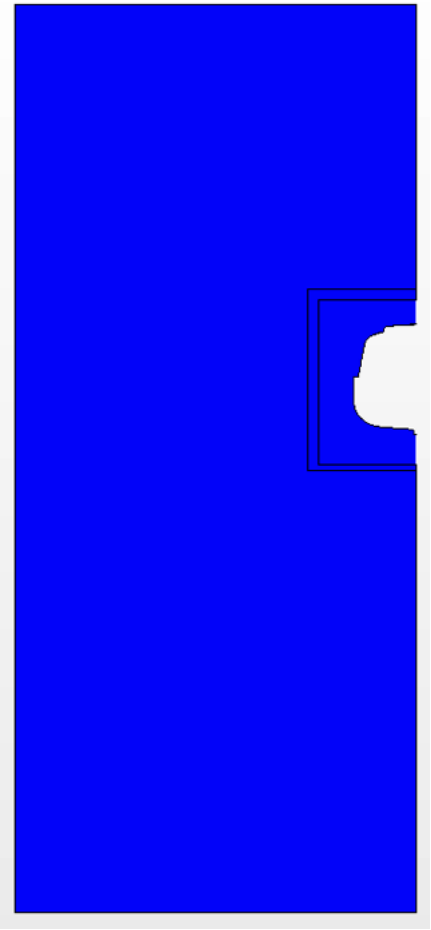

Figure 5.12: Domain used in CFD calculations

Mesh

The model consists of two different mesh continua - one for the background region and one for the overset mesh region. This is done due to the requirement specified in CD-Adapco (2014). The following mesh modules have been applied in order to create the mesh *Surface Remesher*, *Trimmer Mesher* and *Prism Layer Mesher*. The *Prism Layer Mesher* is crucial to capture the boundary layer and spray root that is created during the impact phase. It should be noted that the *Prism Layer Mesher* is only applied to the overset mesh region. This is due to the lack of walls in the background region. A volumetric control has been added at the location of the free surface. The mesh size is 7.5 % of the base size in the background mesh region.

The mesh is configured in such a way that the background domain and the overset domain mesh size are linked through the base size in the background mesh continua. The base size in the background region is denoted x while the base size in the overset mesh region is $\frac{1}{4}x$.

In table 5.4 and 5.5 can we see important properties and values of the initial mesh. While figure 5.14 and 5.15 displays the final mesh. A surface mesh refinement on the wet surface is included as specified in table 5.4. The mesh is created in such a way that when the base size changes, the surface mesh size on the wet surface will also change. This will also alter the growth from the hull. This approach also implies that a change in the base size will quickly reduce or increase

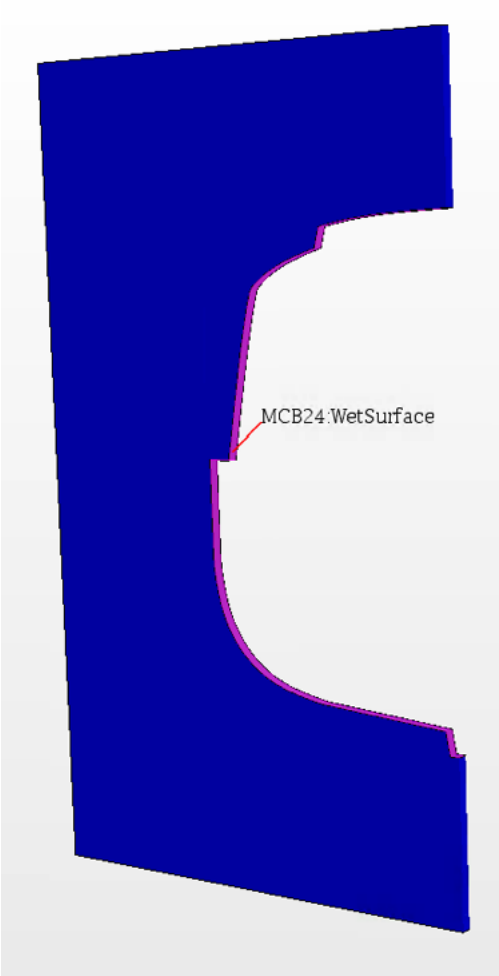

Figure 5.13: Close up of the Overset Mesh Region, the WetSurface is marked in purple

Table 5.4: Important Parameters regarding the initial mesh

Parameters	Value
Base Size	0.5 m
Template Growth Rate	Very Slow
Minimum Surface Size WetSurface	25 % of base size
Target Surface Size WetSurface	25 % of base size
Prism Layers	15
Prism Layer Stretching	1.1
Prism Layer Thickness	0.075

Table 5.5: Initial domain size

	$x_{min}[m]$	$x_{max}[m]$	$y_{min}[m]$	$y_{max}[m]$	$z_{min}[m]$	$z_{max}[m]$
Domain	0.0	-5.0	-6.5	7.5	0.0	0.05

the number of cells in the domain. The thickness of the prism layer is kept constant in order to secure that the prism layer not is too high or too low, in order to capture the boundary layer and spray root.

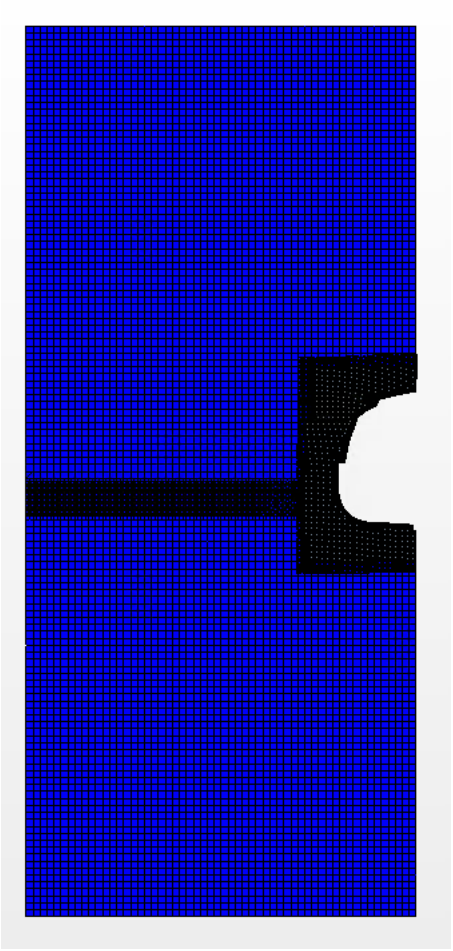

Figure 5.14: Mesh used in CFD-calculations

Physics

In order to model the full-scale test we need to choose the proper physical modules in Star-CCM+. In figure 5.16 can we see the physical modules that were applied in the rigid CFD analysis. It is believed that these are able to capture the physics behind the test. Turbulent flow has not been modeled as the full-scale test is of short duration and this will probably not affect the result significantly. This was also demonstrated by Johannessen (2012). The air phase is modeled, as this will probably influence the results due to the present of an air cushion. The air is present for all simulations of this thesis. This is in accordance with Bereznitski (2001).

Numerical Parameters

Table 5.6 shows the most important numerical parameters applied. A study regarding numerical parameters (except time step) has not been performed, as these values are obtained from Johannessen (2012).

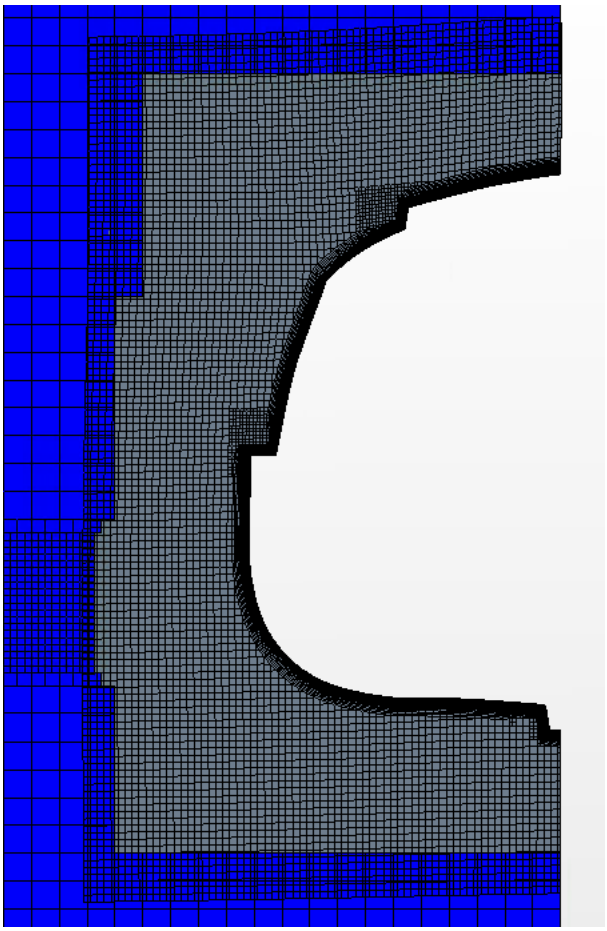

Figure 5.15: Close up of the mesh in the Overset Mesh Region during Co-Simulation

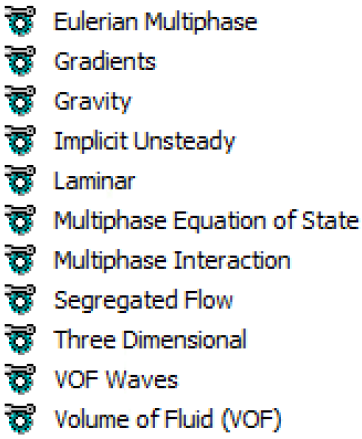

Figure 5.16: Selected physical modules for rigid CFD analysis

Convergence study - Domain Size

One can observe from figure 5.2 that the boat is dropped close to a wall but there is no information regarding the distance from the wall. It is assumed that the wall will not affect the final acceleration significantly. This assumption is questionable, as it will probably influence the pressure, but it is not know by the author how this will influence the accelerations. Thus the lifeboat is dropped in an infinite fluid. This means that the domain size has to be large enough

Table 5.6: Numerical solution parameters

	Parameters	Chosen
Physics - Segregated Flow	Convection	2nd-order
Physics - Volume of Fluid	Convection	2nd-order
Solver - Implicit Unsteady	Temporal Discretization	1st-order
Solver - Implicit Unsteady	Time Step	0.0001 s
Solver - 6-DOF Solver	Number of Iterations	6
Solver - Segregated Flow	Under-Relaxation: Velocity	0.8
Solver - Segregated Flow	Under-Relaxation: Pressure	0.2
Stopping Criteria - Iterations	Number of Inner Iterations	15
Stopping Criteria - Total Solving Time	1.3 s	

so that the domain does not contaminate the result. In addition, we need to consider the number of cells and computational time as well.

In order to determine the best suited domain, we need to perform a couple of simulations with different domains. This is important, since the domain size may influence the results due to contamination the boundary conditions may inflict. Since the problem is symmetric with respect to the right side, the height of the domain will be changed, while the free surface is kept constant. The width of the domain is also altered by moving the left boundary. The depth of the domain will be kept constant as specified in the FEM-model - this should not influence the solution, as a symmetry condition on both sides (front and back) has been applied.

Table 5.7: Results from convergence study regarding domain

	Corner 1[m]	Corner 2[m]	Cells	Solving Time [h]	P_{max} [kPa]
D1	(0.0, -7.5, 0.0)	(-7.0, 8.5, 0.05)	42834	1.93	470.5
D2	(0.0, -6.5, 0.0)	(-5.0, 7.5, 0.05)	38410	1.65	487.6
D3	(0.0, -5.5, 0.0)	(-3.0, 6.5, 0.05)	32458	1.49	469.9

In table 5.7 and figure 5.17 and 5.18, we can see the results of the convergence study. The smallest domain (D3) is a poor choice, due to the noise at the end of the signal when we look at the translation of the hull in figure 5.18. This domain is then discarded. We can see in figure 5.17 and table 5.7 that D2 overestimates the pressure with respect to D1. Since this domain is smaller, a probable cause can be contaminations due to the size. Therefore D2 is discarded. Then D1 and the largest domain is the best choice.

Convergence study - Mesh Size

The convergence study of the mesh is performed with different sizes of the base size in the background mesh region. The link between the overset mesh region and background region still exists.

We can observe in table 5.8 and figure 5.19 and 5.20 the results from the mesh convergence study. It can be seen that M1 overestimates the maximum pressure, while M3 underestimates the pressure with respect to M2. The difference $\Delta P = 21$ kPa is not that significant and the

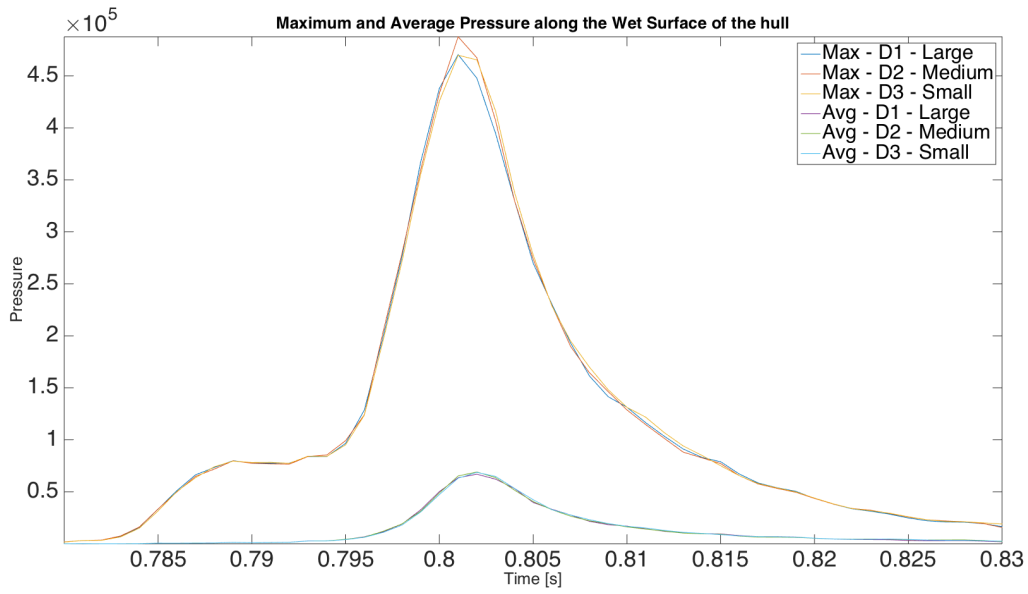

Figure 5.17: Time series of maximum and average pressure along the wet surface of the hull - convergence study regarding domain size

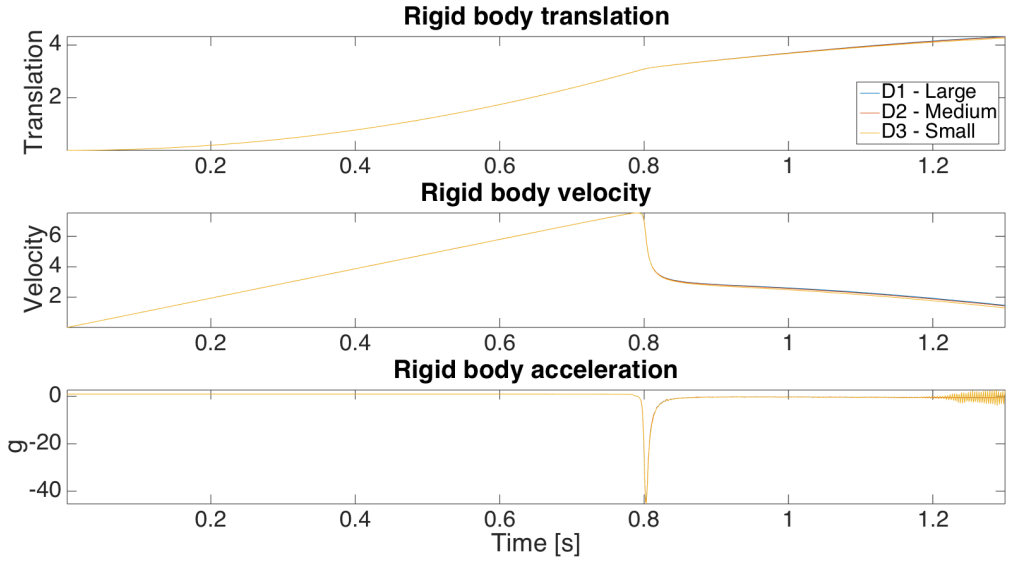

Figure 5.18: Time series of translation, velocity and acceleration of the hull - convergence study regarding domain size

Table 5.8: Results from convergence study regarding mesh size

	Base Size [m]	Solving Time [h]	P_{max} [kPa]	Cells
M1	0.50	1.65	487.6	42834
M2	0.25	5.48	466.6	169869
M3	0.75	0.69	440.0	20486

computational time is 3.3 times longer for M2 than M1. The overestimation can be regarded as a good trade off due to the demand of computational power when performing a co-simulation

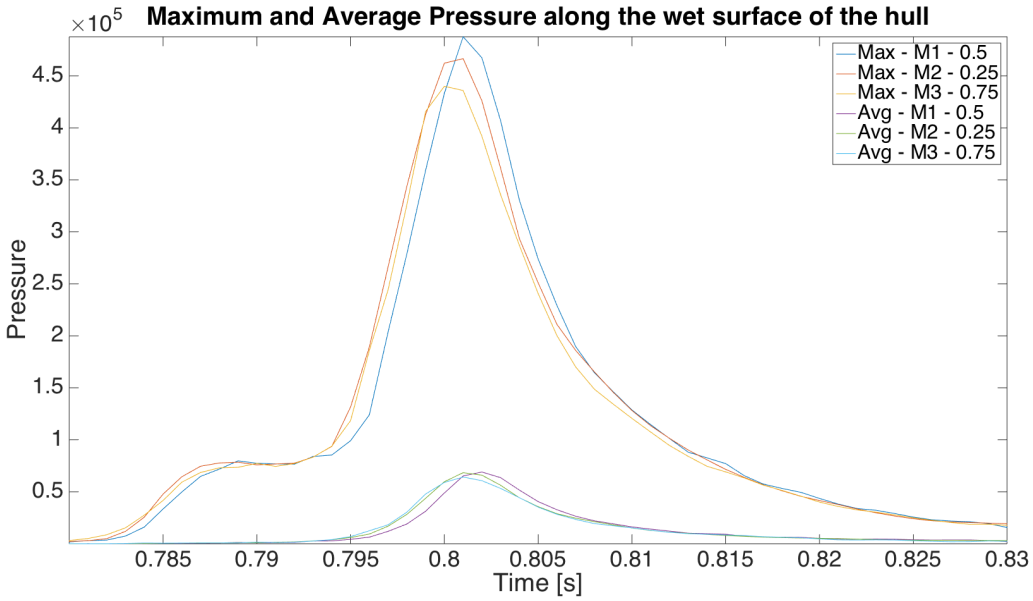

Figure 5.19: Time series of maximum and average pressure along the wet surface of the hull - convergence study regarding mesh size

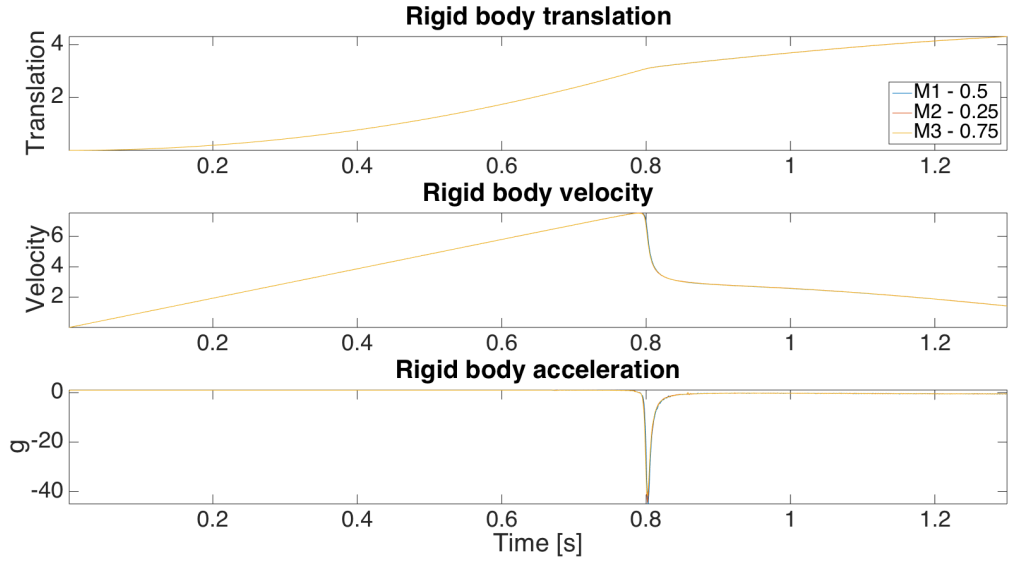

Figure 5.20: Time series of translation, velocity, and acceleration of the hull - convergence study regarding mesh size

analysis. We must note that the size of the pressures have been shown to be of less importance, (Faltinsen, 2005), since it is the impulse of the impact load that is important. The pressure difference between M2 and M3 is 27 kPa, while the M3 is roughly twice as quick as M1. If we consider the average pressure obtained for M1 and M2 are they fairly equal, while M3 clearly underestimates the average pressure on the hull. It is uncertain if M3 is fully capable to the boundary layer and spray root due to the size of the cells. Since M1 is much faster and the difference in P_{avg} is not that large, M1 is preferred. The final mesh can be viewed in figure 5.14 and 5.15.

Convergence study - Time Step

It is important to choose an appropriate time step in slamming analyses. Due to the short duration of the pressure peaks, it is important to have a small time step in order to capture them.

Table 5.9: Results from convergence study regarding time

	Δt	Solving Time [h]	P_{max} [kPa]	$CFL_{\max}$
T1	$1{\cdot}10^{-3}$	1.93	470.5	55.2
T2	$5{\cdot}10^{-4}$	2.83	672.7	28.1
T3	$2.5{\cdot}10^{-4}$	4.96	1105.5	27.7
T4	$1{\cdot}10^{-4}$	7.42	1580.3	9.1
T5	$2{\cdot}10^{-5}$	28.09	1972.2	1.9

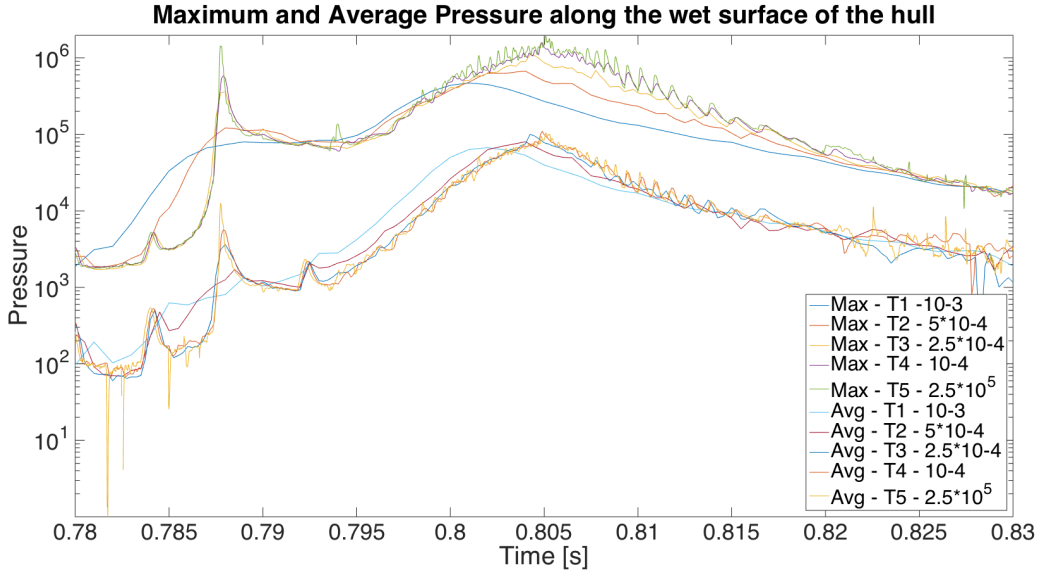

Figure 5.21: Time series of maximum and average pressure along the wet surface of the hull - convergence study regarding time step

In table 5.9 and figure 5.21 and 5.22 one can observe the obtained results from the time step convergence study. One should note that the Y-axis on figure 5.21 is on a logarithmic scale. This is done out of convenience, as it is easier to interpret the graph this way due to pressure oscillations. We can immediately see from figure 5.21 that T1 and T2 are not able to capture the pressure peak that appears around 0.787 s. This is also evident when looking at the average pressure. These two time steps are therefore discarded. Due to the very long computational time, T5 is discarded as well, as the size of the impulse probably is fairly equal, this is regarded a reasonable decision. One can observe the difference between T3 and T4 in figure 5.21 - the difference is most evident when we consider the maximum pressure. If we consider the average pressure, the difference is much smaller and the trend of the results follow each other closely. The maximum pressure represents the maximum pressure at a single cell on the hull, while the average pressure represents the surface averaged pressure along the whole hull. The average pressure is a better comparison method in this case, as we deal with noise (oscillations) in the signal and it is more important from a structural point of view than a singular pressure peak

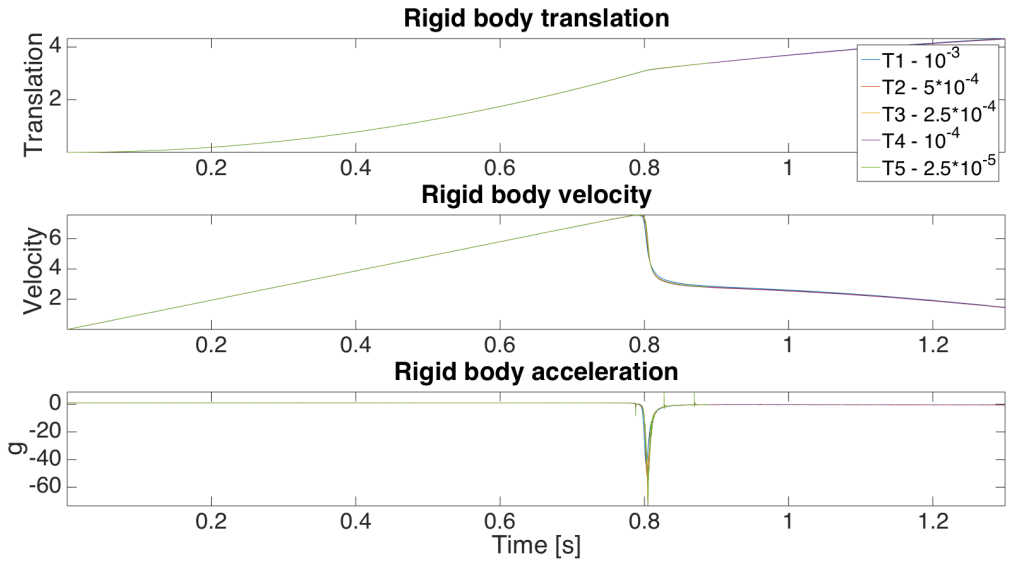

Figure 5.22: Time series of translation, velocity, and acceleration of the hull - convergence study regarding time step

- see chapter 4.3. Based on this, T3 should be the better choice as the computational time is shorter and the average pressure is very equal to T4 and T5.

Final model

After the convergence study regarding domain size, mesh size, and time step the following has been implemented in the final model. It has been chosen to use domain size D1, mesh size M1 and time step T3. Figures 5.23 and 5.24 shows the final model. Note that mesh refinement at the free surface has been applied.

In figure 5.25 and 5.26 the results from the final model can be seen.

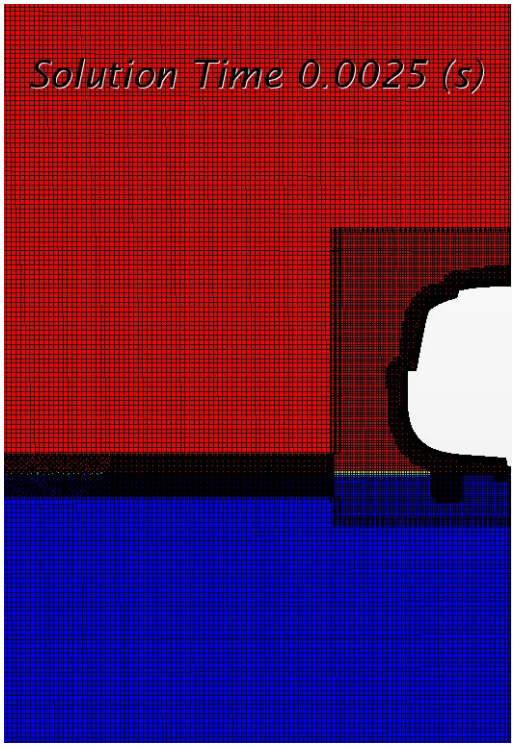

Figure 5.23: A snapshot of the VoF-solution at $t = 0.0025s$ displaying the mesh far away

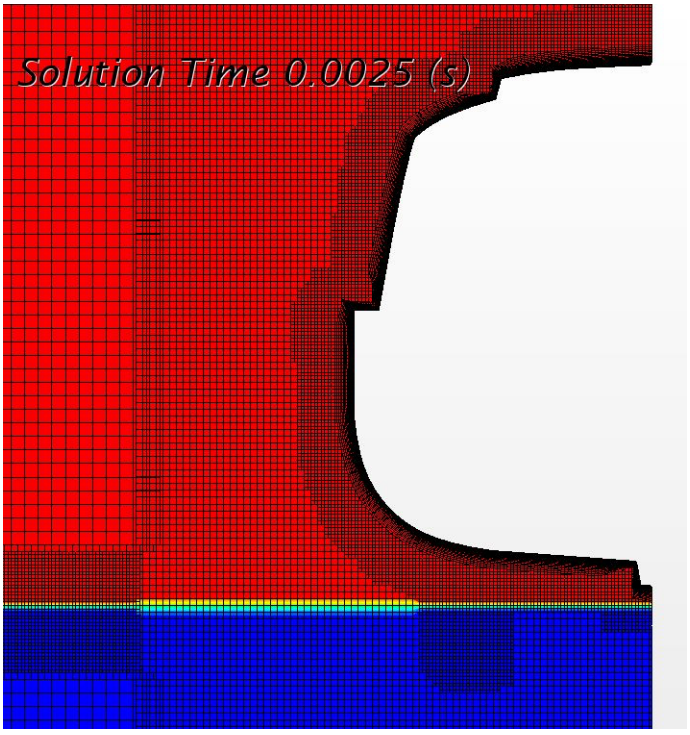

Figure 5.24: A snapshot of the VoF-solution at $t = 0.0025s$ displaying the mesh close

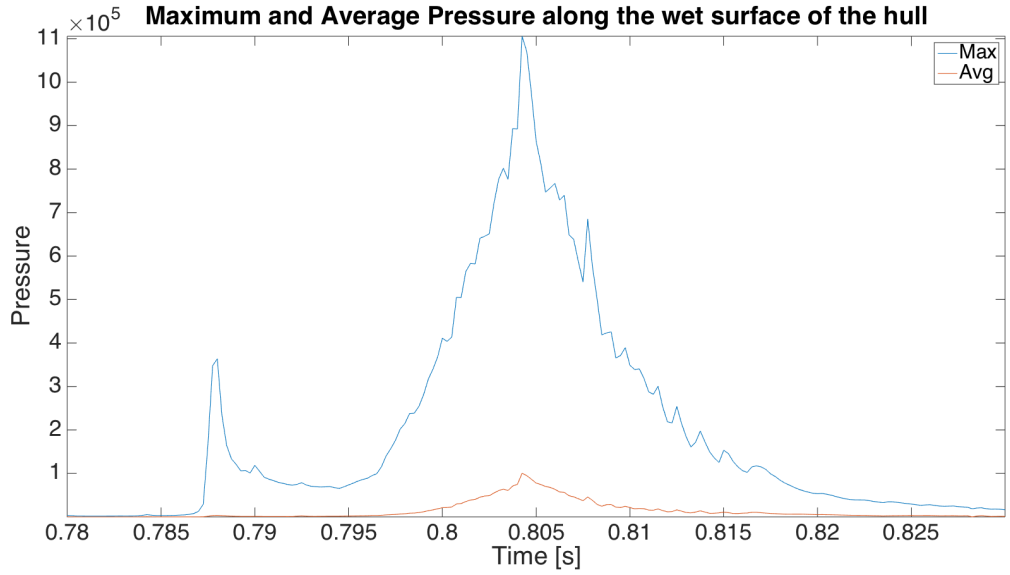

Figure 5.25: Maximum and average pressure along the wet surface from the final model

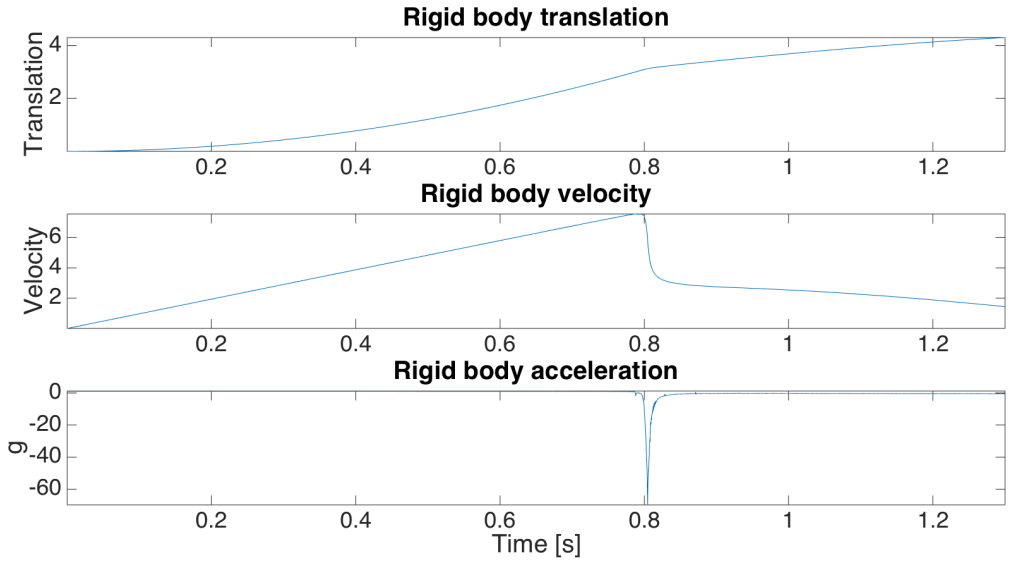

Figure 5.26: Response of the hull from the final model

5.4 Flexible model

In order to perform a FSI-analysis using Star-CCM+ and Abaqus have a co-simulation engine been developed that enables topological mapping between the two codes and therefore is capable to exchange information.

What basically is done is that the engine creates a conformal mapping between the models in the two codes - this requires that the models are geometrical equal. The engine creates a correspondence between the nodes and cells in the CFD-model and the nodes (integration points) and elements in the FEM-model. This is essential in order to get the two codes "talking". Further we must define what information that is going to be transferred.

It have been defined that Star-CCM+ is going to export the pressure and wall shear force, while Abaqus is going to export the nodal displacement. It have further been decided that the coupling should be implicit since the problem is a two-way interaction problem which is strongly-coupled. Since slamming is phenomenon that is highly coupled, a scheme like this will be highly advisable.

As mentioned earlier, it is necessary to perform a coupled or two-way analysis, since a one-way analysis is not able to predict the elastic response on a low flexural structure in a satisfactory manner, (Arai M., 1998).

To perform a co-simulation analysis some changes have been made to both the CFD-model and the FEM-model. This chapter quickly explains the main differences.

According to Bereznitski (2001), the response of a structure can be regarded as hydroelastic when the ratio between the duration of the load and the first dry eigenperiod is below two. If the ratio is above, the hydroelastic effect will not play an important role. The formula is defined in equation 4.4. In figure 5.25 we can make a quick estimation of the loading period. The load duration is estimated as approximately $0.035[s]$. From the eigenfrequencies in table 5.2 can we find the maximum ratio $R_B = \frac{0.035}{\frac{1}{5.51}} = 0.193$. As this value is below 2.0, hydroelastic response is regarded as important.

5.4.1 FEM-model

Initial Conditions and Boundary Conditions

The model is subjected to two boundary conditions. First, a symmetry condition in x-direction on the right side is applied. This allows the model to freely translate in the vertical direction and impose a symmetry condition in order to reduce the number of elements. Secondly, a symmetry condition in z-direction is applied on the front and back of the model. This corresponds with the assumption that the hull at the location is homogenous and 2D theory can be applied.

The whole model is translated to 10 cm above the free water surface and given an initial velocity field equal to 7.452 $[\frac{m}{s}]$ to save computational time. The initial velocity is obtained from the rigid CFD analysis. When the structure reaches a distance a little less than 10 cm above the free

surface, an increase in the pressure appears due to the compressibility of air; this is the reason why 10 cm is chosen. The model is also subjected to a gravity load.

The surface that will be coupled with Star-CCM+ has been defined. The surface is the outer side of the shell sections that evolves the hull. It is denoted *WetSurface*.

In addition, a *Dynamic - Implicit* step in Abaqus is applied. This was done in order to allow dynamic structural analysis. The initial time step guess is defined as $5 \cdot 10^{-5}$. Non-linear geometry is activated.

Additional Mass

Sandbags were placed on seats in the lifeboat during the full-scale test in order to simulate the weight of people who would be seated in the event of an evacuation. The total mass of the full scale lifeboat will therefore consist of the weight of the hull and the sandbags. The green areas in figure 5.27 represent the applied sandbags in the 2D-model. The sandbags are represented as non-structural mass in the Abaqus model.

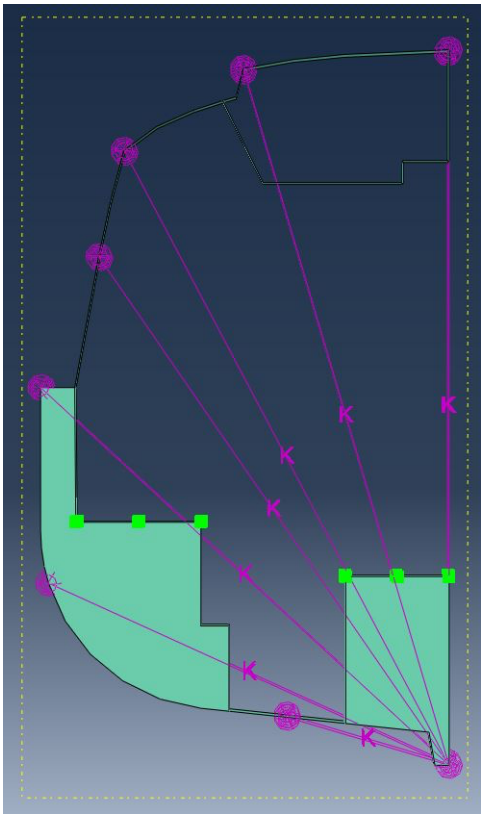

Figure 5.27: Abaqus model with sandbags and springs

It was assumed that the weight was evenly distributed along the hull of the lifeboat in order to find the additional mass. This was mainly done due to the fact that the weight distribution along

the hull was not known. This yielded a total mass of the section equal to:

$$\begin{aligned} m_{\text{total}} &= 8190\text{kg} \\ L &= 7300[\text{mm}] \\ L_{\text{section}} &= 50\text{mm} \\ m_{\text{section}} = \frac{m_{\text{total}}}{L} \cdot L_{\text{section}} &= 27.446\text{kg} \end{aligned}$$

These values are from Fedem (2011). After analysis and discussion with employees at Fedem, it was concluded to be an incorrect assumption, as there existed huge differences between the obtained accelerations and the benchmark. This is mainly due to the fact that the weight was not evenly distributed along the lifeboat (as expected).

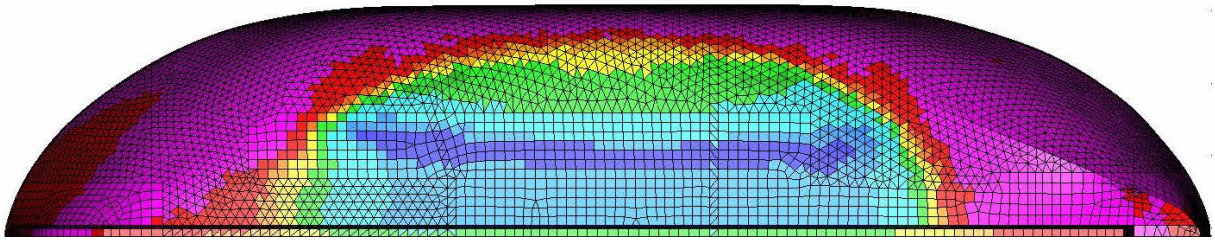

Figure 5.28: Pressure from rigid CFD analysis, (Fedem, 2011)

The other reason is a more physical reason linked with Newton's second law ($\vec{F} = \frac{d(m\vec{V})}{dt}$). Where m is the mass, $\vec{F}$ is the sum of forces and $\vec{V}$ is the velocity - the two latter are on vector form. As the benchmark shows only the acceleration, this law is particularly important. The pressure does not act uniformly along the whole keel of the lifeboat when it experiences impact with water. The significant part of the pressure acts only in an area in proximity to the middle of the lifeboat - see figure 5.28. If we neglect the gravitational force for a moment when considering slamming (an assumption in Greco (2012)), we have only two forces that act on the hull - the inertia forces though the center of gravity due to the acceleration, and the pressure force. A translation of the mass will appear - this means that in order to obtain force and moment equilibrium, the mass, which is distributed towards the ends, will experience a translation towards the center of the lifeboat. The same thing happens in real life if we consider a beam which has a pressure load along the middle - the ends will experience a deflection and thus translates the mass at the ends.

This phenomenon makes it difficult to find the correct mass for the 2D section. However, since the final result is known, we can apply this to find an equivalent mass of the 2D-section. If we assume that there exists an unbalanced inertia force due to the virtual translation of mass in 3D, this means that the mass in 2D would increase accordingly. Hence can we apply Newton's second law to find the unbalanced inertia force. It is also necessary to assume that the pressure force is equal in 2D and 3D. We cannot use equilibrium to find the unbalanced inertia force if the pressure force not is equal. One realizes that this s to be an iterative procedure. It is possible to find the change in equivalent mass using Newton's second law:

$$m_{\text{eq}}^{i+1} = m_{\text{eq}}^{i} + \Delta m_{\text{eq}} \tag{5.1}$$

Now we can find the change in equivalent mass with the following equilibrium equation:

$$m_{eq}a_{3D} - m_{eq}a_{2D} = \Delta m_{\text{eq}}a_{3D} \tag{5.2}$$

$$\Delta m_{\text{eq}} = m_{eq}\frac{a_{3D}}{a_{2D}} - m_{eq} \tag{5.3}$$

Here a_{3D} is the maximum acceleration in the full-scale test (-12.1 g) and a_{2D} is the maximum acceleration in the 2D co-simulation analysis. The 2D-acceleration is filtered according to IMO-standards (20 Hz low-pass filter). m_{eq} is the equivalent mass of the 2D-section. This formula expresses the unbalance in force equilibrium that we achieve due to the virtual displacement. It is understood that this is an iterative procedure and 11 different simulations were performed using this approach. Then a plot was created showing the mass of the 2D-section and the achieved acceleration. The results were interpolated in order to create a much finer picture. This figure can be seen in figure 5.29.

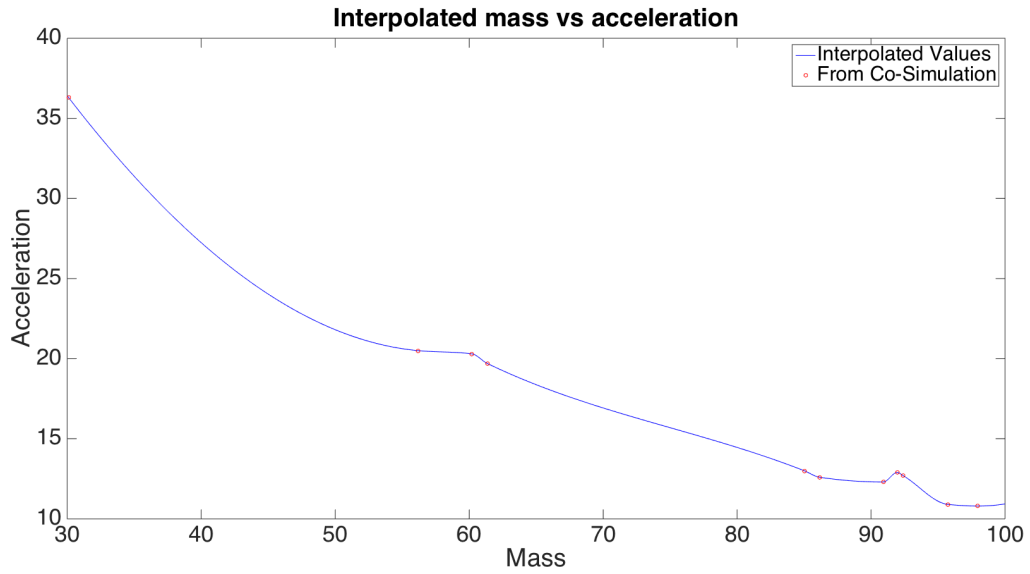

Figure 5.29: The interpolated values of the mass of 2D-section plotted against the maximum acceleration

From figure 5.29 can one observe that the total mass of the 2D-section would be 90.91 kg. This is the final mass that is used in the simulations - the final results can be viewed in section 5.6. One should note that this is an unphysical mass as the 2D-section will not float with this mass. The mass is the result of a virtual translation of the mass in full-scale in order to achieve force and moment equilibrium between the inertia force and pressure force.

Stiffness of Hull

A section in a full-scale lifeboat does not in itself have the sufficient stiffness to survive a 3 m free-fall drop. The majority of the stiffness comes from the ends of the lifeboat. It is therefore necessary to apply springs in order to achieve the right stiffness for the 2D-section. This procedure is given below:

1. Apply a load F_i^k in both x- and y-direction (i) at various nodes (k) in both the 3D model and the 2D model. These nodes must be located at the same location in space.
2. Perform a Static Analysis when all the loads are applied in the same step.
3. Find the displacement s_i^k at the node (k) in both x- and y-direction (i) due to the load (F_i^k).
4. Find the stiffness of the spring at the nodes using the formula $k_i^k = \frac{F_i^k}{s_i^k}$.
5. Subtract the acquired 2D-stiffness from the 3D-stiffness - this is done in order to ensure that the stiffness of the 2D-section is not accounted for twice.

The applied force is from the rigid CFD analysis. The maximum hydrodynamic force in x- and y-direction is 2800 N and 13 000 N respectively. Further, it is assumed that the springs on the keel would absorb 25 % of the force. For the top, it is assumed that it would absorb 0.5 % and the transition from the top to the keel would absorb 12.5 %. With reference to figure 5.27, spring number 1 is from the top to the keel and the springs are enumerated counter-clockwise. Spring number 1 to 2 is regarded as the top, 3 to 4 is regarded as the transition, while 5 to 7 is regarded as the keel. All the springs are connected with the mentioned points and the point on the keel.

In figure 5.27 we can see the applied springs in the 2D-section. We have now found the spring constants in both x- and y-direction for all the nodes on the figure. Springs are not applied in the x-direction at the node on the top right and at the bottom due to the boundary conditions on the model. In the model, two springs have been placed in the depth of the domain at each point in figure 5.27. Spring stiffness has, of course, been modified due to this. In addition, each point contains two springs - one in x-direction and one in y-direction. In table 5.10 can we

Table 5.10: Spring Stiffness Constants

Location	$k_x[\frac{N}{mm}]$	$k_y[\frac{N}{mm}]$
1	[-]	0.15
2	0.0195	0.1665
3	0.0375	0.06
4	1.662	1.275
5	0.0405	6.744
6	4.1325	1.5045
7	0.8835	2.8365

see the applied spring stiffness constants. Location number 1 is at the top and the numbers are enumerated counter-clockwise. All springs have their origin from the keel - hence there are no springs associated with the keel.

5.4.2 CFD-model

In order to perform a FSI-analysis coupled with Abaqus, we must perform a couple of changes. The mesh, domain, and time step remains the same as specified for the rigid case. The model is translated to 10 cm above the free surface in order to reduce computational time. This was

also done for the Abaqus model - since they must be conformal. In addition, the co-simulation modules are activated in order to allow communication between the two codes. The activated physical modules can be viewed in figure 5.30.

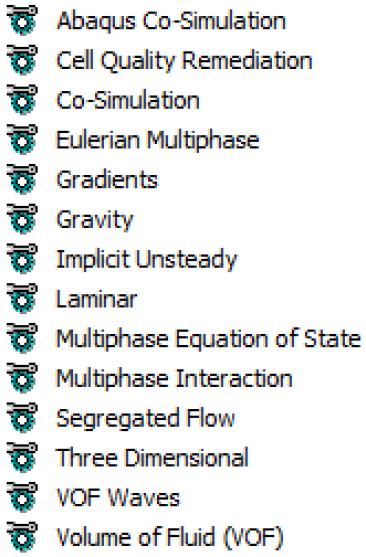

Figure 5.30: Activated physical modules during the co-simulation analysis

The *DFBI*-module is removed, since Abaqus will compute the nodal displacements. A morpher in the motion specification to the Overset Mesh region has been applied. This region contains the coupling surface named *WetSurface* on the hull. A change in boundary condition is demanded as specified in CD-Adapco (2014). The boundary named *Symmetry* in the overset mesh region is changed from a symmetry boundary condition to a slip-wall condition without a prism layer mesh. The change is related to the coupling between the overset mesh region and the background region. In table 5.11, we can see the boundary conditions of the morpher.

Table 5.11: Morpher Boundary Conditions

WetSurface	Abaqus Co-Simulation
Overset Mesh Interface	[-]
Symmetry	Floating

In the co-simulation setting, the following choices been applied. The coupling is implicit (since this is a strongly coupled problem) with a constant coupling time step equal to four times the time step used in the CFD-analysis. Star-CCM+ exports the pressure and wall shear stress acting on the hull (WetSurface), while Abaqus exports the nodal displacements. Abaqus leads the simulation. The mapper searches in the current coordinates in order to account for gravitational deformations. In addition, it checks the shell normals in order to export the pressure and shear force to the correct side of the shell. There are at minimum six exchanges per time step and two inner iterations per exchange. In addition will the morpher-solver morph during the inner iteration.

An under-relaxation factor has been applied. This factor relates to the nodal displacements

imported from Abaqus. The nodal displacement can be related to w in equation 4.5.

$$w_{i+1}^{n+1} = (1-\beta)w_i^{n+1} + \beta\tilde{w}_{i+1}^{n+1} \tag{5.4}$$

This equation is from Piro and Maki (2013). Where n is related to the time step, i the iteration within this time step and $\tilde{w}$ is unrelaxed displacement or predicted displacement. This approach was suggested by CD-Adapco (2014), but a low under-relaxation factor ($\beta < 0.5$) should be selected with care for problems that demand dynamic accuracy. The under-relaxation factor β is sat to 0.85 in the simulations in this thesis. As a consequence, it is necessary to perform more iterations and exchanges for each coupling step in order to achieve the full deformation. This will lead to a longer computational time, due to a higher number of iterations. The under-relaxation factor will not introduce the full deformation, therefore will this method under-predict the pressure loads, but it will stabilize the solution.

The coupling step is set equal to four times the coupling step in Star-CCM+. This means that Star-CCM+ exchanges information with Abaqus every forth time step. When we introduce a deformation to the structure, this is associated with a velocity and an acceleration. This leads to a pressure peak because we suddenly update the deformation values or move the structure in the fluid. It is beneficial to let the pressure solution rest and settle down due to this deformation, before introducing a new deformation. This was explored in Handeland (2014). The down side of this is that Abaqus only receives the pressure and wall shear that act at the time step for the coupling. Therefore, we can miss pressure peaks if they occur when we are between exchanges. The simulations have applied a coupling step that is four times the time step used in Star-CCM+. If Δt is $2.5{\cdot}10^{-4}$ the coupling time step would be 10^{-3}. It was found that this problem is much more sensitive than the studied wedge in Handeland (2014).

A physical consequence of this sudden change in deformation of the structure is that we introduce a sudden acceleration. The structure transfers this acceleration to the fluid. This is similar to the added mass problem in the seakeeping problem. The acceleration is however sudden and "discontinuous". This will change the forces and eigenfrequency of the problem, since the added mass suddenly changes. This is known as the artificial added mass effect in the literature, see Causin (2005) and Forster (2006) for more information. This will lead to further pressure oscillations due to the sudden increase in added mass.

A pressure ramping factor has been applied. This factor is important in the beginning of the simulation so that the hull is not influenced by the shock waves that can occur in the first time steps. Hence, it prevents numerical instabilities in the beginning. This factor works in such a way that it interpolates the exported pressure from zero at $t = 0$ to $P_{\text{coupling}} = P_{\text{star}}$ at $t =$ given.

The stopping criterion is also slightly modified - it now consists of three inner iterations criterions and one outer iteration criterion. The three inner stopping criterions are as following:

- When the Co-Simulation Residual is below 10^{-4}.
- When the number of inner iterations have exceeded 15.
- When the number of inner iterations have exceeded 200.

Where the latter applies when the two former are not achieved. The outer criterion is the stop-

ping time sat to 0.2 s.

5.5 Convergence of Time Step and Coupling Time Step

Due to the problems regarding mass, a vast number of simulations have been performed. This section contains a final study where the correct mass was found. It should be noted that the simulations performed in chapter 5.4.1 were performed with under-relaxation factor $\beta = 0.85$, time step $\Delta t = 2.5 \cdot 10^{-4}$ and coupling step equal to four times the time step.

A various number of combinations have been experimented with. It became apparent that the structure was more sensitive to the settings in the co-simulation than the wedge presented in Handeland (2014). It was quickly realized that the under-relaxation factor (β) had a huge impact and could cause failure of the co-simulation engine. The factor was established to be 0.85. In table 5.12 we can see the result of a short convergence study. The smaller time step somehow caused the simulation to crash. The reason for this is unknown, as there was no indication when considering pressure and deformations.

Table 5.12: Status for different co-simulations analysis

Time Step Δt	Coupling Time Step $x\Delta t$	Status
10^{-4}	3	Fail
10^{-4}	4	Fail
$2.5 \cdot 10^{-4}$	3	Ok
$2.5 \cdot 10^{-4}$	4	Ok
$5 \cdot 10^{-4}$	4	Ok

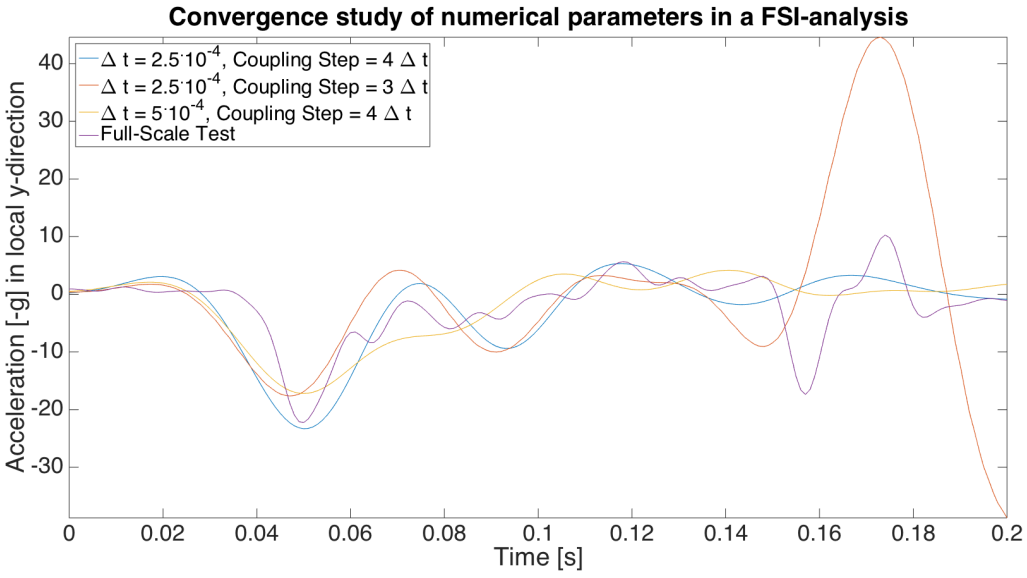

Figure 5.31: Acceleration time history from the convergence study of numerical parameters in a co-simulation analysis compared against the full-scale test results

In figure 5.31 can we see the acceleration from the convergence study compared to the full-scale test results. We can quickly see that the simulation with a time step equal to $5 \cdot 10^{-4}$ yields the

worst match and is therefore discarded. One should expect that the simulation with the lowest coupling step would yield a more correct result; however, this is not the case here. This is due to the spike in acceleration observed in the end of the simulation. The simulation with under-relaxation factor $\beta = 0.85$, time step $\Delta t = 2.5 \cdot 10^{-4}$ and coupling step is equal to four times the time step is chosen. As previously mentioned, the simulations were performed in chapter 5.4.1 created the basis for the applied additional mass. These simulations were performed using the obtained settings in this section. This could be the reason that the chosen set-up had the best fit with the test results.

5.6 Results

The co-simulation is performed with the setting and values as given above. Due complications regarding the additional mass, a vast number of models were simulated and the presented result is from the final simulation. In table 5.13 can we see the applied values and properties. The other settings are as described above.

Table 5.13: Properties and values

Base size	0.5 [m]
Domain	(0.0, -7.5, 0.0), (-7.0, 8.5, 0.05)
Time step	$2.5 \cdot 10^{-4}$
Initial Velocity	7.452 $[\frac{m}{s}]$
Mass	90.91 [kg]
Constant Coupling Time Step	10^{-3}
Under-relaxation factor β	0.85
Number of inner iterations per exchange	2
Minimum number of exchanges per time step	6
Star-CCM+ Exports	Static Pressure and Wall Shear Stress
Abaqus Exports	Nodal Displacements
End time pressure ramping	$5\Delta t$

In figure 5.32 we can observe the acceleration from the co-simulation. The numerical results are filtered with a fourth-order digital low-pass Butterworth filter with a cutoff frequency equal to 50 Hz. The test results are extracted from figure 5.4 and represent the unfiltered results. It should be noted that the applied additional mass found in chapter 5.4.1 was found using the filtered test results and the numerical results was subject to a 20 Hz low-pass filter.

It is observed that the numerical FSI results follow the full-scale test results closely. One should note that the mass has been tuned in order to achieve the same maximum acceleration. Even though when this is the case can we observe that they follow each other closely after the point of maximum acceleration. This implies that the numerical model is able to recreate the slamming event in a satisfactory manner. This can also indicate that the stiffness and damping used in the model is correct, as they experience approximately the same oscillation period. This can be further explored in appendix E. In appendix F we can see the comparison between the acceleration in the FSI-analysis and the rigid CFD-analysis.

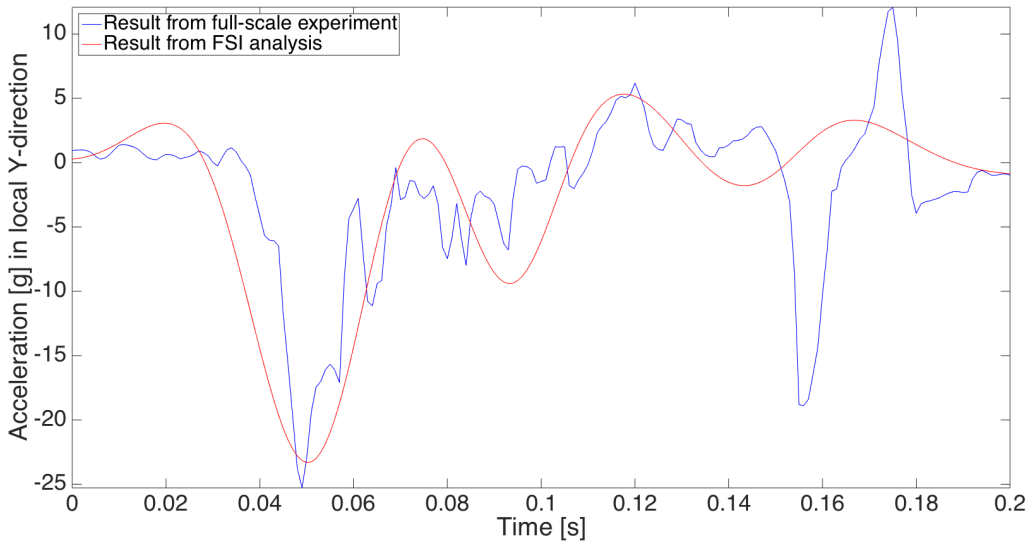

Figure 5.32: Comparison of the acceleration in local Y-direction between the full-scale test results and the final numerical co-simulation results

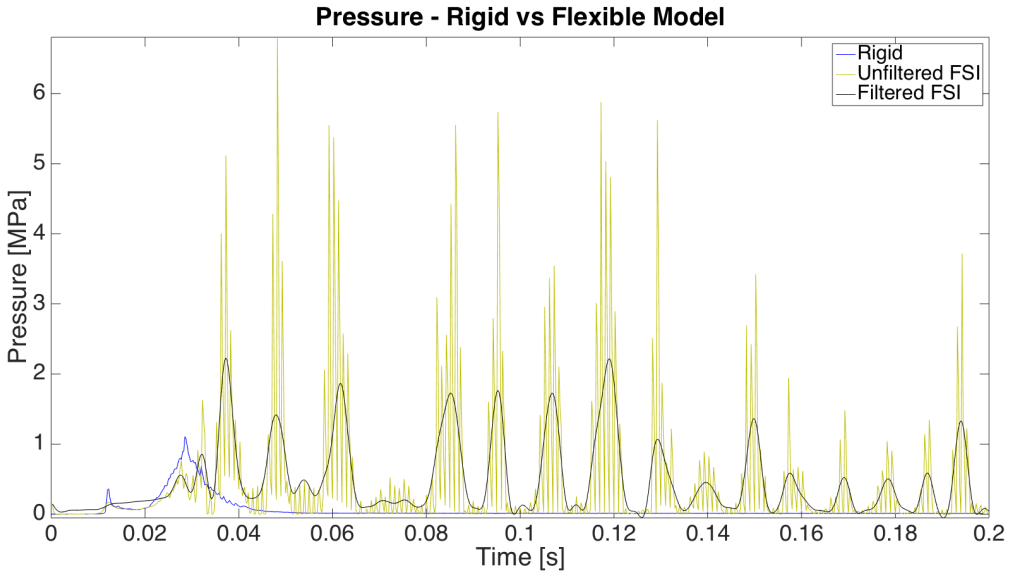

Figure 5.33: Comparison between the rigid pressure and the pressure obtained from the co-simulation analysis

We can observe that the pressure in figure 5.33 is associated with oscillations. First the pressure is associated with the slamming pressure and after the pressure oscillations start. This is in accordance with the theory presented in chapter 4.3. In figure 5.34 can we see the power spectrum of the pressure solution. It is interesting to note that the oscillations are concentrated around specific peaks and not all over the domain.

When we look at the right side of figure 5.34 we can see that the peaks are associated with the coupling frequency. We can assume that the peaks close to the coupling frequency are due to transients from the coupling. Let us now ignore the peaks above 500 [Hz]. On the left side in the figure we can observe some of the eigenfrequencies. We can understand from comparison

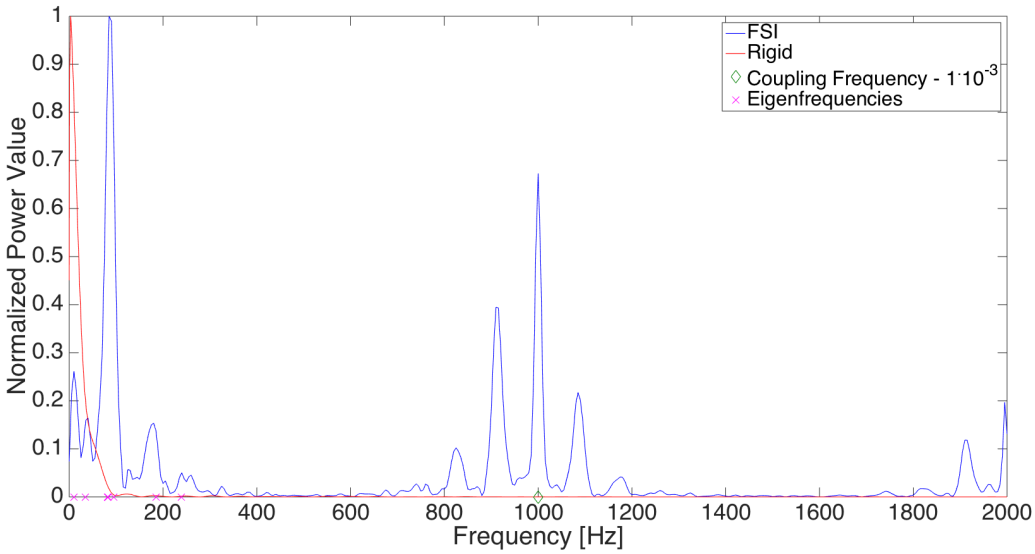

Figure 5.34: Power Spectrum of the maximum pressure from the rigid and the co-simulation analysis

with the spectrum of the rigid structure that the some of the eigenmodes are excited during the impact. The deformation from the activated eigenmodes will greatly contribute to the pressure oscillations and vibrations on the structure. It is believed that the simulation has recreated a hydroelastic event.

We can based upon the presented results in this section draw the conclusion that the developed co-simulation model is able to recreate the physics behind a full-scale 3 m free-fall drop test. It is uncertain if the benchmark presented in the chapter is subjected to hydroelasticity - but it is very likely as the deadrise angle is small and the impact velocity is fairly large. In addition the sandwich composites shells are not very stiff. This can further be validated through the oscillations showed in figure 5.34. The results and conclusion presented in Handeland (2014) stated that the method was able to recreate a hydroelastic event regarding wedge impact using the same method. Based on the results in figure 5.32 one can conclude that the numerical model is able to recreate the full-scale 3 m free-fall drop test in a satisfactory manner and the hydroelastic phenomenon associated with this test. It should be emphasized that the mass of the section is found using the resulting maximum acceleration, but even when this is the case, the results are very similar and they express the same oscillation period. It can therefore be concluded that the results show that the method is able to capture the physics and it can be trusted. Since the model yields results in accordance with the full-scale test, the next step is to move forward with a parametric study in order to explore when it is important to account for fluid-structure interaction.

Chapter 6

Parametric Study

6.1 Motivation

The purpose of this thesis is to investigate when it is important to account for hydroelasticity when performing numerical simulations on lifeboats. In chapter 5 it was demonstrated that the applied method is able to recreate a hydroelastic event and that the model is capable of recreating a full-scale test scaled down from 3D to a 2D-section when considering the deceleration of the hull. This is important, as the deceleration of the hull can have an important effect on the strains in the structure, (Arai M., 1998).

In order to determine when hydroelasticity is important, a parametric study will be suitable. To perform a parametric study, a large number of simulations will be performed using the model and setting from the previous chapter. The impact velocity, deadrise angle of the hull, and the modulus of elasticity (E and G) will be varied. The maximum strains from the co-simulations will be compared with strain from a quasi-static model. The only difference from the model presented in chapter 5.6 is the geometric change due to the deadrise angle, the modulus of elasticity, the shear modulus of the material, and the impact velocity.

The topic fluid-structure interaction and hydroelasticity has been a popular topic for many years. There have been many papers published on the subject, but these papers mainly consider simple geometries, such as simple wedges or wedge shaped plate field. In addition, these are structures mainly constructed of metals. Structures built with construction grade metals are usually associated with a high stiffness and from equation 4.2 a high stiffness is associated with a lower degree of hydroelasticity. Hence, large parts of the available work are based on simple high rigidity structures. Some work is also done on complex (hull sections, complete structures) high rigidity structures e.g. in Bloxom (2012). Very little is done on simple low rigidity structures such as composite plate wedges which was studied in Panciroli (2005). Even less is performed on complex low rigidity structures. These complex structures can, for example, be the hull of a glass-fiber reinforced composite lifeboat. Some work is done on decision factors for when it is important to account for hydroelasticity, but these are mainly related to simple high rigidity structures, (Faltinsen, 1999b), (Panciroli, 2005) and (Bereznitski, 2002). There exist very few articles that the obtained results can be related to. However, support will be retrieved from

previously presented results in Faltinsen (1999b), Faltinsen (2000) and Panciroli (2005).

6.2 Evaluation

6.2.1 Assumptions

In this chapter it has been assumed that the hull responds quasi-steady, (Faltinsen, 1999b). This implies that the response of the hull follows the dynamic load (pressure) which is proportional to the impact velocity squared (V^2). If the hull did not respond quasi-steady, it would have to be assumed that the response of the hull is dominated by hydroelasticity. When hydroelasticity dominates, it is not possible to first obtain the hydrodynamic loads by assuming a rigid body and then use these loads to predict the response of the hull, (Faltinsen, 2000). The structural solution now requires a design pressure from the hydrodynamic solution in order to find the response. The problem arises when the solution is highly hydroelastic, as design pressure cannot be obtained due to the pressure oscillations. The only way is to define an equivalent pressure which yields the same maximum strain. This is however a bad approach as it is a manufactured pressure, (Faltinsen, 2000). One quickly realizes that the assumption is reasonable.

6.2.2 Evaluation Parameter

In order to be able to determine when hydroelasticity is important, we need to choose a parameter that is consistent and easy to obtain for all possible configurations. In Faltinsen (1999b) and various other articles, we can observe that the maximum strain has been chosen as a parameter. Based on previous articles, it has been understood that the strain is a good parameter to evaluate, as it is able to describe both the stresses in the structure and the deformation. The nominal strain at the red point shown in figure 6.1 will be extracted. This region was chosen due to the similarities with the plate field which was studied in Faltinsen (1999b). The ends are supported by buoyancy foam and can be considered as support for the plate/beam. The reason for choosing this point and not a point at the middle was due to the presence of a spring. It appeared that the spring interacted with the strains in the shell at this point. It is preferable to deal with the nominal strain or Green strain because it incorporates the large rigid body motions into the strain evaluation and is therefore able to deal with large deformation theory.

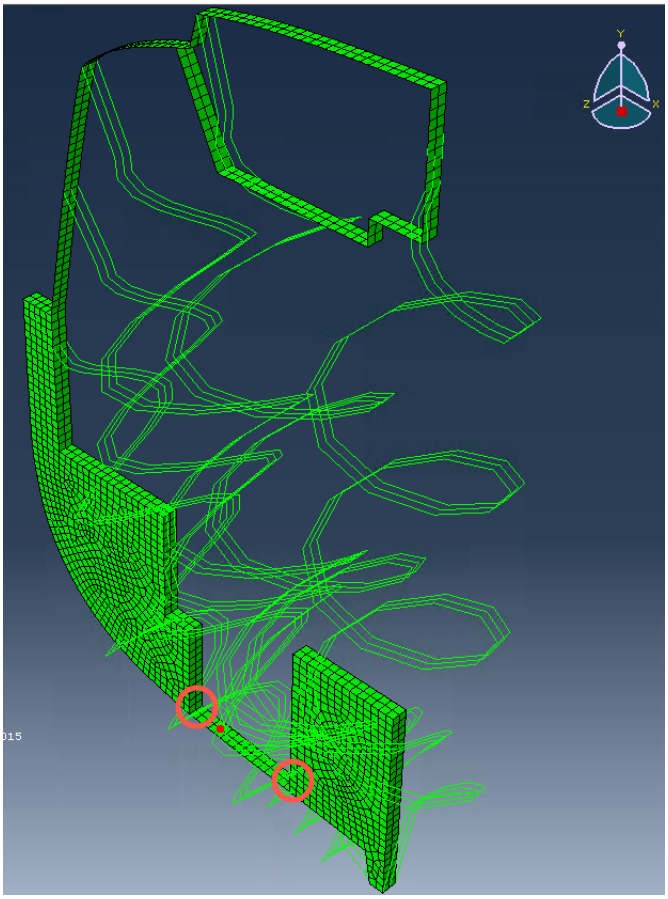

Figure 6.1: The red point is the point where the stain will be evaluated in the FEM-model. Note that the springs can be viewed in the figure

6.2.3 Dimensionless Parameters

In order to compare the results from the co-simulations with the quasi-static analysis, it is more convenient to compare the results when they are dimensionless. In this way, the different combinations can be easier incorporated.

We can observe from Faltinsen (2005) that if the structure responds quasi-steady is the maximum strain assumed to be proportional to V^2. This is explained by the fact that the impact pressure is proportional to V^2. The strain is now made dimensionless as $\frac{\varepsilon D \tan\alpha}{Z_a V^2 \rho L^2}$. Where ε is the maximum strain in the point, D is the bending stiffness (EI), α is the deadrise angle of the hull, Z_a is the height from the keel to the point where the strain is evaluated, V is the impact velocity, ρ is the density of water ($1000\frac{kg}{m^3}$) and L is the beam length.

If hydroelasticity is regarded as significant we can observe from Faltinsen (1999b) that the strain is assumed to be proportional to V. The strain is now made dimensionless as $\frac{\varepsilon\sqrt{D/\rho L}}{Z_a V}$.

It is also possible to non-dimensionalize as in Panciroli (2005). The strain is made dimensionless as $\frac{E\varepsilon\tan\alpha}{V^2\sqrt{M}}S$. Here α is the deadrise angle, M is the total mass of the structure, V is the impact velocity, ε is the nominal strain at the point, E is the modulus of elasticity of the layer on the top of the shell, S is the sectional modulus.

6.2.4 Quasi-Static Approach

As previously mentioned, the region is chosen based upon the similarities with the plate field in Faltinsen (1999b). We can consider the shell as a plate in a plate field with longitudinal stiffeners (going in Z-direction). The stiffeners are in the area where the shell connects with the buoyancy foam. For convenience, they are marked with red circles in figure 6.1. The region on the hull where the plate field is located is marked as L4 in figure 6.2. The stiffeners are the longitudinal area of this plate field. As the plate field is longer than it is wide and because 2D theory is assumed, strip theory can be applied. This means that the plate is reduced so that we can apply Euler-Bernoulli beam theory to a strip of the plate.

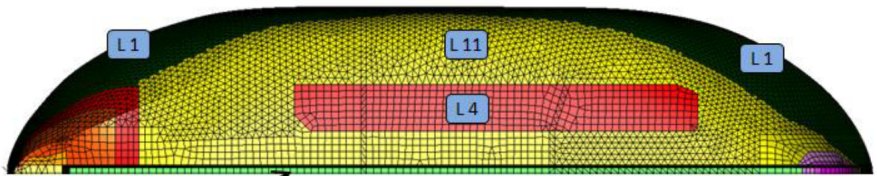

Figure 6.2: L4 is the plate field where the strain is evaluated, (Fedem, 2011)

With this approach we can apply a simple analytical formula in order to assess the hydroelastic quasi-static strain. We know from Gere and Timoshenko (1997) that for a beam the following relationship exists:

$$\varepsilon_x = -z\frac{\partial^2 w}{\partial x^2} \tag{6.1}$$

Where z is the height from the neutral axis to the point of evaluation and w is the displacement. Based on the co-simulation results in chapter 5.6 it is assumed that the beam has the boundary conditions expressed in figure 6.3. Where the left side in figure 6.3 is to the right in figure 6.1. From Gere and Timoshenko (1997) we can see that the displacement w for the given beam is:

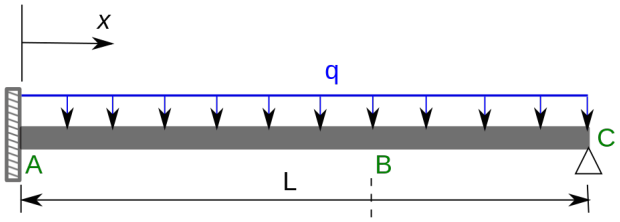

Figure 6.3: Equivalent beam subject to quasi-static strain calculation, (Gere and Timoshenko, 1997)

$$w(x) = \frac{qx^2}{48D}(3L^2 - 5Lx + 2x^2) \tag{6.2}$$

Where q is an evenly distributed pressure load and x is the position on the beam where the strain is evaluated. Hence can the strain in the beam be expressed as:

$$\varepsilon_x(x,z) = -z\frac{q}{8D}(L^2 - 5Lx + 4x^2) \tag{6.3}$$

In order to determine the quasi-static response of the plate a rigid CFD-analysis has been performed for all the relevant cases (all deadrise angles and velocities). When the average pressure on the hull was at a maximum the simulation terminated. The pressure was then space-averaged over the indicated plate area - between the two circles in figure 6.1. The strain is evaluated in the same point as the FSI-analysis. The values are made dimensionless, as defined earlier. It appears that the nondimentional strains converge to the same value. This can be observed in figure 6.4. Mean is taken of the obtained dimensionless values. This is mainly for the reader's convenience

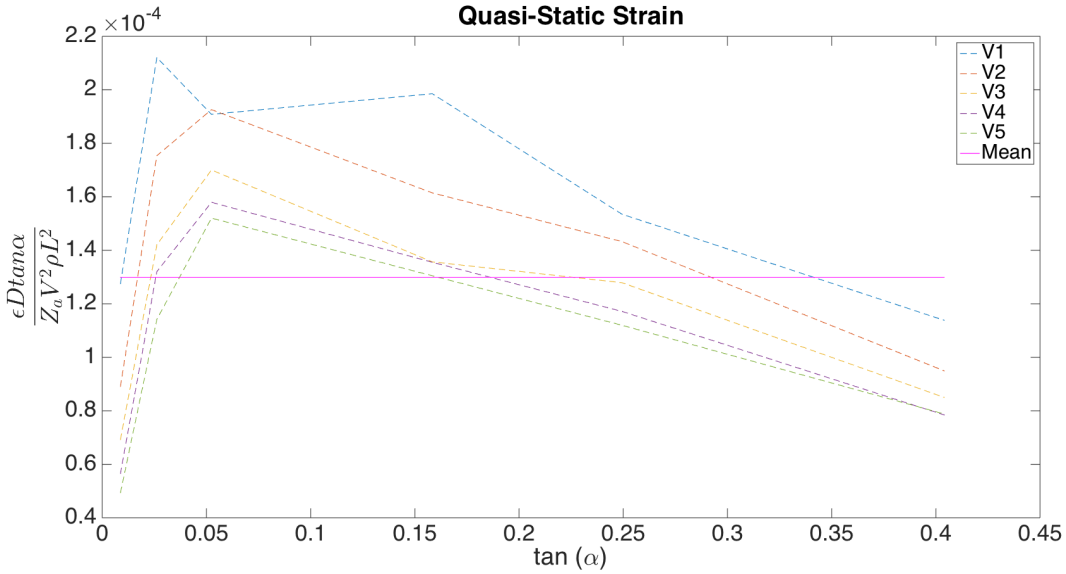

Figure 6.4: Quasi-Static nondimentional strains with different velocities and deadrise angles compared with the mean of the values

6.2.5 Rigid CFD Analysis

In order to find the quasi-static pressure and load duration, a series of rigid CFD analysis was performed. All the velocities and deadrise angles were represented - 30 simulations in total. The pressure applied to find the quasi-static strain can be viewed in appendix B while the load durations can be found in appendix C.

6.2.6 Sandwich Beam Theory

The plate is a sandwich composite beam - consisting of a top and bottom material and a core material. This can also be denoted as two faces and a core material. The layout can be viewed in figure 6.5. As defined in Vinson (1999) can we find the bending stiffness D with the following formula:

$$D = \frac{AC - B^2}{A} \tag{6.4}$$

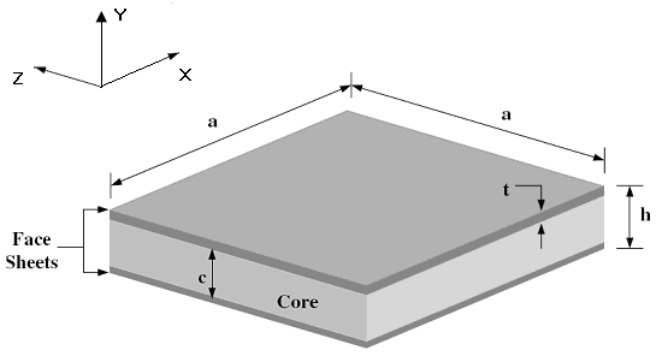

Figure 6.5: Layout of a sandwich beam, (Vinson, 1999)

Where

$$A = \Sigma_{i=1}^{k} \frac{E_i}{1-\nu_i^2}(y_i - y_{i-1}) \tag{6.5}$$

$$B = \Sigma_{i=1}^{k} \frac{E_i}{1-\nu_i^2}\frac{y_i^2 - y_{i-1}^2}{2} \tag{6.6}$$

$$C = \Sigma_{i=1}^{k} \frac{E_i}{1-\nu_i^2}\frac{y_i^3 - y_{i-1}^3}{3} \tag{6.7}$$

Where E_i is the modulus of elasticity of the material, ν is the Poisson ratio and y_i and y_{i-1} is the end and start height of the layer. k is the total number of layers in the sandwich. In this case, the shell consists of three layers - the top and bottom layer consists of 4 mm of spray laminate and the core is 6 mm of Uni-Directional Epoxy-glass. This constant is relevant to the structural behavior of the beam. This can be seen in equation 4.5. In addition, we need to consider that the beam does not have a unit width. This is accounted for by multiplying the bending stiffness D with the extruding depth of the hull (50 mm).

6.3 Importance of Hydroelasticity

In order to decide which cases that should be simulated, we need to utilize a decision factor. In chapter 4 it was observed that Faltinsen (1999b) described a parameter that was able to describe when hydroelastic effects became important. The basis for the formula is the ratio between the wetting time or the load period and the first dry natural period of the structure. The formulas are defined in equation 4.1 and 4.2. The case studied here is different since it contains a more complex structure and it is constructed from composite materials. It is interesting to see if R_F is able to predict hydroelasticity in the indicated plate in figure 6.1. R_F is of interest as we do not need to perform any analysis in order to decide if hydroelasticity is important. Where in equation 4.4, defined in Bereznitski (2001), it is necessary to perform some preliminary analysis. First will R_F be used as a decision factor and later will the results be compared when applying R_B. The more general equation R_B defined in Bereznitski (2001) may yield better results for more complex structures.

It has been chosen to evaluate five different impact velocities, five different materials and six different deadrise angles. The definition of the deadrise angle can be seen in figure 6.6 (shown here a deadrise angle equal to 6 degrees). We can observe that the length L and the height Z_a is

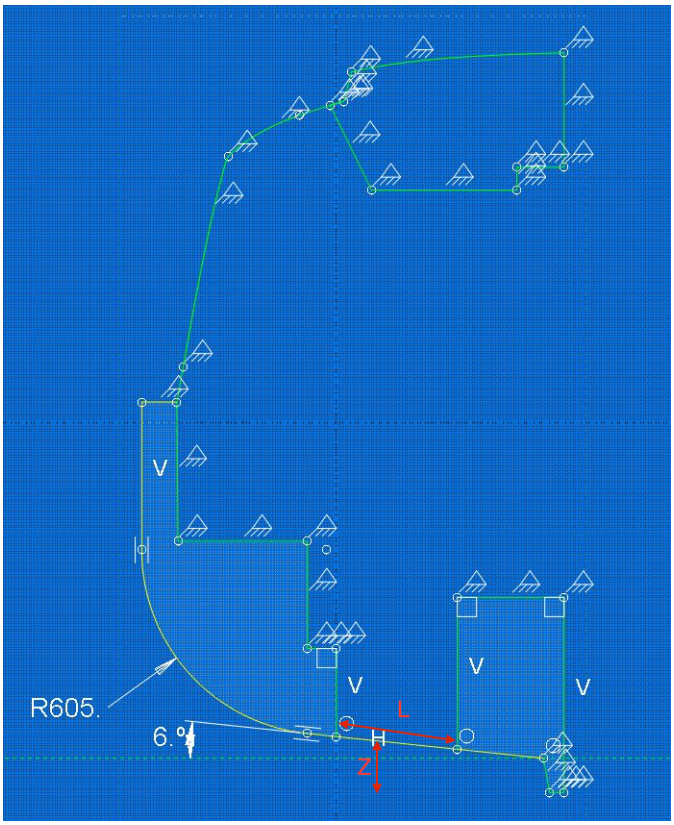

Figure 6.6: Sketch of 2D-section when the deadrise angle can be varied

also defined in the figure. There exists a significant difference when we compare the sketches in figure 5.6 and 6.6. In order to be able to change the deadrise angle, it was necessary to make these changes to the model. As a consequence, L and Z_a will change when the deadrise angle changes. The reason for altering these three parameters is based on Faltinsen (1999b) and Bereznitski (2002). Here it was shown that lower deadrise angles and higher impact velocities lead to a higher influence from hydroelasticity. While Bereznitski (2002) showed that a reduction of structural stiffness will increase the influence from hydroelasticity.

The main change in the model is the deadrise angle; this is described above. This change is done in Abaqus and then the model is exported to Star-CCM+. The change in velocity is done in the prescribed velocity field. The last change made to the material, altering Young's modulus (E) and the shear modulus (G). The additional mass and spring constants are kept constant. It is assumed that the change in geometry does not significantly alter the total mass of the hull. This assumption is reasonable as most of the mass comes from the additional mass represented by the sandbags. Keeping the stiffness of the springs constant is not a very reasonable assumption, since the geometrical stiffness of the structure will change according to the deadrise angles. It is time consuming to find the spring constants in 2D, and with the fact that it is not possible to change the 3D-model, this assumption is necessary. The total running time is increased to 0.3 seconds in order to capture the dynamic effect for the steepest deadrise angles and lowest

impact velocities. The hull is still subjected to gravity load and is dropped 10 cm above the free water surface. The other settings are kept equal, as earlier.

The span in velocities and material properties consist of five different values. Where two are above the values used in the flexible model in the verification study and two are below. Both sides of the default value is 25 % and 50 % above or below. This is done in order to use realistic values. The expressed bending stiffness D is calculated based on equation 6.4. $V3$ and $D3$ are the default values from the verification study.

Table 6.1: Different velocities used in the parametric study

Name	Velocity [$\frac{m}{s}$]
V1	3.726
V2	5.589
V3	7.452
V4	9.315
V5	11.178

Table 6.2: Different resulting bending stiffnesses from different material properties used in the parametric study

Name	Bending Stiffness - D [Nm^2]
D1	59.96
D2	89.95
D3	119.93
D4	149.91
D5	179.90
D60	7195.81

Table 6.3: Different deadrise angles used in the parametric study

Deadrise angle [deg]
0.5
1.5
3
9
14
22

In tables 6.1, 6.2 and 6.3, we can see the applied values. For comparison is D in Faltinsen (1999b) equal to 61110 [Nm^2] which is 8.5 times stiffer than D60. For simplicity, it will be refer to the names of the different values instead of the values.

In figure 6.7 we can see the result when applying the values to the inequity in equation 4.1. Within each deadrise angle (marked in green) every combination of the five impact velocities and stiffnesses is applied (velocity is horizontal and the different material is vertical). The notation **FSI** suggests that according to equation 4.1 is it important to account for hydroelasticity, while **Ikke FSI** suggests the contrary. In figure 6.8, it is possible to observe the values when

		V5	V4	V3	V2	V1
D5	0,5	FSI	FSI	FSI	FSI	FSI
D4		FSI	FSI	FSI	FSI	FSI
D3		FSI	FSI	FSI	FSI	FSI
D2		FSI	FSI	FSI	FSI	FSI
D1		FSI	FSI	FSI	FSI	FSI
D5	1,5	FSI	FSI	FSI	FSI	FSI
D4		FSI	FSI	FSI	FSI	FSI
D3		FSI	FSI	FSI	FSI	FSI
D2		FSI	FSI	FSI	FSI	FSI
D1		FSI	FSI	FSI	FSI	FSI
D5	3	FSI	FSI	FSI	FSI	FSI
D4		FSI	FSI	FSI	FSI	FSI
D3		FSI	FSI	FSI	FSI	FSI
D2		FSI	FSI	FSI	FSI	FSI
D1		FSI	FSI	FSI	FSI	FSI

	V5	V4	V3	V2	V1
9	FSI	FSI	FSI	FSI	Ikke FSI
	FSI	FSI	FSI	FSI	Ikke FSI
	FSI	FSI	FSI	FSI	Ikke FSI
	FSI	FSI	FSI	FSI	FSI
	FSI	FSI	FSI	FSI	FSI
14	FSI	FSI	Ikke FSI	Ikke FSI	Ikke FSI
	FSI	FSI	FSI	Ikke FSI	Ikke FSI
	FSI	FSI	FSI	Ikke FSI	Ikke FSI
	FSI	FSI	FSI	FSI	Ikke FSI
	FSI	FSI	FSI	FSI	Ikke FSI
22	Ikke FSI	Ikke FSI	Ikke FSI	Ikke FSI	Ikke FSI
	Ikke FSI	Ikke FSI	Ikke FSI	Ikke FSI	Ikke FSI
	FSI	Ikke FSI	Ikke FSI	Ikke FSI	Ikke FSI
	FSI	FSI	Ikke FSI	Ikke FSI	Ikke FSI
	FSI	FSI	FSI	Ikke FSI	Ikke FSI

Figure 6.7: Results from a study of the importance of hydroelasticity using inequity 4.1. The different deadrise angles are marked green while the different velocities are marked in yellow and placed horizontal, and the different stiffnesses are placed vertical in yellow

0,5	11,178	9,315	7,452	5,589	3,726
138,9	0,00117	0,00141	0,00176	0,00234	0,00352
115,8	0,00107	0,00128	0,00160	0,00214	0,00321
92,6	0,00096	0,00115	0,00144	0,00191	0,00287
69,5	0,00083	0,00099	0,00124	0,00166	0,00249
46,3	0,00068	0,00081	0,00102	0,00135	0,00203

9	11,178	9,315	7,452	5,589	3,726
138,9	0,02088	0,02506	0,03132	0,04176	0,06264
115,8	0,01906	0,02287	0,02859	0,03812	0,05719
92,6	0,01705	0,02046	0,02557	0,03410	0,05115
69,5	0,01477	0,01772	0,02215	0,02953	0,04430
46,3	0,01206	0,01447	0,01808	0,02411	0,03617

1,5	11,178	9,315	7,452	5,589	3,726
138,9	0,00352	0,00422	0,00527	0,00703	0,01055
115,8	0,00321	0,00385	0,00481	0,00642	0,00963
92,6	0,00287	0,00344	0,00431	0,00574	0,00861
69,5	0,00249	0,00298	0,00373	0,00497	0,00746
46,3	0,00203	0,00244	0,00304	0,00406	0,00609

14	11,178	9,315	7,452	5,589	3,726
138,9	0,03201	0,03841	0,04801	0,06401	0,09602
115,8	0,02922	0,03506	0,04383	0,05844	0,08765
92,6	0,02613	0,03136	0,03920	0,05227	0,07840
69,5	0,02263	0,02716	0,03395	0,04526	0,06790
46,3	0,01848	0,02218	0,02772	0,03696	0,05544

3	11,178	9,315	7,452	5,589	3,726
138,9	0,00702	0,00843	0,01054	0,01405	0,02107
115,8	0,00641	0,00770	0,00962	0,01283	0,01924
92,6	0,00574	0,00688	0,00860	0,01147	0,01721
69,5	0,00497	0,00596	0,00745	0,00993	0,01490
46,3	0,00406	0,00487	0,00608	0,00811	0,01217

22	11,178	9,315	7,452	5,589	3,726
138,9	0,04845	0,05814	0,07267	0,09690	0,14534
115,8	0,04423	0,05307	0,06634	0,08845	0,13268
92,6	0,03956	0,04747	0,05934	0,07912	0,11867
69,5	0,03426	0,04111	0,05139	0,06852	0,10277
46,3	0,02797	0,03357	0,04196	0,05594	0,08391

Figure 6.8: Results from study of the importance of hydroelasticity displaying R_F as defined in equation 4.2. The different deadrise angles are marked green while the different velocities are marked in yellow and placed horizontal, and the different stiffnesses are vertical in yellow

applying equation 4.2, obtaining the ratio R_F. We can understand from figure 4.5 that all the simulations either respond fully elastic or they are in the transition area. From figure 6.8 we can therefore observe that the problem is hydroelastic in nature and a co-simulation analysis is necessary to find the proper load and response. R_F for D60 can be found in appendix D.

It is also possible to find the importance of hydroelasticity from the formula given by Panciroli (2005) which is defined in equation 4.3. In Panciroli (2005), the writer suggests that the effect from hydroelasticity is negligible when $R_P \geq 200$. If the values specified in tables 6.1, 6.2, and 6.3 are applied, we achieve a maximum value of $R_P = 6.7$. If the result from Panciroli (2005) should be followed, one needs to increase the material parameters with a factor of 10^7 yielding $R_P = 197$. This is an extreme and unphysical increase as it would result in that the buoyancy foam is 240 times stiffer (in terms of Young's modulus) then structural steel. This makes this parameter unsuitable for this study - however the results will be presented for the interest of the reader.

6.4 Choice of Analysis Series

Due to the vast number of possible simulation cases, is it important to choose which cases that are going to be simulated. In this chapter, three series will be simulated where the stiffness is kept constant. This means that each series contains every impact velocity and deadrise angle. One series, therefore, contains 30 simulations. The series have been chosen according to figure 6.7 and 6.8. In this way, some simulations will be below the limit $R_F < 0.25$ and some in the transition area. This can be viewed in figure 6.8. In addition a series will be performed with D60.

After some trial simulations D3, D4, and D5 have been chosen as the stiffnesses for three of four series. This is based upon stability in the test simulations. It was clear that cases with a lower stiffness were subjected to more instabilities, this is in accordance with Arai M. (1998). This is can be a result of the change in eigenfrequency when the material properties, E and G, are modified. These instabilities can also be the result of bifurcation points in non-linear structural mechanics, (Moan, 2003). This is mainly related to the dynamic solution of the problem. The instabilities in the simulations are likely the reason for the failure of many simulations. This means that the co-simulation engine quits before the stopping time was reached. This was mainly due to convergence issues within the Abaqus solution engine.This will be further investigated in chapter 6.7. This displays the sensitive nature of an FSI-analysis, as small changes can affect the response greatly. Some simulations failed due to problems with the CFD solver. This was mainly related to negative volume in some cells or problems with the overset mesh. If this is the case, some minor changes were made and the simulation is restarted.

The failure of the co-simulation engine makes it difficult to know if the maximum strain has been achieved. It was mentioned in chapter 6.2.1 that it has been assumed that the strain follows the dynamic loading. This can be used in order to find out if the obtained strain is the representable maximum. If the strain follows the dynamic loads, one can examine the time series of the acceleration and the surface averaged pressure on the hull. The reason for using the acceleration is because it is related to the inertia forces on the hull. Arai M. (1998) found out that the deceleration had a significant effect on the strain time history. This implies that a study of the acceleration is important for the strain. The surface-averaged pressure is more representable than the maximum pressure, as the maximum pressure only shows the maximum pressure in a single cell along the hull, while the surface averaged pressure is the pressure surface averaged over the hull. This makes it more representable and easier to display the change in the hydrodynamic load. According to this assumption, if the point of maximum dynamical load (acceleration and pressure) has passed, one can expect that the maximum strain has occurred (given that the plate is given some time to respond). Unfortunately, one cannot know for sure if this point has passed and we therefore need to rely on experience. Another good option is to compare with similar cases (same deadrise angle and stiffness), e.g. if V3 has quit early and V2 and V4 have finished. We can then use the time series from V2 and V4 to some extent and compare with the results from V3. From this is it possible to interpolate and see if it is likely that the point of maximum strain has occurred in V3.

In figures 6.9 and 6.10 the result from a comparison between the surface averaged pressure

along the hull, the acceleration in local y-direction and the nominal strain in x-direction (at the same point as showed in figure 6.1) can be seen. Figure 6.10 shows the filtered results. A 50 Hz low-pass filter has been applied to the acceleration and strain, while a 500 Hz low-pass filter has been applied to the pressure. The maximum strain occurs shortly after the maximum acceleration - about 28 ms. While the maximum strain occurs at the same time as the surface averaged pressures reaches its maximum. This shows that the assumption, that the response is quasi-steady, is reasonable.

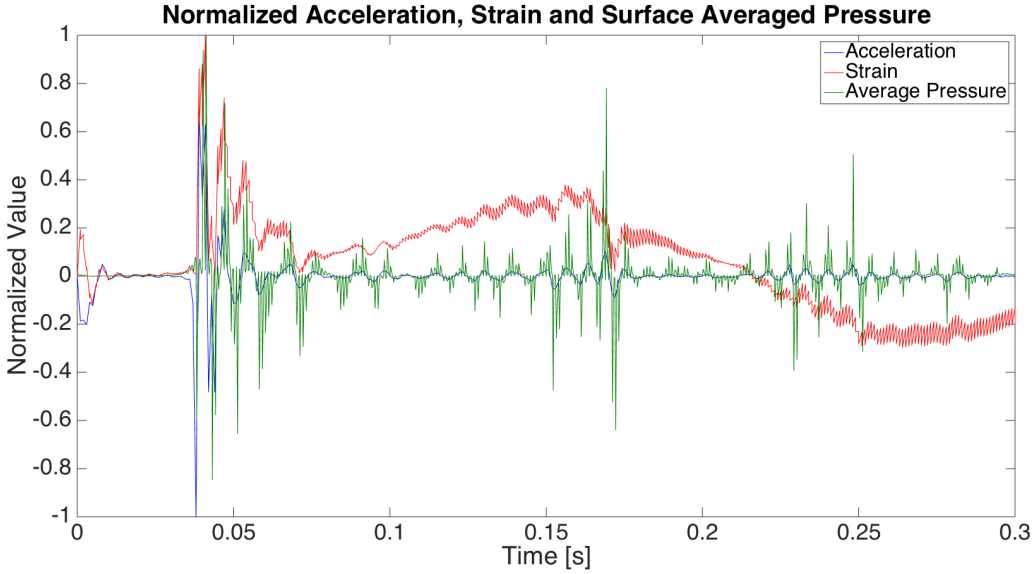

Figure 6.9: Normalized accelerations and stain evaluated in the the same node compared again the surface-averaged pressure along the hull

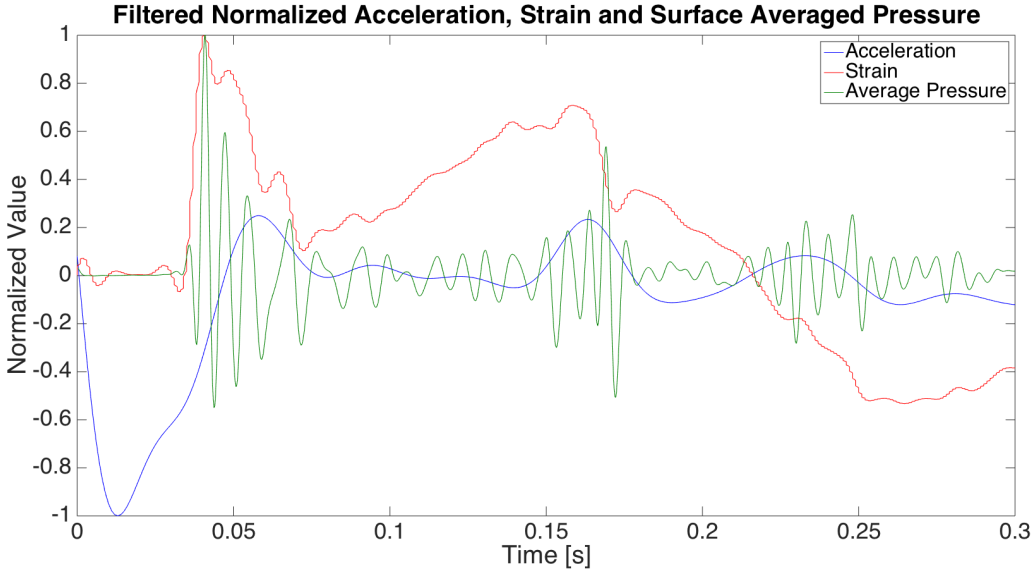

Figure 6.10: Filtered normalized accelerations and stain evaluated in the the same node compared again the surface-averaged pressure along the hull

As many simulations have been performed, the described method is the preferable approach to verify if the maximum strain is obtained, because this method is more convenient than to tweak

variables which can alter the presented results. In the case of doubt, several parameters can be changed in order to stabilize the solution. The following can been changed:

- Initial Time Step in Abaqus
- Under-relaxation factor
- Coupling Step

The maximum strain was retrieved for all simulations under the assumption that the strain follows the dynamical loading with these methods.

6.5 Results from Different Simulation Series

In the presented results from the difference series, the quasi-static values are not incorporated as the focus lies on the results. The quasi-static strain will be presented when comparing all the simulations.

6.5.1 Results from D3-series

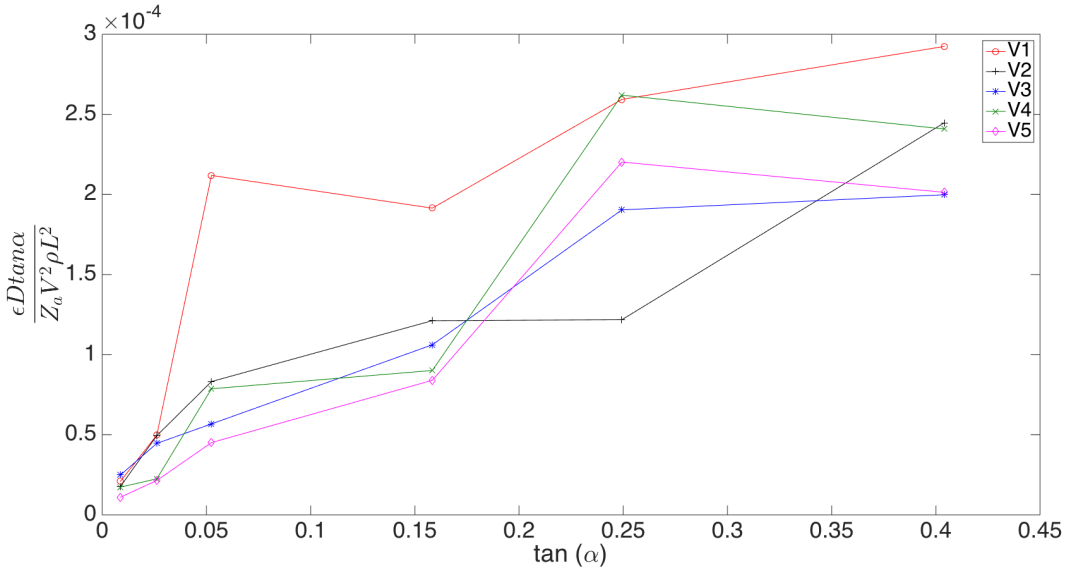

Figure 6.11: Results from the FSI-simulation series with stiffness of the plate equal to D3 with different impact velocities and deadrise angles compared again the quasi-static hydroelastic beam theory when assuming that the plate responds quasi-steady

In figures 6.11, 6.12, 6.13 and 6.14 can we see the results from 30 FSI-analysis when evaluating the strain in the plate and non-dimensionalized them as described above. The results will be commented in section 6.8.

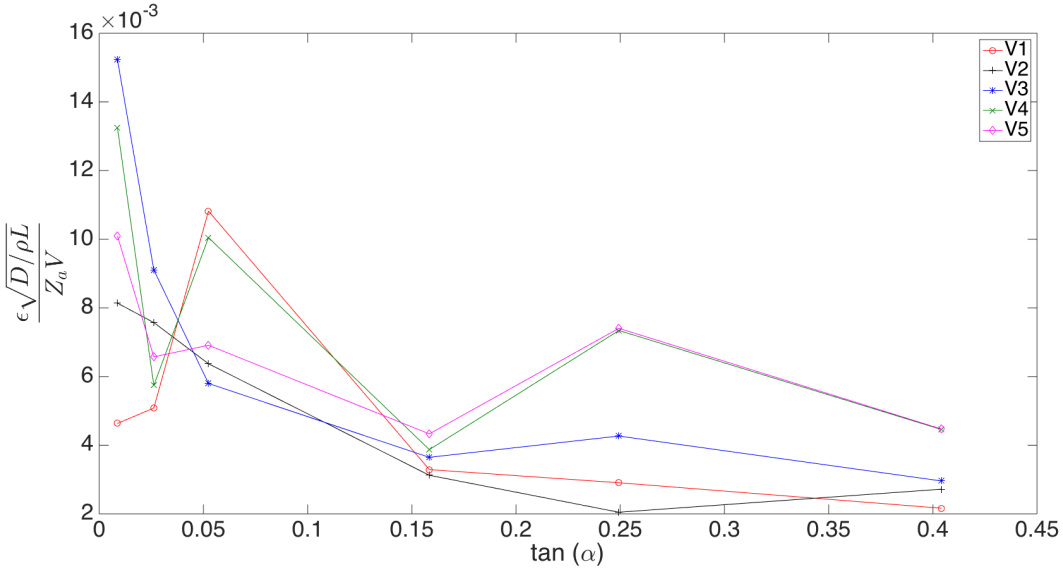

Figure 6.12: Results from the FSI-simulation series with stiffness of the plate equal to D3 with different impact velocities and deadrise angles when assuming that the plate responds hydroelastic

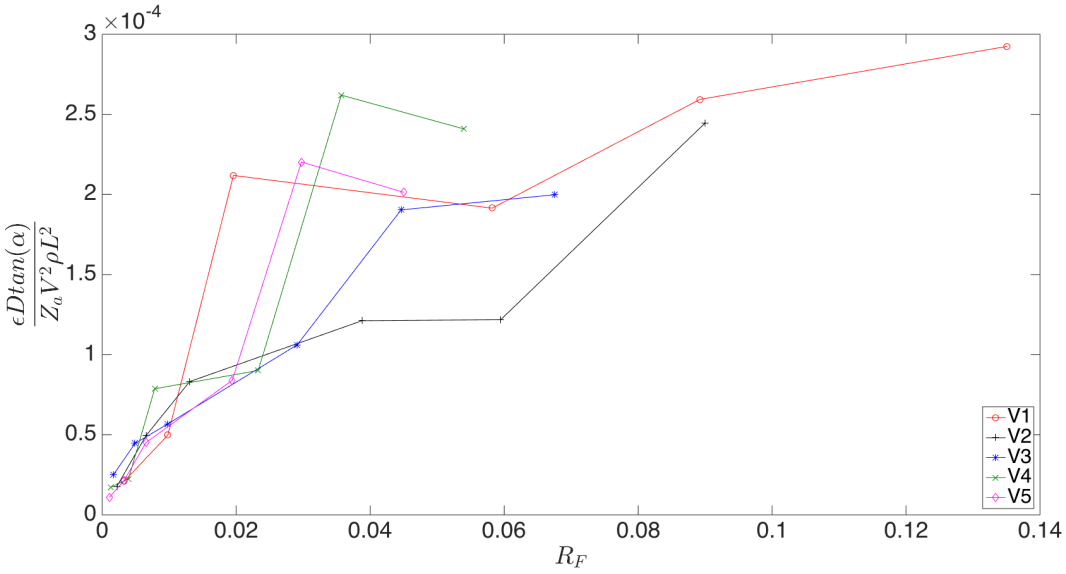

Figure 6.13: Results from the FSI-simulation series with stiffness of the plate equal to D3 with different impact velocities and deadrise angles compared again the quasi-static hydroelastic beam theory assuming that the plate responds quasi-steady while utilizing the hydroelastic factor R_F defined in equation 4.2

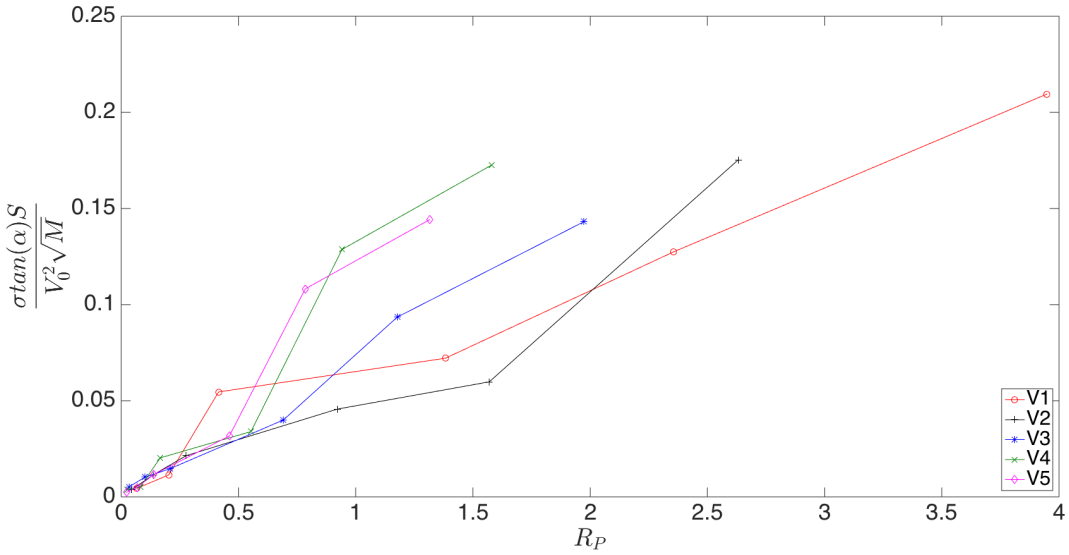

Figure 6.14: Results from the FSI-simulation series with stiffness of the plate equal to D3 with different impact velocities and deadrise angles when applying the theory in Panciroli (2005)

6.5.2 Results from D4-series

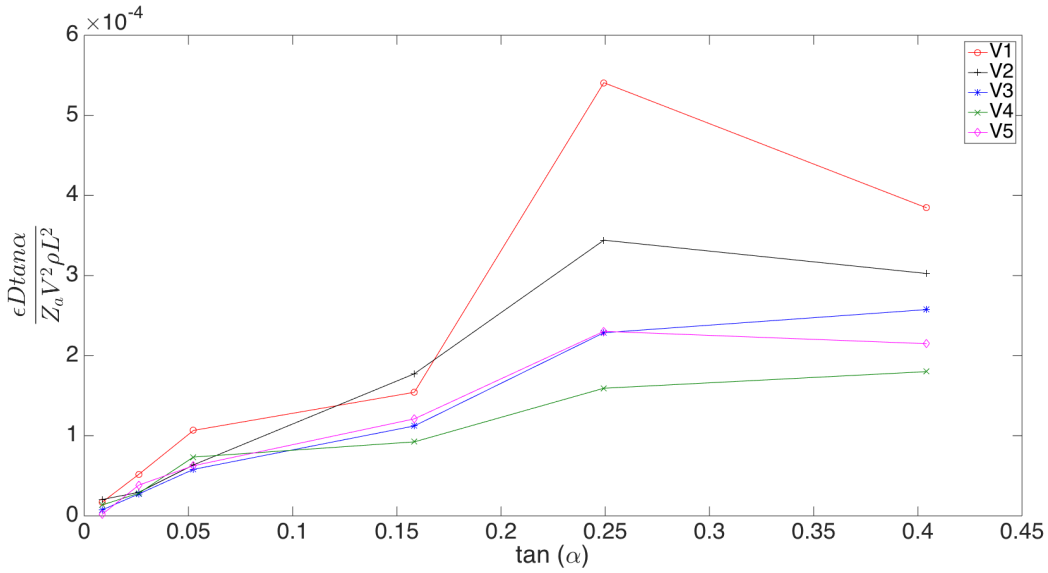

Figure 6.15: Results from the FSI-simulation series with stiffness of the plate equal to D4 with different impact velocities and deadrise angles compared again the quasi-static hydroelastic beam theory when assuming that the plate responds quasi-steady

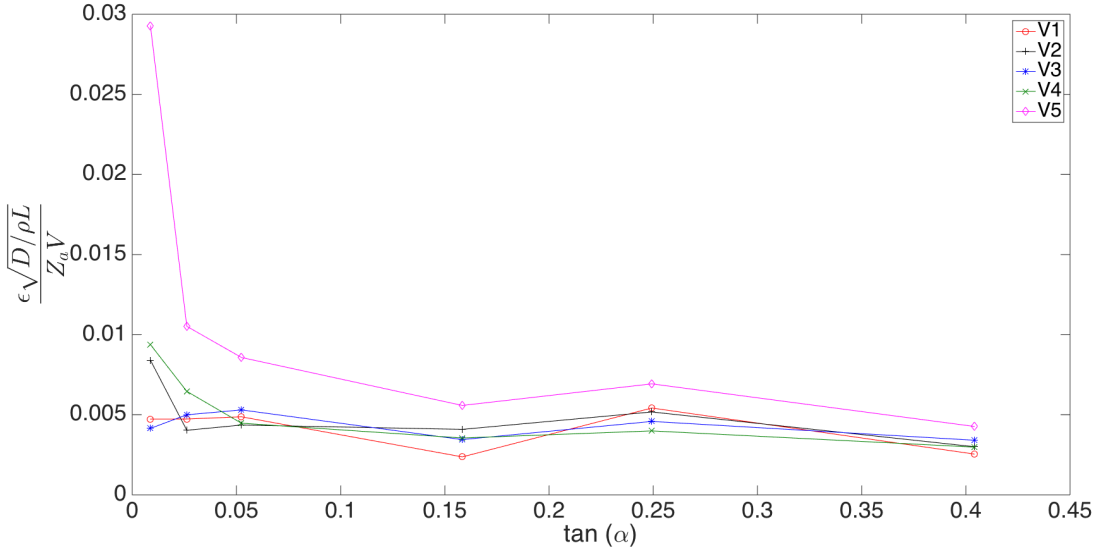

Figure 6.16: Results from the FSI-simulation series with stiffness of the plate equal to D4 with different impact velocities and deadrise angles when assuming that the plate responds hydroelastic

In figures 6.15, 6.16, 6.17 and 6.18 can we see the results from 30 FSI-analysis when evaluating the strain in the plate and non-dimensionalized them as described above. The results will be commented in section 6.8.

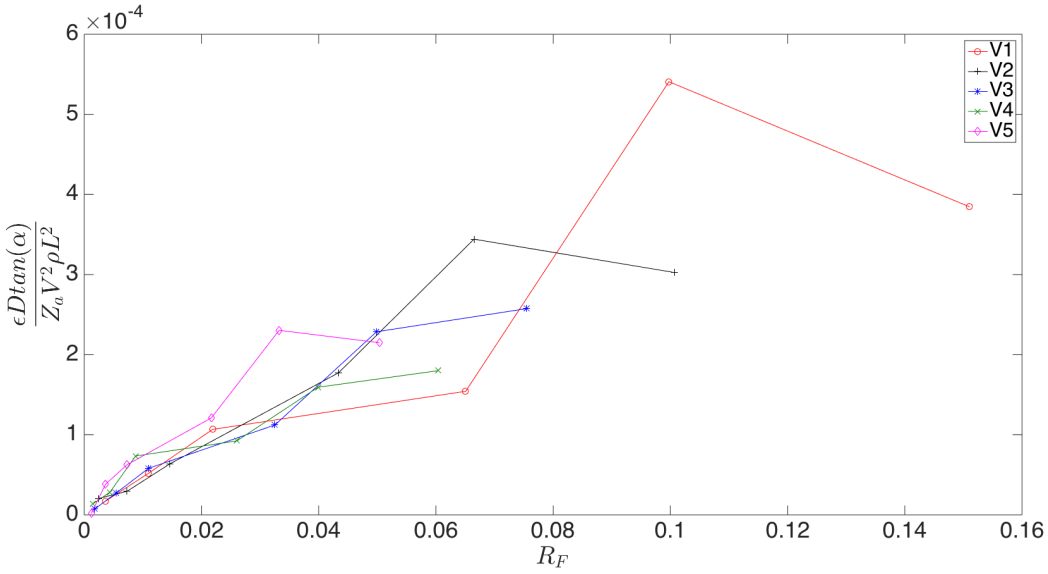

Figure 6.17: Results from the FSI-simulation series with stiffness of the plate equal to D4 with different impact velocities and deadrise angles compared again the quasi-static hydroelastic beam theory assuming that the plate responds quasi-steady while utilizing the hydroelastic factor R_F defined in equation 4.2

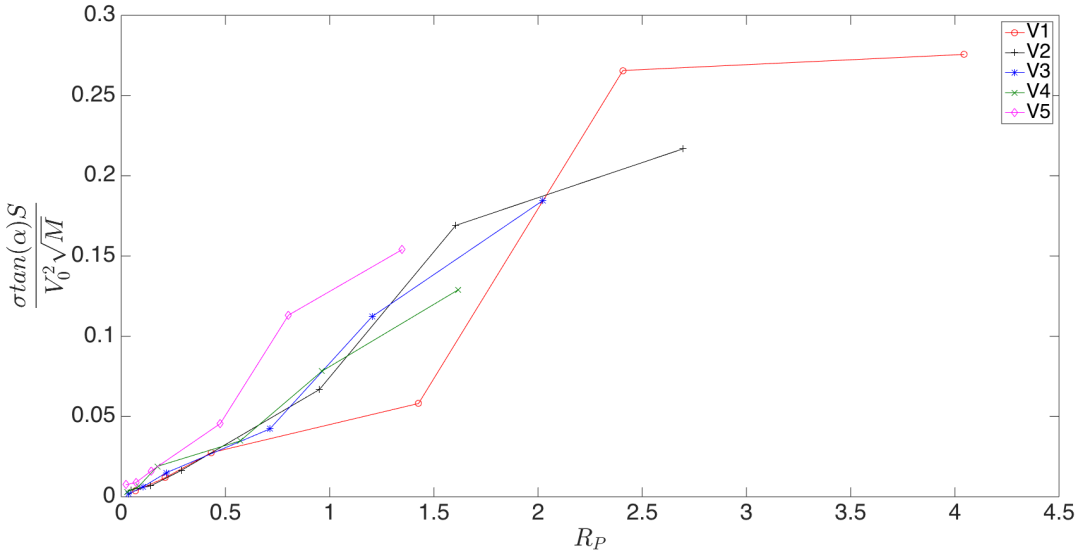

Figure 6.18: Results from the FSI-simulation series with stiffness of the plate equal to D4 with different impact velocities and deadrise angles when applying the theory in Panciroli (2005)

6.5.3 Results from D5-series

In figures 6.19, 6.20, 6.21 and 6.22 can we see the results from 30 FSI-analysis when evaluating the strain in the plate and non-dimensionalized them as described above. The results will be commented in section 6.8.

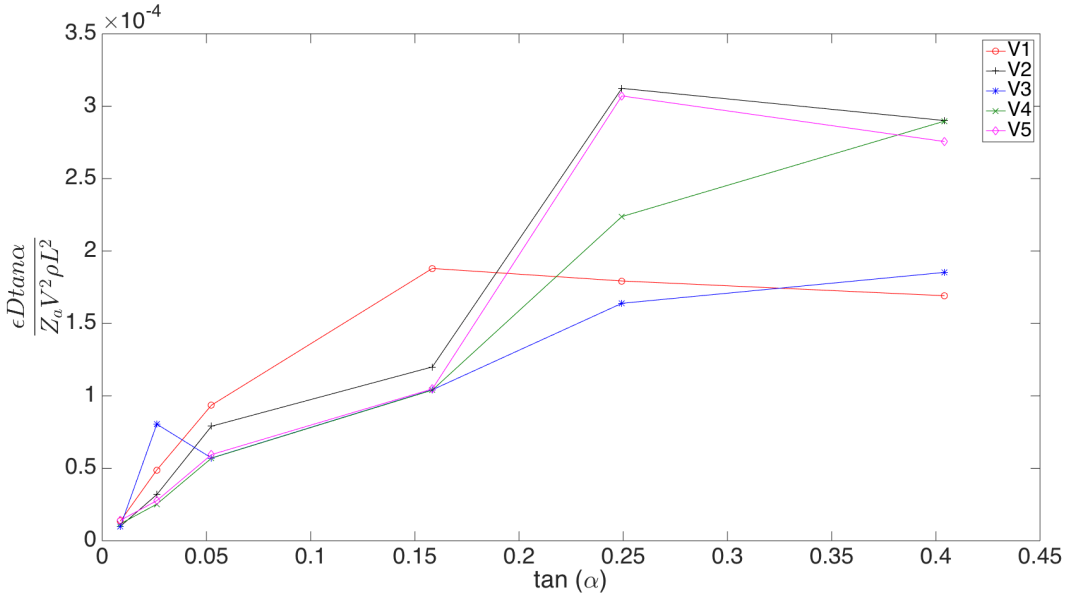

Figure 6.19: Results from the FSI-simulation series with stiffness of the plate equal to D5 with different impact velocities and deadrise angles compared again the quasi-static hydroelastic beam theory when assuming that the plate responds quasi-steady

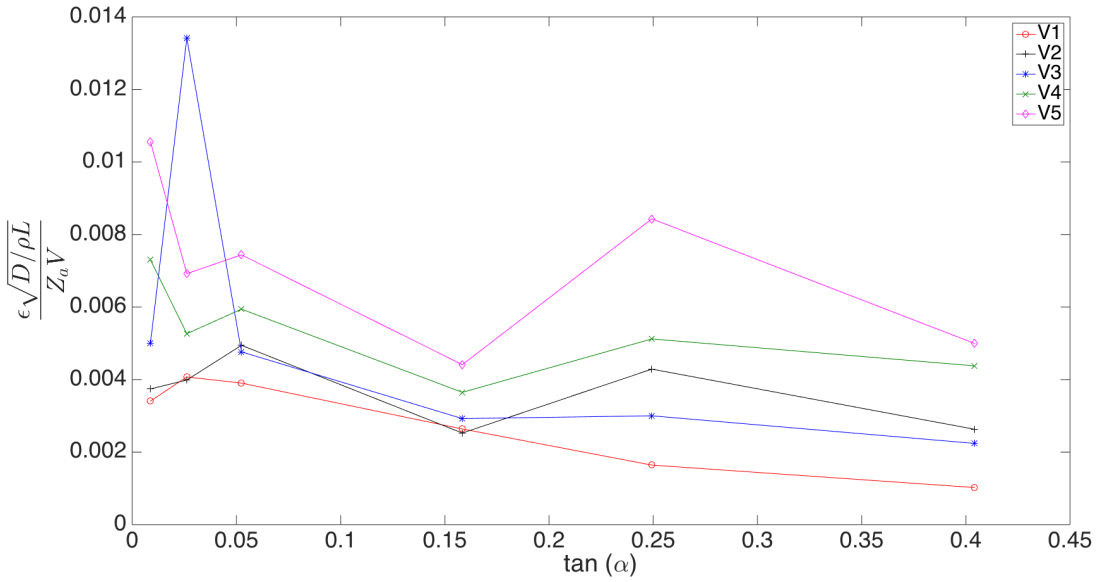

Figure 6.20: Results from the FSI-simulation series with stiffness of the plate equal to D5 with different impact velocities and deadrise angles when assuming that the plate responds hydroelastic

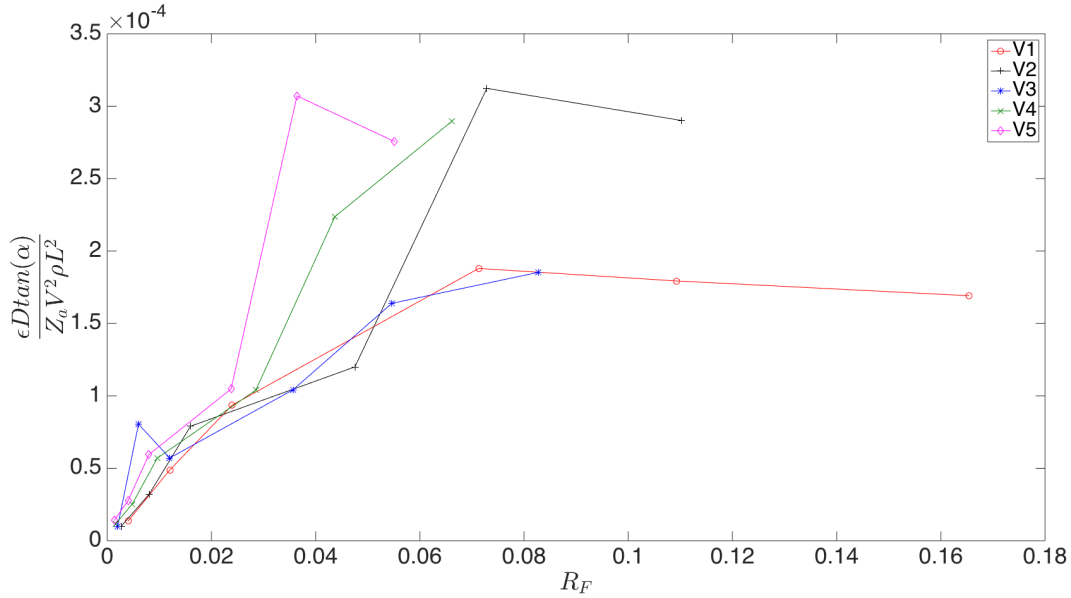

Figure 6.21: Results from the FSI-simulation series with stiffness of the plate equal to D4 with different impact velocities and deadrise angles compared again the quasi-static hydroelastic beam theory assuming that the plate responds quasi-steady while utilizing the hydroelastic factor R_F defined in equation 4.2

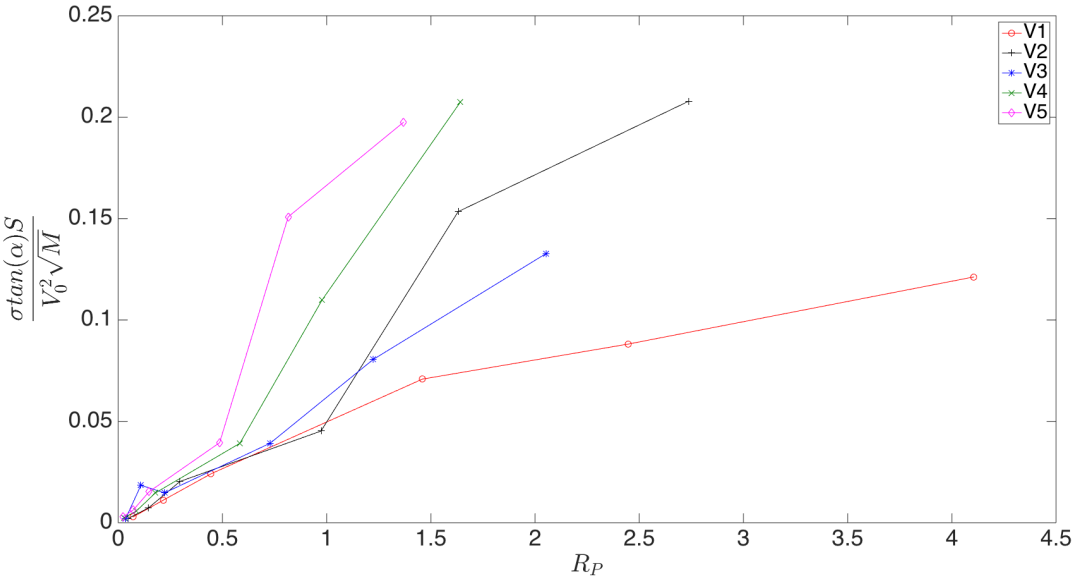

Figure 6.22: Results from the FSI-simulation series with stiffness of the plate equal to D5 with different impact velocities and deadrise angles when applying the theory in Panciroli (2005)

6.5.4 Results from D60-series

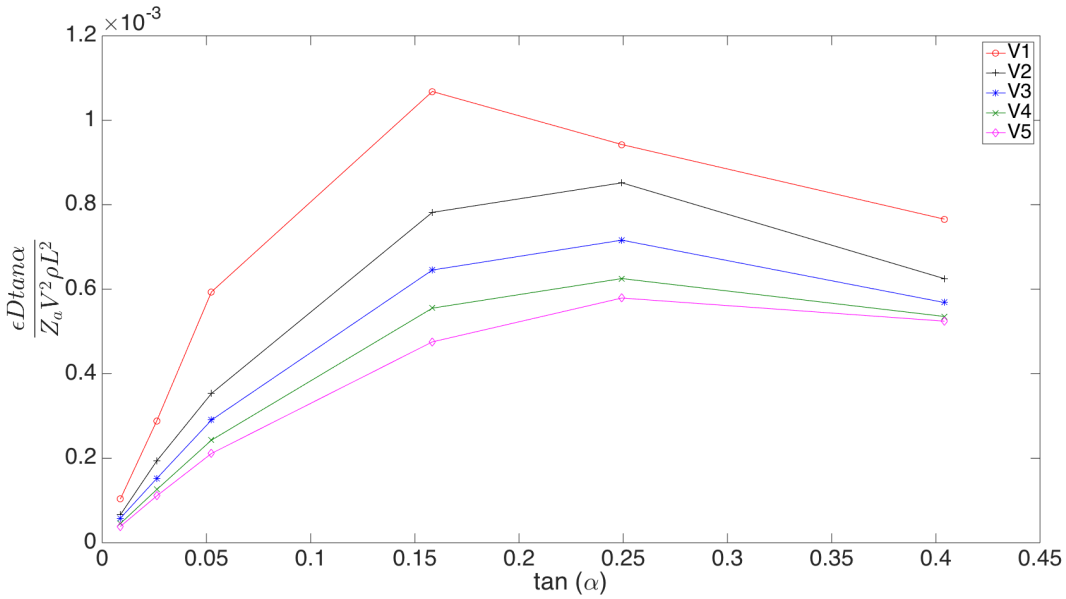

Figure 6.23: Results from the FSI-simulation series with stiffness of the plate equal to D60 with different impact velocities and deadrise angles compared again the quasi-static hydroelastic beam theory when assuming that the plate responds quasi-steady

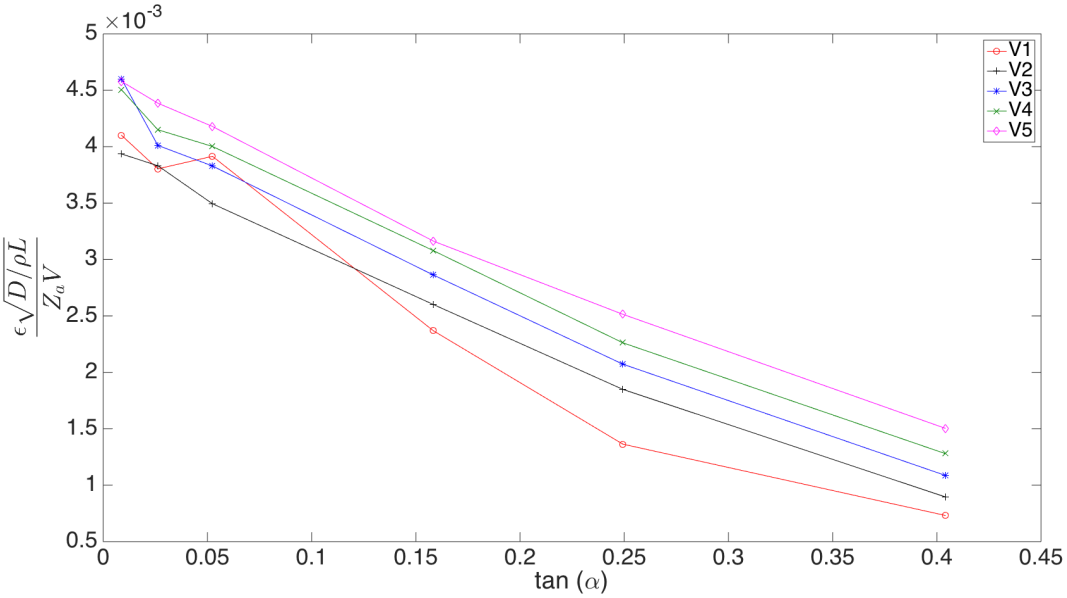

Figure 6.24: Results from the FSI-simulation series with stiffness of the plate equal to D60 with different impact velocities and deadrise angles when assuming that the plate responds hydroelastic

In figures 6.23, 6.24, 6.25 and 6.26 can we see the results from 30 FSI-analysis when evaluating the strain in the plate and non-dimensionalized them as described above. The results will be commented in section 6.8.

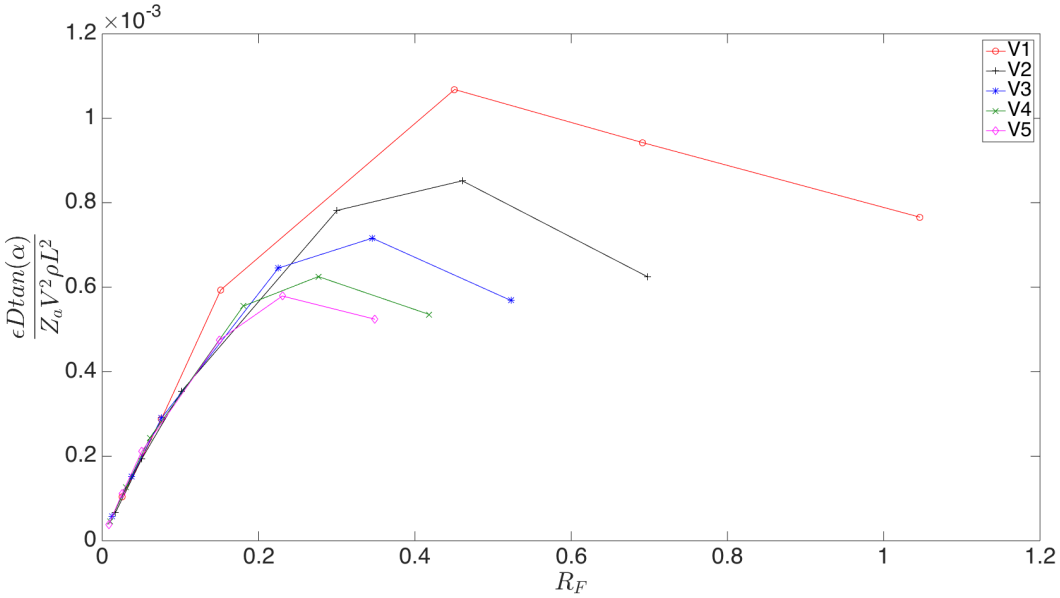

Figure 6.25: Results from the FSI-simulation series with stiffness of the plate equal to D60 with different impact velocities and deadrise angles compared again the quasi-static hydroelastic beam theory assuming that the plate responds quasi-steady while utilizing the hydroelastic factor R_F defined in equation 4.2

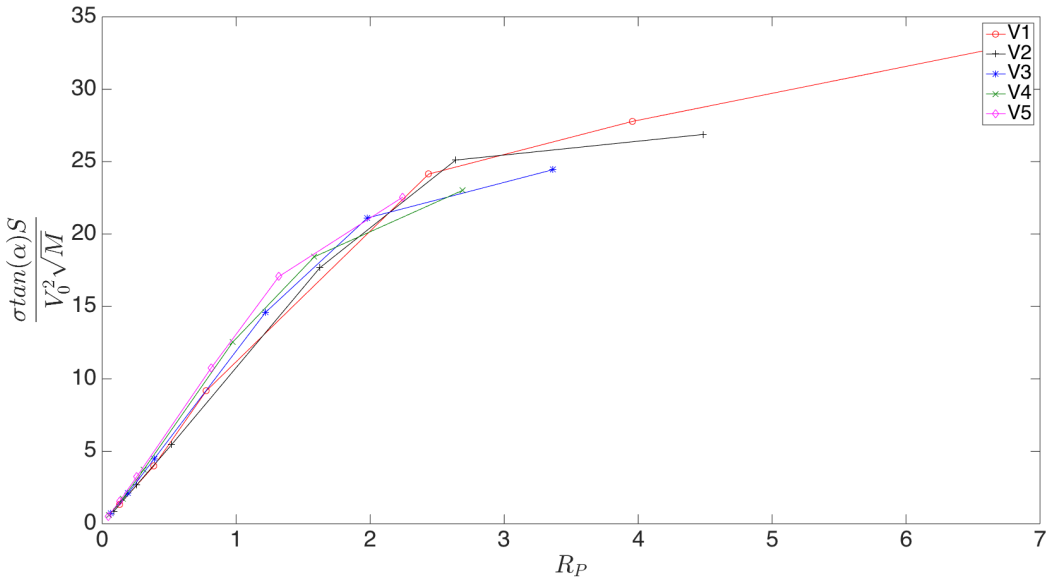

Figure 6.26: Results from the FSI-simulation series with stiffness of the plate equal to D60 with different impact velocities and deadrise angles when applying the theory in Panciroli (2005)

6.5.5 Comparison Between the Series

In figures 6.27, 6.28, 6.29 and 6.30 can we see the results from 120 simulations when they are made dimensionless are specified earlier. The results will be commented in section 6.8.

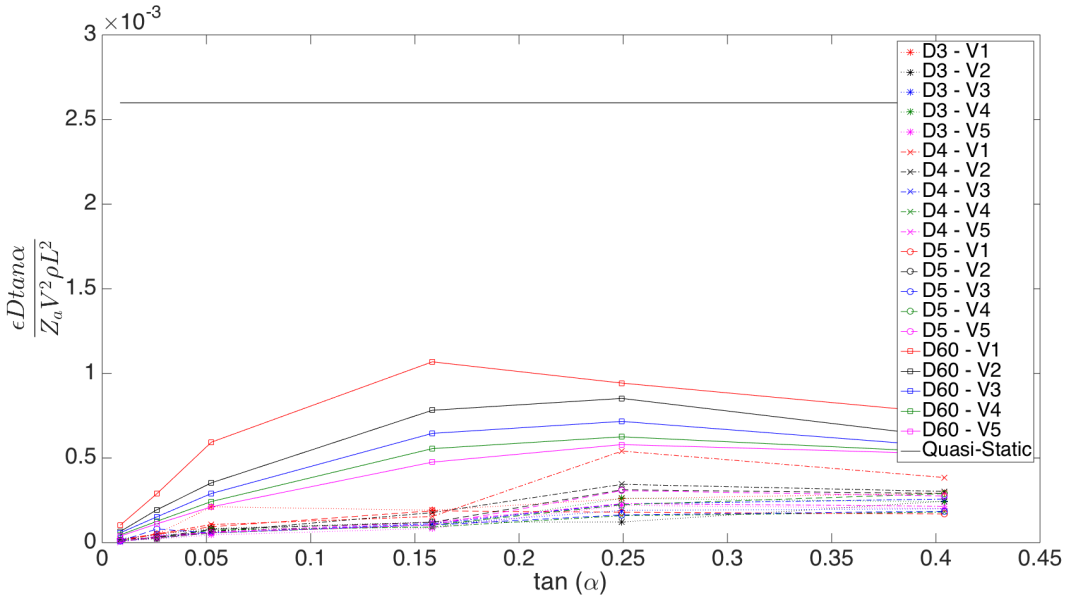

Figure 6.27: Results from the FSI-simulation series with different plate stiffness (D) with different impact velocities (V) and deadrise angles (α) compared again the quasi-static hydroelastic beam theory when assuming that the plate responds quasi-steady

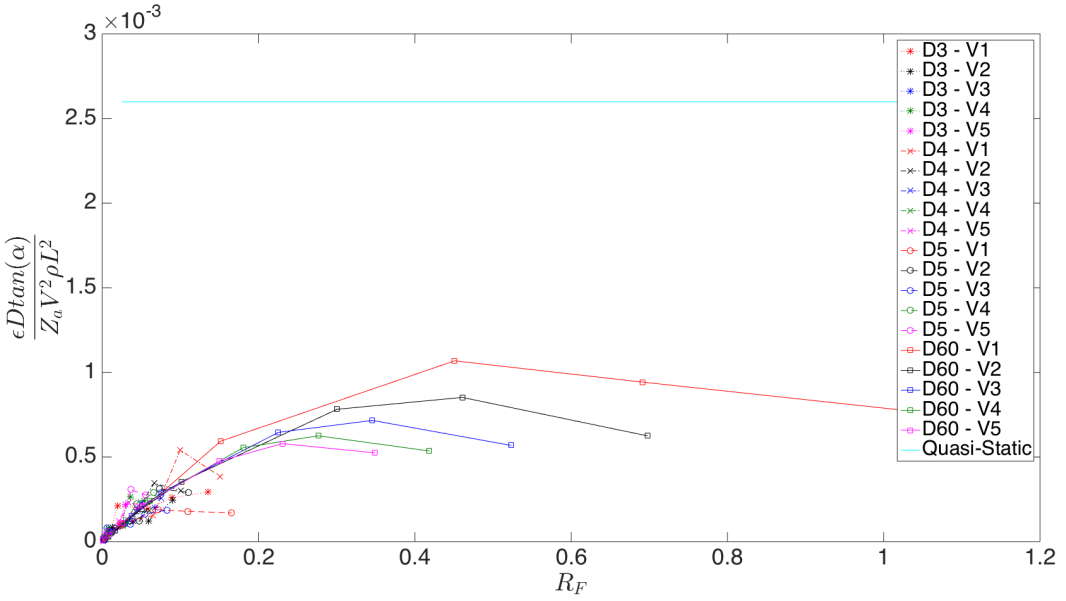

Figure 6.28: Results from the FSI-simulation series with different plate stiffness (D) with different impact velocities (V) and deadrise angles (α) compared again the quasi-static hydroelastic beam theory assuming that the plate responds quasi-steady while utilizing the hydroelastic factor R_F defined in equation 4.2

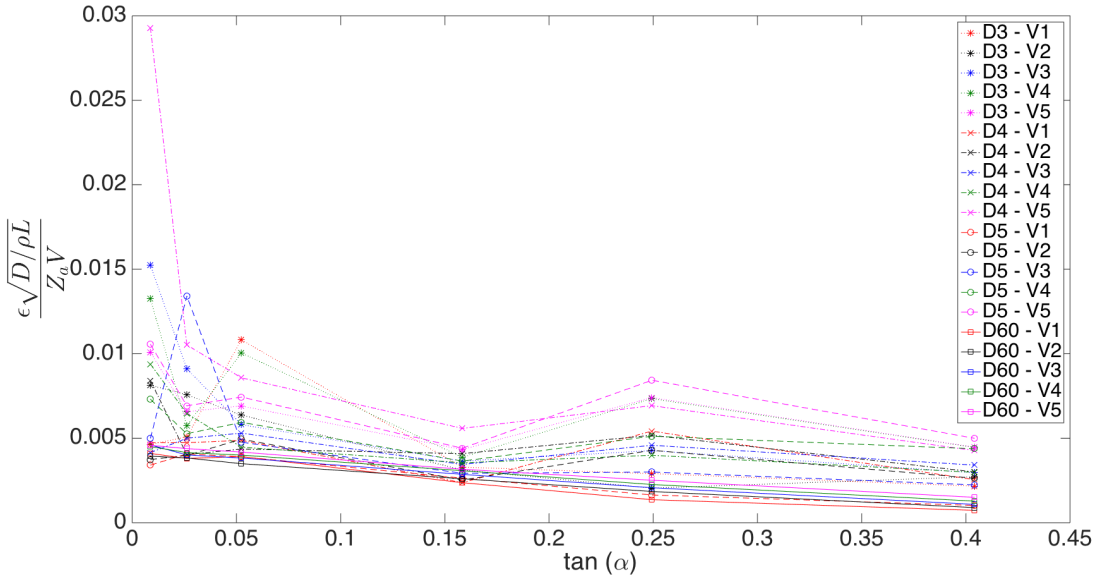

Figure 6.29: Results from the FSI-simulation series with different plate stiffness (D) with different impact velocities (V) and deadrise angles (α) when assuming that the plate responds hydroelastic

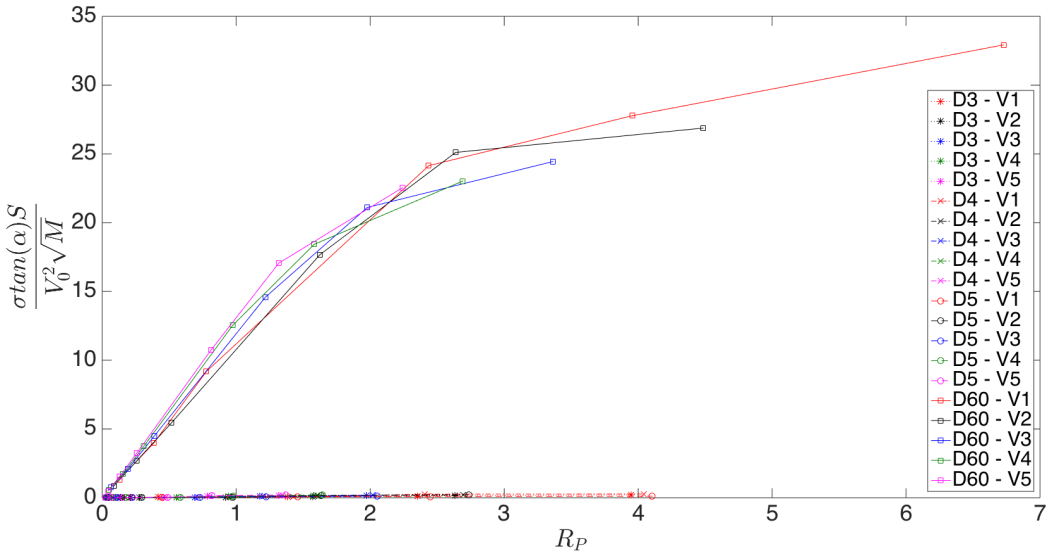

Figure 6.30: Results from the FSI-simulation series with different plate stiffness (D) with different impact velocities (V) and deadrise angles (α) when applying the theory in Panciroli (2005)

6.6 Parametric Study of Impact Velocity

In order to achieve a wider understanding of when it is important to account for hydroelasticity, a simulation series has been performed with the model used in chapter 5. In this section, the only change will be the initial velocity of the hull. The section is still dropped 10 cm above the free surface with an initial velocity. Two simulations are performed from stand still and dropped from a different distance above the free water surface. This is done in order to assure that R_B is varied.

First a series of rigid CFD-simulations are performed with the different initial velocities. The plot of hydrodynamic load on the hull, obtained from the series, is used to find the load duration. Such a plot can be seen in figure 6.31. The first dry eigenperiod is specified in table 5.2. With this information the ratio R_B can be found.

After this, co-simulations are performed in the same manner as in chapter 5 - the only difference is the initial velocity, and in two simulations, the distance from the keel to free water surface.

The strain is evaluated as described in figure 6.1. It was found that this model was more stable for higher velocities than the models used in section 6.5. This is probably due to the correct stiffness of the springs and the fact that the original design is preserved.

6.6.1 Rigid CFD

The different initial velocities and the resulting ratios (R_B) are found in table 6.4. For most cases, the hull is dropped 10 cm above the free surface with an initial velocity. For other cases, the initial velocity is removed and one simulation the hull is dropped from stand still at a different height. The initial velocity is found by using an equivalent drop height. It is easy to find the velocity with basic kinematic equations: $V = \sqrt{2gh}$. Where g is the gravity and h is the drop height. The load duration is found from the hydrodynamic force. An example of the hydrodynamic force plot can be seen in figure 6.31. The load duration is derived from the shape of the peak in this figure. This peak is approximated as a triangle and the base of this triangle represents the load duration used in R_B. For the case in figure 6.31, the load duration is approximated to be 0.007 s.

Table 6.4: Results from the different rigid CFD analysis

Name	Equivalent Drop Height [m]	Initial Velocity $[\frac{m}{s}]$	Load Duration [s]	R_B
V1	0.005	0	0.075	0.413
V2	[-]	0.1	0.0445	0.245
V3	[-]	0.5	0.0425	0.234
V4	[-]	1	0.035	0.193
V5	1	4.43	0.02	0.110
V6	2	6.26	0.01375	0.076
V7	[-]	7.45	0.01	0.055
V8	5	9.90	0.008	0.044
V9	6	10.85	0.007	0.038
V10	7	11.71	0.0065	0.036
V11	8	12.52	0.0064	0.035
V12	9	13.29	0.006	0.033
V13	10	14.01	0.00583	0.032
V14	12	15.34	0.0055	0.030
V15	35	26.20	0.00425	0.023

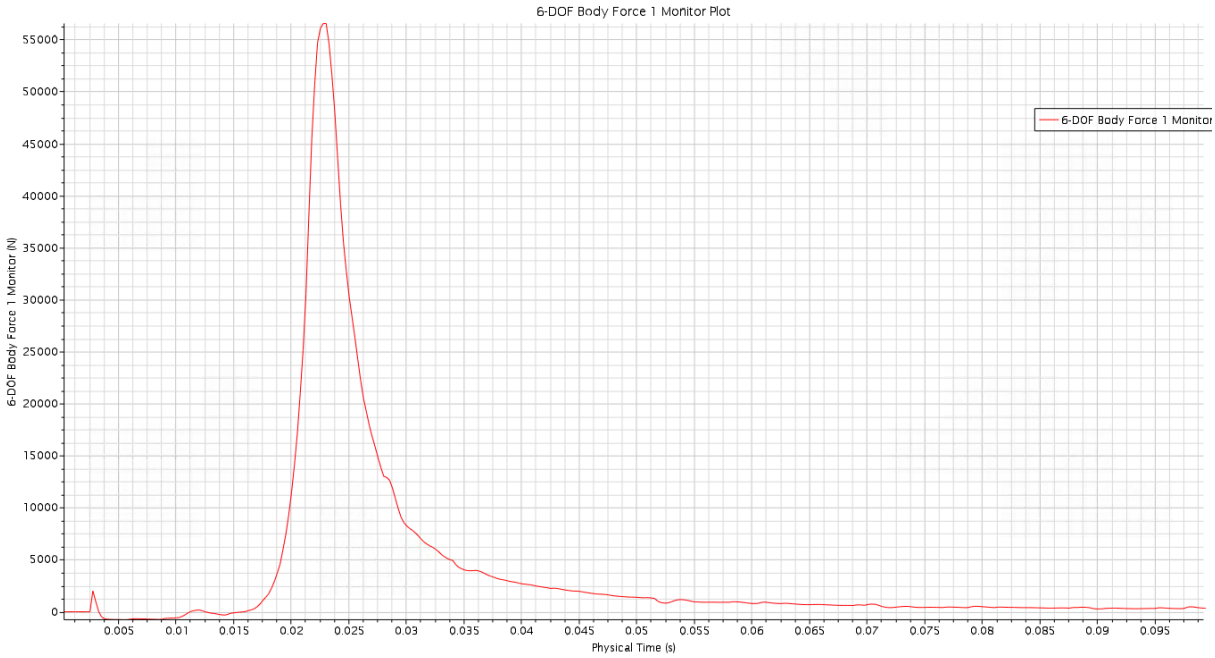

Figure 6.31: Time series of hydrodynamic force on the hull in the simulation V9

6.6.2 Results

Since the velocity is the only variable in the series, it is less complicated to compare the results. The maximum strain in the plate has been divided with the impact velocity squared. This is based on the non-dimensional methods presented in Faltinsen (1999b) under the assumption that the structure responds quasi-steady (follows the dynamic load). The y-axis in figure 6.33 represents the maximum strain in the point divided by the impact velocity squared while the x-axis contains R_B.

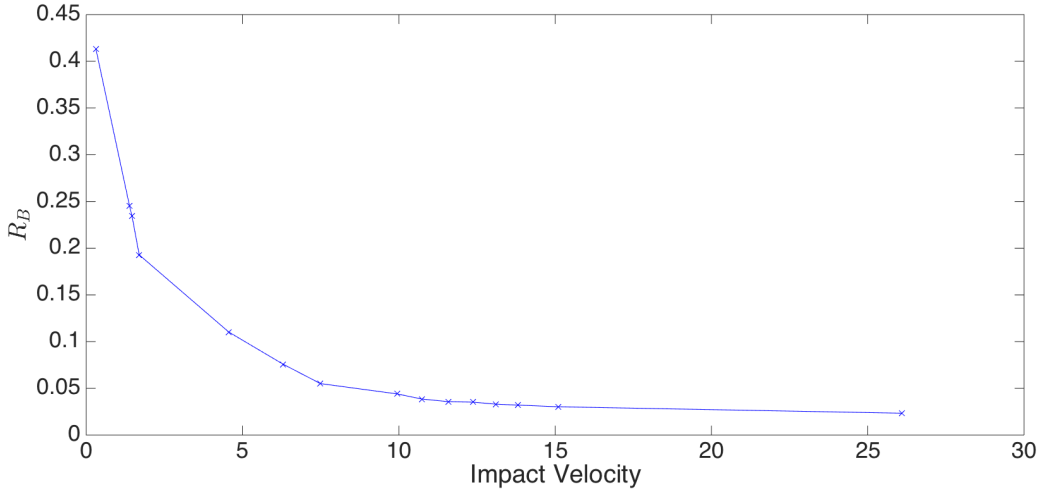

Figure 6.32: R_B versus the impact velocity

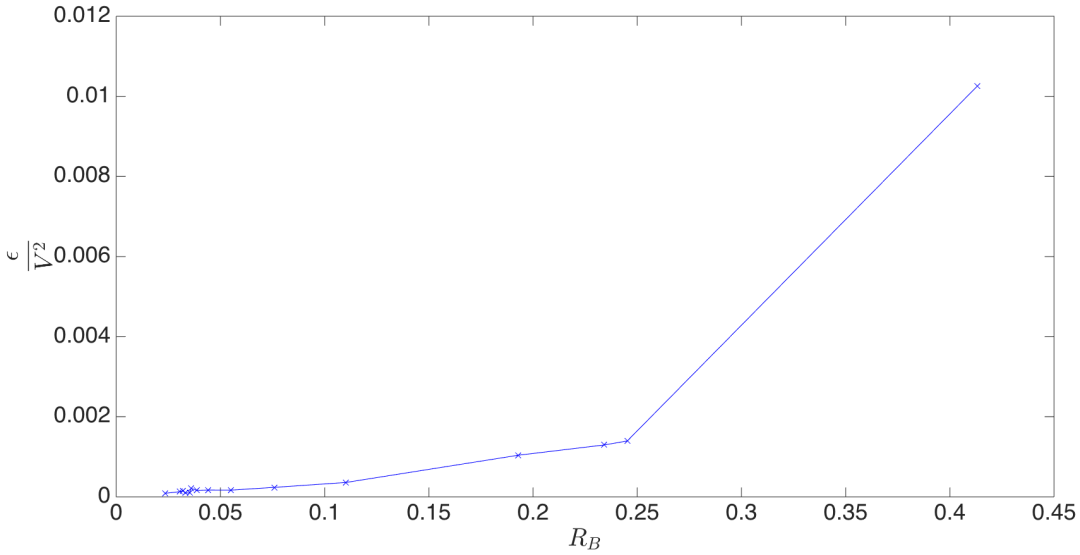

Figure 6.33: Nondimentional strains from the co-simulations - the strains are non-dimensionalized assuming quasi-steady response and associated with R_B

The results from the simulations can be found in figures 6.32 and 6.33. Figure 6.32 shows the correlation between the ratio R_B and the impact velocity. As expected, a lower impact velocity yields a higher ratio R_B as the load duration gets longer. Figure 6.33 shows the nondimentional strains from the co-simulation. One can clearly see the effect from the ratio R_B. We can observe that as the load period gets longer with respect to the eigenperiod, the effect from hydroelasticity is reduced. The strain gets more dependent on the pressure (velocity squared) and we can at some point treat the problem as quasi-static with a one-way interaction analysis method. The results tends to a lower degree of hydroelasticity when R_B gets higher as demonstrated in Faltinsen (1999b) and Bereznitski (2001). The ratio R_B defined in equation 4.4 appears as a suitable decision factor when it is important to account for hydroelasticity. It was difficult to obtain $R_B > 2$ since the drop height must be even lower - this will influence the numerical results as the free water surface is smeared out due to the VoF-method.

6.7 Error Sources

As the parametric study is a purely numerical study and there is no evidence to support the results, it is paramount to be critical with respect to what kind of errors exist.

6.7.1 Modelling Error

The biggest concern regarding modeling errors is the reduction from 3D to a 2D-section. In chapter 5.4.1, the mass for the 2D-section was tuned so that the inertia force would resemble the inertia force in the full-scale test. This is not an optimal approach, since the model is tuned so that the maximum acceleration in the simulation would be equal to the maximum acceleration in the full-scale test, by using the results from the full-scale test. However, this turned out to be a reasonable approach, since the time series follow each other closely after the point of maximum acceleration. They have approximately the same oscillation period.

To account for the structural stiffness and geometrical stiffness of the 3D-hull, several springs were applied on the 2D-section. The process of finding the spring constants are somewhat straight forward and is considered by the author to be correct. A possible weakness might lie in non-linear interaction effects, which can occur when the load is increased above or below a certain point. This should have been examined further, as only one load was applied. A better approach would be to use several loads and take the mean of the obtained results in order to capture non-linear effects (if they are present) or to use non-linear springs. In addition, the springs will interact dynamically and lead to some unphysical eigenmodes in the 2D-section. The first eigenmode introduced by the springs is among the five first eigenmodes of the structure. This means that it will most likely be activated during impact. Ideally it would be better to apply more springs - the problem here is that they need to be conformal with respect to the 2D-model and the 3D-model. As there exists only a limited number of reference points, the maximum number of springs that are truly conformal has been applied. If more springs are going to be applied, these would have been placed in a less accurate manner. It is observed that the springs interact during impact and contribution to the response of the hull.

Another problem with the reduction from 3D to 2D is that the slamming pressure will be different as the 3D section would include end effects, which will influence the results. In addition, a bow and stern wave will appear. These waves represent a loss in energy and would alter motion characteristics of the hull.

An other improvement would be to find a new mesh for each case in the parametric study. This is due to the fact that they all will behave differently, hence should a convergence study be performed for all. This is however very inconvenient and would be very ineffective.

6.7.2 Instabilities

Repetition

In order to find out if the solution domain is subject to instabilities or bifurcation points (in the structural domain), it is necessary to repeat the simulations in order to find out if they yield the same result. If they display the same maximum strain (which is the focus in this thesis) the problem is stable and not subject to instabilities or bifurcation points. If they yield different maximum strains, the simulation is unstable and might contain several possible solutions, as the structure can take a different response path for each simulation.

A simulation with a deadrise angle equal to $\alpha = 1.5$ degrees, material properties equal to D5, and initial velocity equal to V3, has been performed twice. The strain time history of the two simulation can be viewed in figure 6.34. The strain is evaluated at the same location as specified

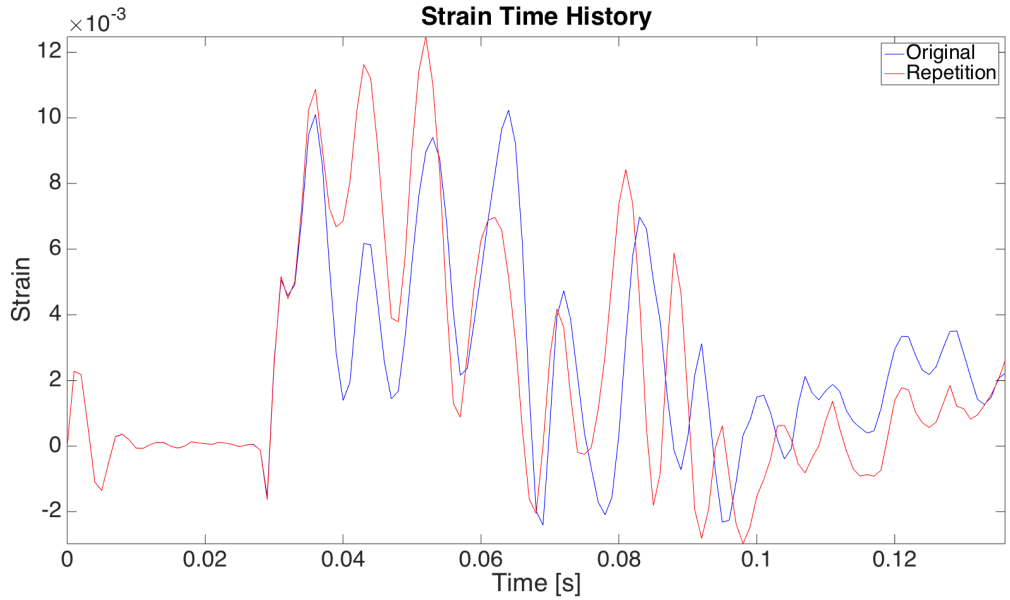

Figure 6.34: Unfiltered strain time history from two simulations with equal initial conditions. Impact occurs at t = 0.014 s

in figure 6.1. As we can observe there exists a difference between the two simulations, even though they have the same settings. This indicates that the simulations are unstable. The maximum strain for the original simulation is 0.0102, while in repetition simulation the maximum strain is 0.0125. This yields a difference in maximum strain of 17.9 %. This is quite significant and it can be concluded that the simulation is unstable. The appearance of the two simulations is very equal and there exists only a small phase shift. We can observe that the different simulations are equal until a certain point after impact (about 0.035 s). It can be observed that the difference starts to occur when the plate starts to vibrate. We can understand that the instability occurs when the plate experiences fast vibrations.

In order to determine how significant the difference is, in total nine repetition simulations have been performed. The time history from these nine simulations can be viewed in appendix G.

An uncertainty analysis will be performed in order to quantify the precision error. This is found using the theory presented in Steen (2014). The sentral equations are defined below, for a more thorough introduction please refer to Steen (2014).

$$\bar{\varepsilon} = \frac{1}{N}\Sigma_{j=1}^{N}\varepsilon_j \tag{6.8}$$

$$S_\varepsilon = \sqrt{\frac{1}{N-1}\Sigma_{j=1}^{N}(\varepsilon_j - \bar{\varepsilon})} \tag{6.9}$$

$$P_\varepsilon = S_\varepsilon t_{N-1} \tag{6.10}$$

$$U_\varepsilon = \frac{P_\varepsilon}{\bar{\varepsilon}} \tag{6.11}$$

$$S_{\bar{\varepsilon}} = \frac{S_\varepsilon}{\sqrt{N}} \tag{6.12}$$

$$P_{\bar{\varepsilon}} = t\frac{S_\varepsilon}{\sqrt{N}} \tag{6.13}$$

$$U_{\bar{\varepsilon}} = \frac{P_{\bar{\varepsilon}}}{\bar{\varepsilon}} \tag{6.14}$$

$$\tag{6.15}$$

$\bar{\varepsilon}$ is the mean of the population, S_ε is the standard deviation of the population, P_ε is the precision limit for a single sample in the population, U_ε is the uncertainty of a single sample in the population, $S_{\bar{\varepsilon}}$ is the standard deviation of the mean of the population, $P_{\bar{\varepsilon}}$ is the precision limit for the mean of the population, $U_{\bar{\varepsilon}}$ is the uncertainty of the mean of the population. N is the number of samples in the population, t_{N-1} is the value of the inverse t-distribution cumulative density function with $N-1$ degrees of freedom within a defined confidence interval. In the table

Table 6.5: Values and Results from Uncertainty Analysis

N	9
Confidence	95 %
t_{N-1}	2.31
$\bar{\varepsilon}$	0.0104
S_ε	0.0015
P_ε	0.0034
U_ε	32.4 %
$S_{\bar{\varepsilon}}$	0.0005
$P_{\bar{\varepsilon}}$	0.0011
$U_{\bar{\varepsilon}}$	10.8 %

6.5 we can see the results from the uncertainty analysis. The values in the population are the maximum strain from the nine different simulations evaluated in the same place as specified in figure 6.1. This means that $\bar{\varepsilon} \pm P_{\bar{\varepsilon}}$ is equal to 0.0104 ± 0.0011. The consequence is that the true mean μ_T is within this value with a 95 % confidence. The true mean would yield the correct results if the systematic error is zero. This yields an uncertainty of 10.8 %.

Sensitivity Study

Another way to check for instabilities is to perform a sensitivity study. Here a parameter is subjected to a small alteration. The goal is to observe if a small change yields a huge amplification in the results; if a huge amplification occurs this can indicate that the problem has conservation problems.

The simulation with a deadrise angle equal to $\alpha = 3$ degrees, material properties equal to D5, and initial velocity equal to V3, is chosen. In the first simulation, the initial velocity is equal to 7.452 $[\frac{m}{s}]$, the second 7.442 $[\frac{m}{s}]$ and the third 7.462 $[\frac{m}{s}]$. The results from the three simulations can be viewed in figure 6.35.

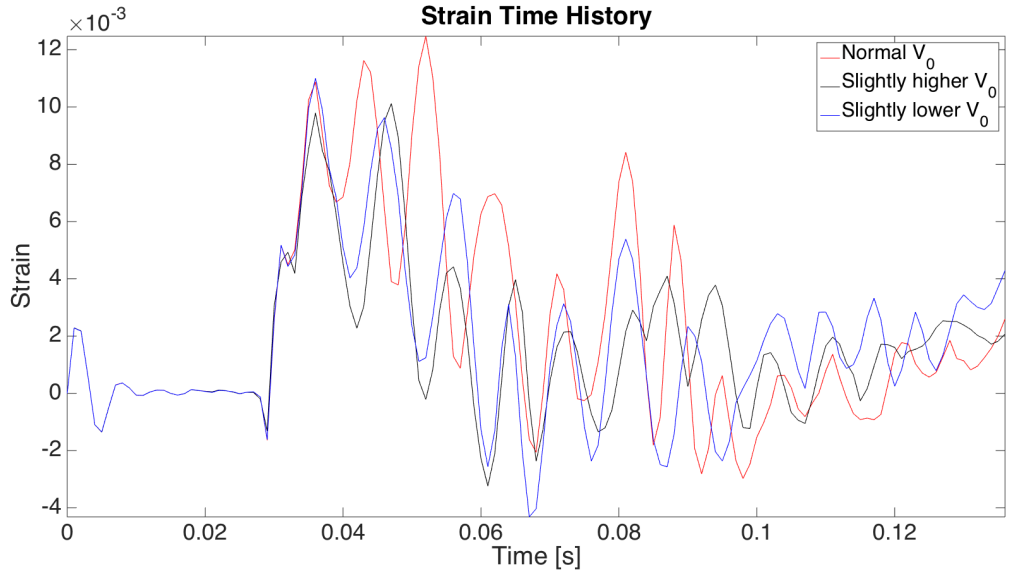

Figure 6.35: Unfiltered strain time history from three simulations with a slightly different initial velocity. Impact occurs at t = 0.014 s

The strain is evaluated at the same location as specified in figure 6.1. We can observe that the three simulations yield different maximum strains when the initial velocity is slightly different. The difference in maximum strain from the original to the simulation with a slightly higher velocity is 18.8 % and difference from the simulation with a slightly lower is 11.7 %. As the difference in the initial velocity is only 0.13 %, the obtained difference in the strain is a much larger amplification than expected. This could indicate that the simulation is unstable. The appearances of the three simulations are equal and phase shift exists as expected. We can observe the same for the sensitivity study as the repetition study. The simulations are equal in the beginning, but after while impact does the difference occur. This occurs when the plate experience fast vibrations.

6.7.3 Numerical Parameters

There are several improvements regarding the numerical parameters that could have been implemented in the simulations. These are mainly related to the time step and coupling time step.

As showed in chapter 5.5, this had little effect. However, this is probably due to the way the additional mass of the 2D-section was found. In the current chapter, we do not compare the results with a full-scale test or experiment. It would therefore be interesting to examine the effects from changes in the time step in Star-CCM+, and the coupling time step between Abaqus and Star-CCM+ considering the strain. However, if the time step and coupling step were lower, this would lead to even longer simulation times. With the current set-up the total simulation time is 8-9 hours per simulation. If we would apply an even smaller time step this would yield a significant increase in the simulation time. As over 135 simulations have been performed, this is significant in total. It is believable that the used set-up is sufficient to capture the physics of the hydroelastic event.

6.7.4 Accuracy of Results

It is difficult to say anything about the accuracy of the results as there exist anything that the results can be compared to. From chapter 5 it has been concluded that the model was able to recreate the acceleration of the hull in a good manner, even when the total mass was altered in order to achieve the same maximum acceleration. As only the acceleration was considered, it cannot be assumed that the same quality applies for the stain. However, as indicated by Arai M. (1998), the acceleration time history is important for the strain time history. This could further be emphasized by equation 3.10, where the acceleration is central. Based on this we can understand that if the simulation is able to recreate the acceleration time history, the simulation should be able to recreate the strain time history. However, there exists no way to verify the obtained strain time history.

6.7.5 Conclusion Regarding Errors

In this section, several points which can affect the simulations have been pointed out. An important aspect is the additional mass, how it is found, and the fact that with this mass the section will not float. Another important point is that the eigenmodes that the springs introduce can easy be activated. The most important discovery is that the simulation appears to be unstable, as the repetition study yield a significant different results. The sensitivity study also demonstrates that the simulation amplifies a small increase in velocity. It is reasonable to assume that the reason for these problems lies in the structural problem and more specifically the equilibrium equation when incorporating non-linear geometry. Shells and plates in the structure will experience compression or other complex load situation and based on the load situation they can experience bifurcations or limit points. Bifurcation points are instability points where the structure might respond in several different ways or a slight variation in a parameter can have a significant impact on the response. An example of this is the phenomenon snap-back or snap-through which is related to buckling, (Moan, 2003). In a non-linear static analysis, these points are treated with different solution algorithms than normal such as arc-length methods based on Ritz-method, (Moan, 2003).

The hull is considered a perfect structure without imperfections. An example of this is buckling

of a perfect column. When the column is loaded with a compressive load, we only know that the column will buckle at some load, we do not know which direction it will buckle. However, if the column is subject to imperfections the buckling direction can be decided based on the imperfections. As the hull is a perfect structure, it can therefore have several response paths and we do not know which way it will respond when subjected to a complex loading situation. This supports the explanation of the instabilities, since the structure might respond in different ways each time.

The interaction with the eigenmodes introduced by the springs and bifurcation points is probably the reason why the simulations are not consistent. This in combination with the fact that during the free-vibration phase a lot happens in the plate and the implicit solver may not be able to capture everything. A possible action, in order to solve the latter problem, is to use an explicit solver; however, then we would lose the implicit coupling between the codes and this is not beneficiary. During the parametric study many of the FSI analysis quit early due to failure of the co-simulation engine. In most cases, this was related to problems within the Abaqus solver. When the structure reaches a bifurcation point several equilibrium positions exist, but the solver may not be able to reach convergence. This can be related to solution techniques or other aspects. An explicit solver might be better suited to solve these problems. The implicit solver requires convergence in each time step, while the explicit solver can accept that convergence did not happen in a single time step as along as the following time steps converges. The simulations experience the difference when the fast vibrations of the plate occur. This is the area on the time history which is the most difficult to solve, as many things happen in a short period of time. Thus can the solver have troubles finding equilibrium since the changes in forces and position is happening fast and it might not be able to track the structure properly.

As discussed in chapter 4.3 it has been shown that there exists a variance among the measured strain for a given impact velocity. This means that it can be expected that there exists a slight difference in the maximum strain when repetition is performed. An uncertainty analysis was performed and the results from nine repetition analysis were explored. It was found that uncertainty of the mean of the population is 10.8 %. This is a significant difference, but it is not known how significant with respect to the obtained variance in the experimental series as the value is not disclosed. The significance of the discovered errors is not clear, but their presence should be noted.

6.8 Discussion of Results

We can observe that the results in figures 6.11, 6.13, 6.15, 6.17, 6.19, 6.21, 6.23, 6.25, 6.27 and 6.28 are consistent with the conclusions in Faltinsen (1999b). The smaller the deadrise angle and the higher the impact velocity, the more important is the effect from hydroelasticity. This can be observed especially at the lowest deadrise angles in figure 6.11, 6.15, 6.19, 6.23 and 6.27. The highest velocities are represented lowest on the y-axis, this is in accordance with Faltinsen (1999b) as the effect from hydroelasticity is more important for higher impact velocities. The effect from deadrise angle and impact velocity is clear up to an angle of 9 degrees. The effect is especially clear for D60. After this, other effects will appear and influence the results such

that they appear more scattered and inconclusive. One possible explanation is that a deadrise angle above 9 degrees lies outside the typical design domain for a lifeboat. The consequence is that the structural geometric stiffness will be much lower. The section might not be able to withstand the forces due to little support from the buoyancy foam and the lower geometrical stiffness. A 2D-section where the deadrise angle is 22 degrees can be viewed in figure 6.36. If we compare this figure to figure 5.9 we can clearly see a difference. The above reasons can explain the scattered results from $\alpha = 9$ deg.

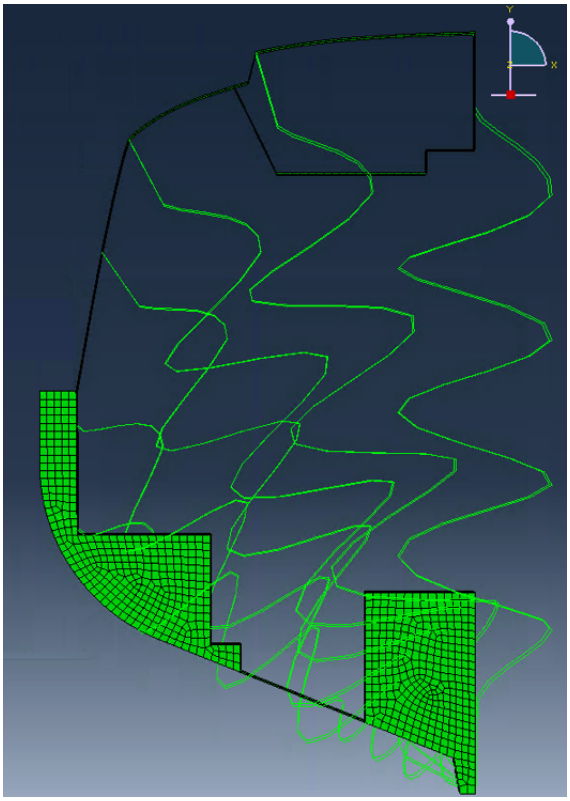

Figure 6.36: Mesh in Abaqus when α=22 deg. The springs can also be viewed in this figure

In figure 6.28 can we observe that the presented trend closely resembles the trend in figure 4.5. There exists a clear trend and most of the values lie on this trend. However, the values have not yet converged to the calculated quasi-static value even though R_F suggests that we should be close to a quasi-static value.

We can also observe that there exist some outliers from the general trend - these can be viewed in figure 6.11, 6.12, 6.15, 6.16, 6.19 and 6.20. If we examine the figures, a general trend can be seen and outside this trend exist some points - these are the outliers. After examination of the simulation result files, it was been concluded that the reason for these outliers is that an interaction effect between different eigenmodes of the structure occurs. This is not the case for the other results. Particularly, it is the activation of the eigenmode due to the springs that contributes. The dynamic behavior of the overbuilding and springs will also affect the strain response in the plate. The eigenfrequencies will change when the deadrise angle and material model changes. This can lead to that more eigenmodes can be activated during impact. The first eigenperiod can be viewed in table 6.6. The same interaction effect was observed in Faltinsen

(1999b).

Table 6.6: First eigenperiod of the hull applying different material properties and deadrise angles

	0.5 deg	1.5 deg	3 deg	9 deg	14 deg	22 deg
D3	0.3352	0.3303	0.3229	0.2931	0.2709	0.2619
D4	0.3216	0.3172	0.3105	0.2841	0.2650	0.2557
D5	0.3117	0.3077	0.3016	0.2777	0.2608	0.2518
D60	0.1752	0.1741	0.1725	0.1663	0.1612	0.1536

In figures 6.27, 6.28 6.29 and 6.30 can we observe the effect from the change in material properties. As a reminder, D3 is the material properties defined in appendix A, while in D4 E and G are 25 % higher, in D5 they are 50 % higher and in D60 they are 60 times the values defined in appendix A. We can clearly observe the difference when applying different material properties. This is especially clear for the highest stiffness, D60. We can observe that for lower deadrise angles it is difficult see the difference. The effect from the stiffness is clearer at higher deadrise angles; at 22 degrees the difference is very clear. In figure 6.37 can we observe the same plot

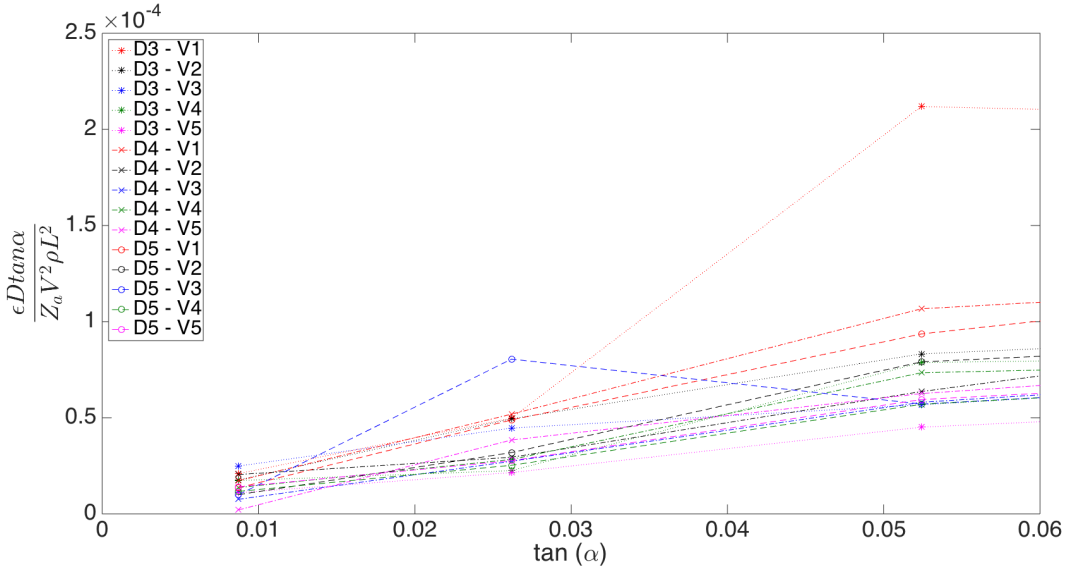

Figure 6.37: Results from the FSI-simulation series with different plate stiffness (D) with different impact velocities (V) and deadrise angles (α) - close up of the first three deadrise angles. D60 is not represented

as in figure 6.27 but it only displays the first three deadrise angles and D60 is removed. From this figure we can see the difference due to the change in stiffness at lower angles. The results are somewhat unclear but for most of them we can see that a lower structural stiffness increases the effect from hydroelasticity. This is in accordance with Bereznitski (2002). However, the observed effect is not very consistent and the trend appears somewhat scattered. One can conclude that the difference is less present at the smallest deadrise angles (0.5 degrees and 1.5 degrees), while clearer for higher deadrise angles. This is probably due to fact that higher deadrise angles have a lower geometrical stiffness and the material stiffness can therefore dominate. It is difficult to conclude anything for the other deadrise angles as the results vary from angle to angle.

Most of the results are in accordance with Bereznitski (2002) as a decrease in material stiffness leads to a higher importance of hydroelasticity. From figure 6.27 we can see that the results tend to converge when the deadrise angle is above 9 degrees; however, it is not near the calculated quasi-static value. We cannot conclude with certainty since R_B is below 2 while R_F suggests that the results almost should be considered quasi-static. R_B can be viewed in appendix C.

It also appears that the nondimentional strain converge to another value other than the calculated quasi-static nondimentional strain. An explanation might be that a sandwich composite shell has other load carrying mechanics than an ordinary metal plate and this will affect how the deformations and stresses are distributed and carried through the structure. In addition, the presented result is from a much more complex structure than a simple stiffened plate field which was studied in Faltinsen (1999b). Other effects will dominate and the results presented in Faltinsen (1999b) cannot be compared directly. Another aspect is the way the quasi-static strain is found. The quasi-static strain is found using strip plate beam theory; this might not be an ideal approach since the plate field in figure 6.1 is assumed to be as a plate field. The better option would be to map the pressure from the rigid CFD-solution directly onto the wet surface in Abaqus and find the quasi-static strain there.

When comparing figure 6.28 with the values of R_F it is clear that D60 should almost respond quasi-static as the value is very close to the limit defined in Faltinsen (1999b). It appears that this is not the case, as the values not yet have converged to anything close to the quasi-static value. However, they demonstrate the same trend as in figure 4.5. If we apply the theory in Bereznitski (2001) and equation 4.4, another story is told. The results from this approach can be seen in figure 6.38 and 6.39. As a reminder, a problem can be regarded quasi-static if $R_B > 2$. The load durations and ratios can be found in appendix C. The load duration is obtained from a series of rigid CFD-analysis as described in chapter 6.6.1. We can from figure 6.38 observe that all the simulations should be considered hydroelastic as R_B is at a maximum of 0.89. In figure 6.39 is it assumed that the plate responds hydroelastically (the stains are proportional to the velocity). The fit appears to be a much better when applying R_B. The decision factor R_B is more likely a better approach to explore when it is important to account for hydroelasticity than equation R_F, since the response have not yet converged to the quasi-static value even though R_F predicts that the response almost should be quasi-static. In addition, the method presented by Faltinsen (1999b) is applied on a plate field which limits it capabilities. The fact that Bereznitski (2001) gives a more correct method can be further explored in figure 6.39. The results appears much less scattered when applying R_B rather than R_F. Take particular note of the effect from higher R_B as the results tend to a response where the importance of hydroelasticity decreases. This is in accordance with Bereznitski (2001). This could indicate that R_B is the better approach to find the importance of hydroelasticity. We can in figure 6.40 observe the difference when the response is assumed to be quasi-steady. We can see that R_F yields a better fit, but as described above R_F states that the response almost should be quasi-static while this is obviously not the case since the values not yet have converged to the quasi-static value. Based on this one can conclude that the response is dominated by hydroelasticity and figure 6.39 shows the best way to compare the results. It appears that the theory by Faltinsen (1999b) underestimates the importance of hydroelasticity, and in this case, leads the user to believe that hydroelasticity is not important as the response almost should be quasi-static. The theory by Bereznitski (2001)

		0,5	1,5	3	9	14	22
D3	3,726	0,01	0,02	0,04	0,12	0,22	0,37
	5,589	0,01	0,02	0,03	0,07	0,13	0,25
	7,452	0,01	0,01	0,02	0,07	0,10	0,18
	9,315	0,01	0,01	0,02	0,06	0,09	0,15
	11,178	0,01	0,01	0,02	0,06	0,07	0,13
D4	3,726	0,02	0,02	0,04	0,12	0,23	0,39
	5,589	0,01	0,02	0,03	0,07	0,14	0,26
	7,452	0,01	0,02	0,02	0,07	0,11	0,19
	9,315	0,01	0,01	0,02	0,07	0,09	0,16
	11,178	0,01	0,01	0,02	0,06	0,07	0,13
D5	3,726	0,02	0,02	0,04	0,13	0,23	0,40
	5,589	0,01	0,02	0,03	0,08	0,14	0,27
	7,452	0,01	0,02	0,02	0,07	0,11	0,19
	9,315	0,01	0,01	0,02	0,07	0,10	0,16
	11,178	0,01	0,01	0,02	0,06	0,07	0,14
D60	3,726	0,03	0,04	0,07	0,23	0,41	0,71
	5,589	0,03	0,04	0,05	0,14	0,25	0,49
	7,452	0,02	0,03	0,04	0,13	0,20	0,34
	9,315	0,02	0,03	0,04	0,12	0,17	0,29
	11,178	0,02	0,02	0,04	0,11	0,13	0,24

Figure 6.38: The value of R_B when applying the theory in Bereznitski (2001). The different stiffnesses are marked in green, while the different dead rise angles are marked in yellow and placed horizontal, and the different velocities are yellow and placed vertical

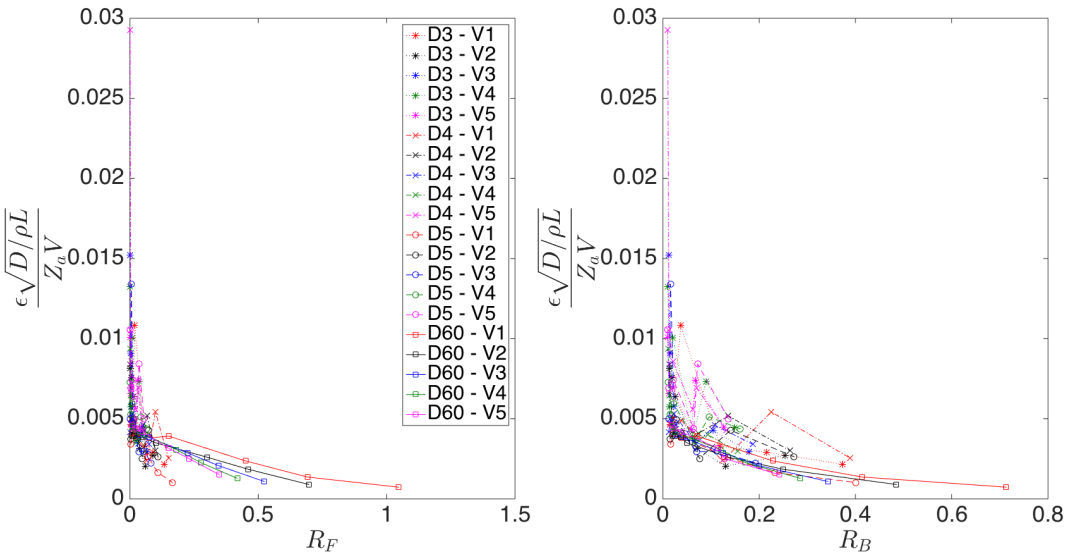

Figure 6.39: Results made dimensionless when assuming that the plate responds hydroelastic (Faltinsen, 1999b) and applying R_B (Bereznitski, 2001) to the right compared with R_F (Faltinsen, 1999b) to the left

still implies that the response should be hydroelastic. From the results it is understood that the response is still hydroelastic and hence is the theory by Bereznitski (2001) a more suited method.

One can argue if the assumptions in chapter 6.2.1 is correct. As stated above, it appear that the response is dominated by hydroelasticity and if this is the case is the assumption that the response is quasi-steady not valid. On the other hand, we can observe in figure 6.10 that the maximum strain appears when the average pressure is at a maximum and a short while after the maximum acceleration. After comparing several other simulations, it is concluded that this assumption is valid as they follow the same trend.

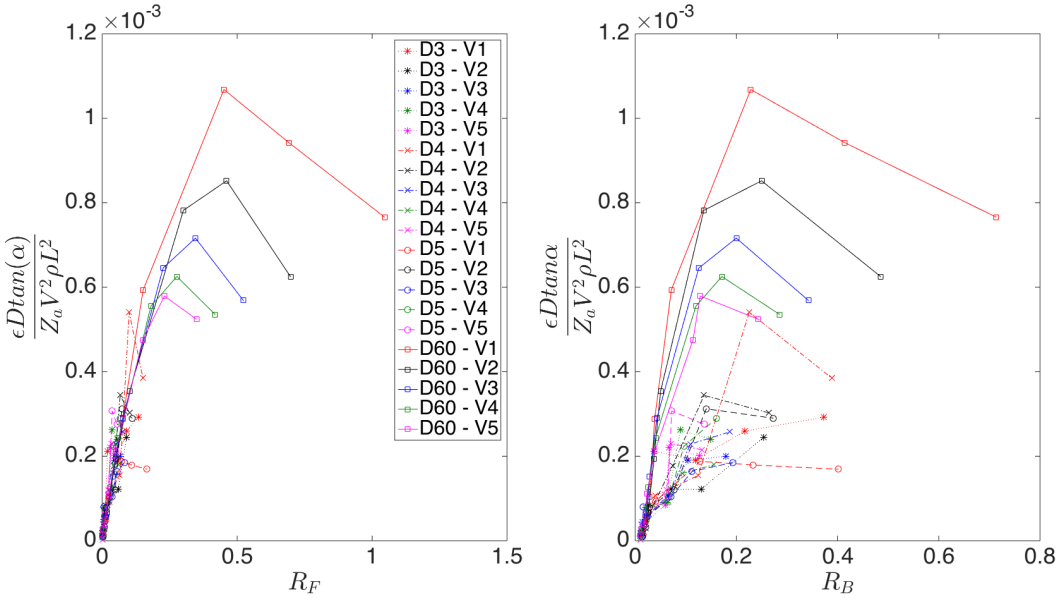

Figure 6.40: Results made dimensionless when assuming that the plate responds quasi-steadily (Faltinsen, 1999b) and applying R_B (Bereznitski, 2001) to the right compared with R_F (Faltinsen, 1999b) to the left

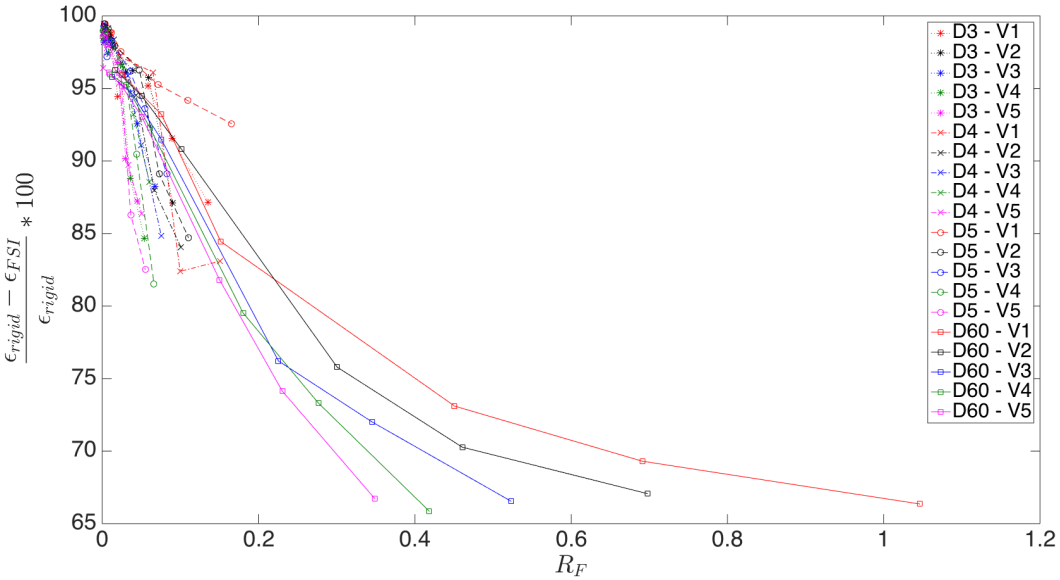

Figure 6.41: Difference between the quasi-static strain and the strain from the co-simulation applying R_F

In figure 6.41 we can see a plot comparing the strains from the quasi-static approach to the strains from an FSI-analysis with the decision factor R_F. The strains are compared in the following way:

$$\frac{\varepsilon_{\text{rigid}} - \varepsilon_{\text{FSI}}}{\varepsilon_{\text{rigid}}} 100 \tag{6.16}$$

This expresses the reduction in the strains due to hydroelastic response. As the response is in the FSI analysis gets more and more quasi-static, the reduction in strain will get lower. Hence, when

the hydroelastic simulation yields the quasi-static strain will the expression be equal to zero. This means that as the value from equation 6.16 gets lower, the importance of hydroelasticity will be reduced. We can observe in figure 6.41 that the value is at the lowest point about 66 % while R_F is about 1.1. If we look at figure 4.7, the response is regarded as quasi-static when the value from equation 6.16 is below 20 %. Based on this we understand that the response is not yet regarded as quasi-static. The value of R_F suggests that the response should almost be quasi-static, on the contrary, the results do not demonstrate that the response should almost be quasi-static. This demonstrates that R_F is not a suitable parameter to describe the importance of hydroelasticity on complex low rigidity structures.

From figure 6.28 we can observe that the simulation with stiffness D60, impact velocity V1 and a deadrise angle equal to $\alpha = 9$ degrees which is closest to the quasi-static value. It would therefore be interesting to see if the pressure plot yields the pressure oscillations associated with hydroelasticity. In figure 6.42, we can see the two pressure results. The pressure oscillations

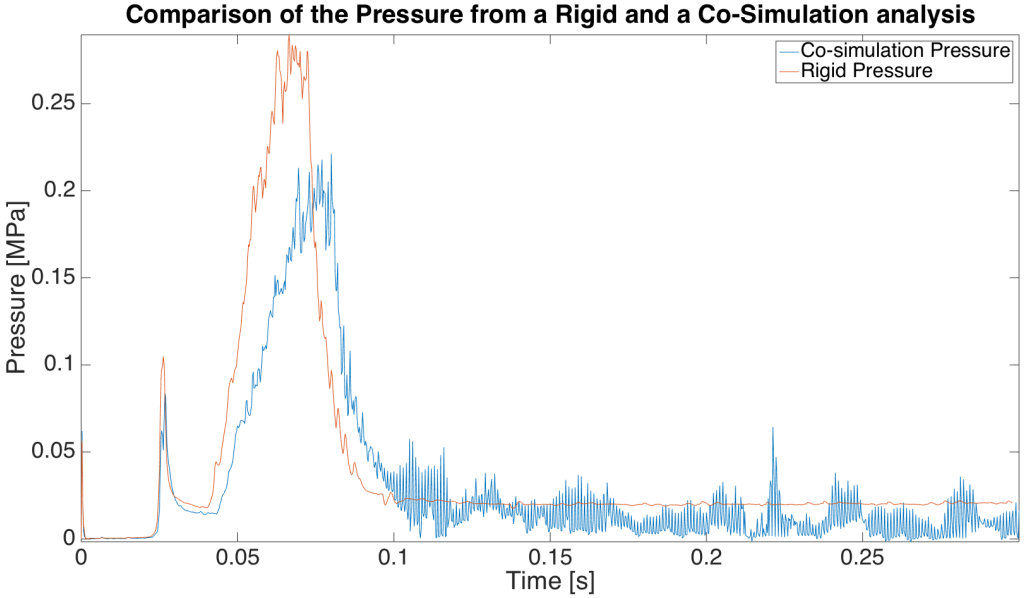

Figure 6.42: Comparison of the pressure from a rigid CFD analysis and a co-simulation which has a response which is the closest to quasi-static - the model has the stiffness D60, impact velocity V1 (3.726 $\frac{m}{s}$) and a deadrise angle equal to $\alpha = 9$ degrees

are not that evident as previously displayed in figure 5.33. However, they are present and the pressure is different; it is therefore believed that the simulation is still subject to hydroelasticity, but in a smaller degree. This was expected by the results in figure 6.28.

It should be noted that an FSI-analysis gives a lower structural stress compared to the quasi-static stress; the higher the influence of hydroelasticity, the lower the structural stress. This implies that if only the structural stress is of interest, a quasi-static approach is both faster and more conservative, but it is not able to correctly predict the pressure or the dynamic response of the hull. This is in accordance with Bereznitski (2001), where he demonstrated that a hydroelastic analysis might reduce the deformations by a factor of 10.

This chapter has tried to determine when it is important to account for hydroelasticity in nu-

merical simulations. It has not been easy, as numerical fluid-structure interaction analysis has shown to be very sensitive. It was demonstrated by Arai M. (1998) that finding the strain in a low rigidity structure was significantly more difficult than a high rigidity structure. Many simulations experienced failures and it had to be assumed that the plate response follows the dynamical loading in order to continue. The assumption was presented in Faltinsen (1999b) and was validated in figure 6.10. The trend in figure 6.28 is in good agreement with the trend in figure 4.5. This most likely demonstrates that the model is able to satisfactory recreate a hydroelastic event. The importance of hydroelasticity increases when the deadrise angle of the hull gets smaller and the impact velocity gets higher. The effect of stiffness is also studied, as we can see in figure 6.27 and 6.37. As expected is a lower structural stiffness associated with higher importance of hydroelasticity. This is also confirmed by Bereznitski (2002). However, it is not universal as the results sometimes show the contrary, but the majority of the results demonstrated this trend. The preferable way to decide when we should account for hydroelasticity is also discussed. It is concluded that the method presented in Bereznitski (2001) is the preferable method to discover when it is important to account for hydroelasticity. The method by Faltinsen (1999b) suggests that the response should almost be quasi-static, but this does not appear to be the case. While the method by Bereznitski (2001) suggests that all cases should be treated as hydroelastic, which is more in accordance with the presented results. The method by Bereznitski (2001) is regarded the preferred method to find the importance of hydroelasticity on complex low rigidity structures. Based on the presented results, it can be concluded that for a glass-fiber reinforced composite lifeboat it is important to account for hydroelasticity for all relevant analysis cases in this thesis. This is in accordance with Arai M. (1998) that a low rigidity structure shows has a higher degree of hydroelasticity. However, if only the structural stress is of interest in an e.g. ULS (Ultimate Limit State) analysis, a quasi-static approach will yield a quicker and more conservative result. If the response and pressure distribution is of interest, it is necessary to perform a FSI-analysis if a high quality result is required.

Chapter 7

Influence from Flow Separation

It is suspected that the flow separation might influence the results. This is mainly related to the separation point where the flow will separate from the hull of the lifeboat. As this might influence the result will it be studied using a rigid CFD-model.

7.1 CFD-model

The CFD-model is the same as the rigid model developed in chapter 5. The main difference lies in the selected physical model and the time step. The model is translated to 10 cm above the free surface in order to save computational time. The change in the physics model is related to the viscous regime. Previously in this thesis, only laminar flow regime has been used as this was investigated by Johannessen (2012) and he discovered that different flow regimes did not have a significant impact on the results. As the goal of this chapter is to examine the influence of flow separation, several different flow models will be tried in order to see if this would change the point of separation.

7.1.1 Flow Regime Model

Four different viscous regimes have been applied.

- Inviscid
- Laminar
- Turbulent - RANS with $\kappa - \omega$-model
- Turbulent - RANS with $\kappa - \varepsilon$-model

The inviscid approach is the most simple. The assumption here is that the inertia forces in the fluid are much greater than the viscous forces. Using this assumption the Navier-Stokes

equation is reduced to the Euler equation:

$$\rho\left(\frac{\partial}{\partial t}\vec{u}\nabla\right)\vec{u}+\nabla p=0 \tag{7.1}$$

If we in addition have an incompressible and irrational fluid can potential flow theory be applied.

Laminar flow is smooth and ordered. This type of flow occurs when the fluid flows in layers and no disturbance occurs between the layers. It is assumed that no disturbances are present in the fluid and that there are no eddies.

Turbulent flow is a highly disordered flow, which occurs at higher velocities and has velocity fluctuations. The interest in turbulent flow has led to the development of the Reynolds-Averaged Navier-Stokes (RANS) equation, which is used to model turbulence along with an additional turbulence model. In this equation are these velocity fluctuation averaged over the domain. There exists a vast number of different turbulence models. Two different models have been applied. Further details regarding the models will not be presented as this lies outside the scope of this thesis.

The decisional factor, for which flow regime is dominant is usually dictated by the Reynolds number $Re = \frac{VL}{\mu}$. Where V is the characteristic velocity, L is the characteristic length while μ is the kinematic viscosity.

7.1.2 Time Step

In order to assure that the simulation is able to capture the spray root properly, the time step has therefore been lowered. This is done due to the fact that the spray root moves quite fast. The new time step is set to $5.0 \cdot 10^{-6}$. This was done in order to ensure that the CFL-number was below 0.5 and to be able to capture the spray root and the free surface properly.

7.2 Results

Table 7.1: Results from the different simulation - Maximum and Average Pressure along the hull

Viscous Regime	$P_{\max}$ [MPa]	P_{avg} [kPa]
Inviscid	1.9123	43.686
Laminar	2.0507	46.460
$\kappa-\varepsilon$	2.3387	47.882
$\kappa-\omega$	2.3909	49.696

In figures 7.1, 7.2, 7.3 and 7.4 we can see the results from the comparison study. In figure 7.4, the top left is inviscid, top right is laminar, bottom left is turbulent flow with RANS and $\kappa-\varepsilon$-model and bottom right is turbulent flow RANS and $\kappa-\omega$-model. We can clearly see from figure 7.4 that the different flow regime models do not affect the separation point in a

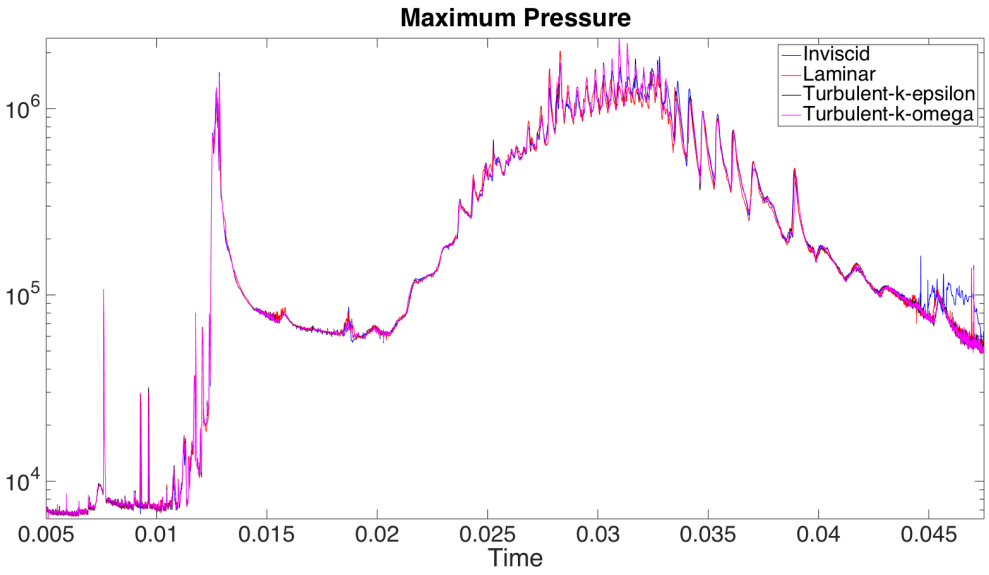

Figure 7.1: Maximum pressure along the hull when applying different viscous models

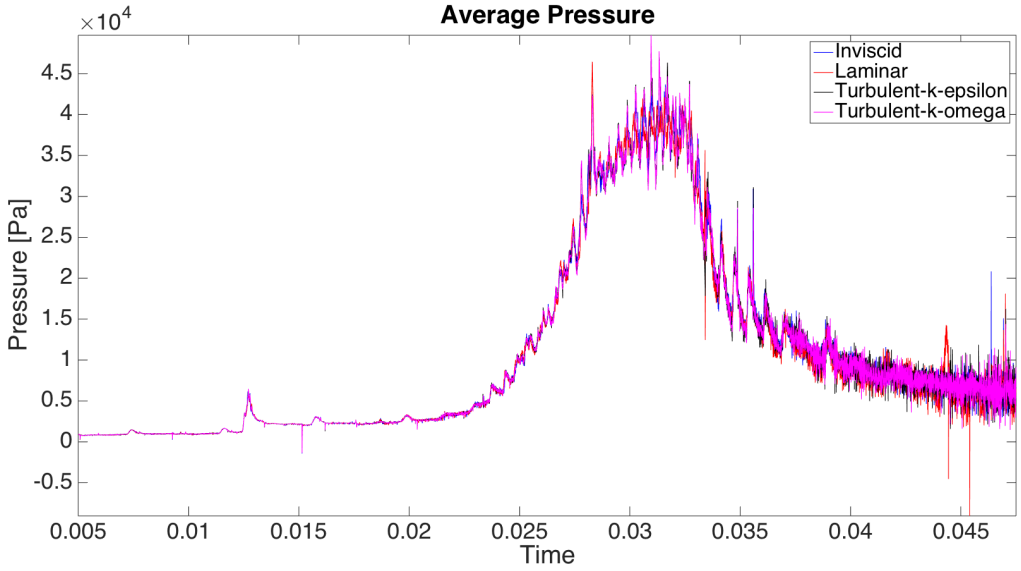

Figure 7.2: Average pressure along the hull when applying different viscous models

significant way. The flow follows the hull until the edge where the flow separates. This is logical as the section does not have a defined point of separation, until the edge that can be seen in the picture.

The effect from different viscous regimes is not very clear on the translation, velocity, or acceleration on the hull. This can be explained with that the pressure time history is fairly similar and only small differences in the magnitude of the pressure exist. One can see that the two turbulent flows yield a larger pressure than inviscid and laminar. This was also demonstrated by Johannessen (2012). In table 7.1, we can see the difference in maximum pressure along the hull. We can observe that the difference is 25 % from the simulation with inviscid flow to turbulent with $\kappa - \omega$ when we consider the maximum pressure along the hull. While for the surface, averaged

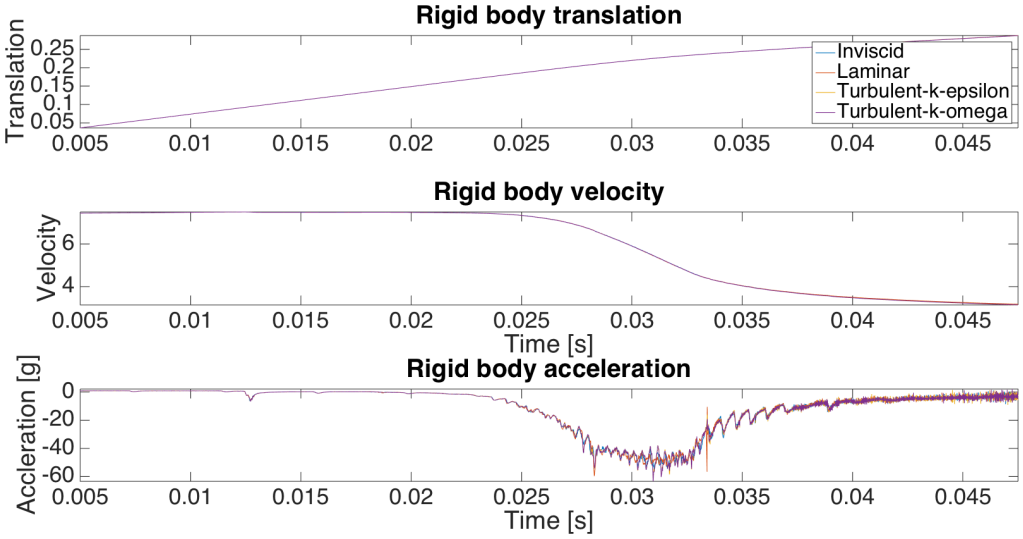

Figure 7.3: Translation, velocity and acceleration of the when applying different viscous models

pressure is the difference 13.8 %. For the laminar flow to turbulent with $\kappa - \omega$ is the difference in maximum pressure 16.5 %, while the difference in average pressure is 6.9 %. As explained in chapter 4.3 is the impulse of the load which is important in slamming. The average pressure is most significant for the impulse, hence is the difference between the two flow regimes is quite small and it is regarded that the difference is neglectable. This was also demonstrated in Johannessen (2012).

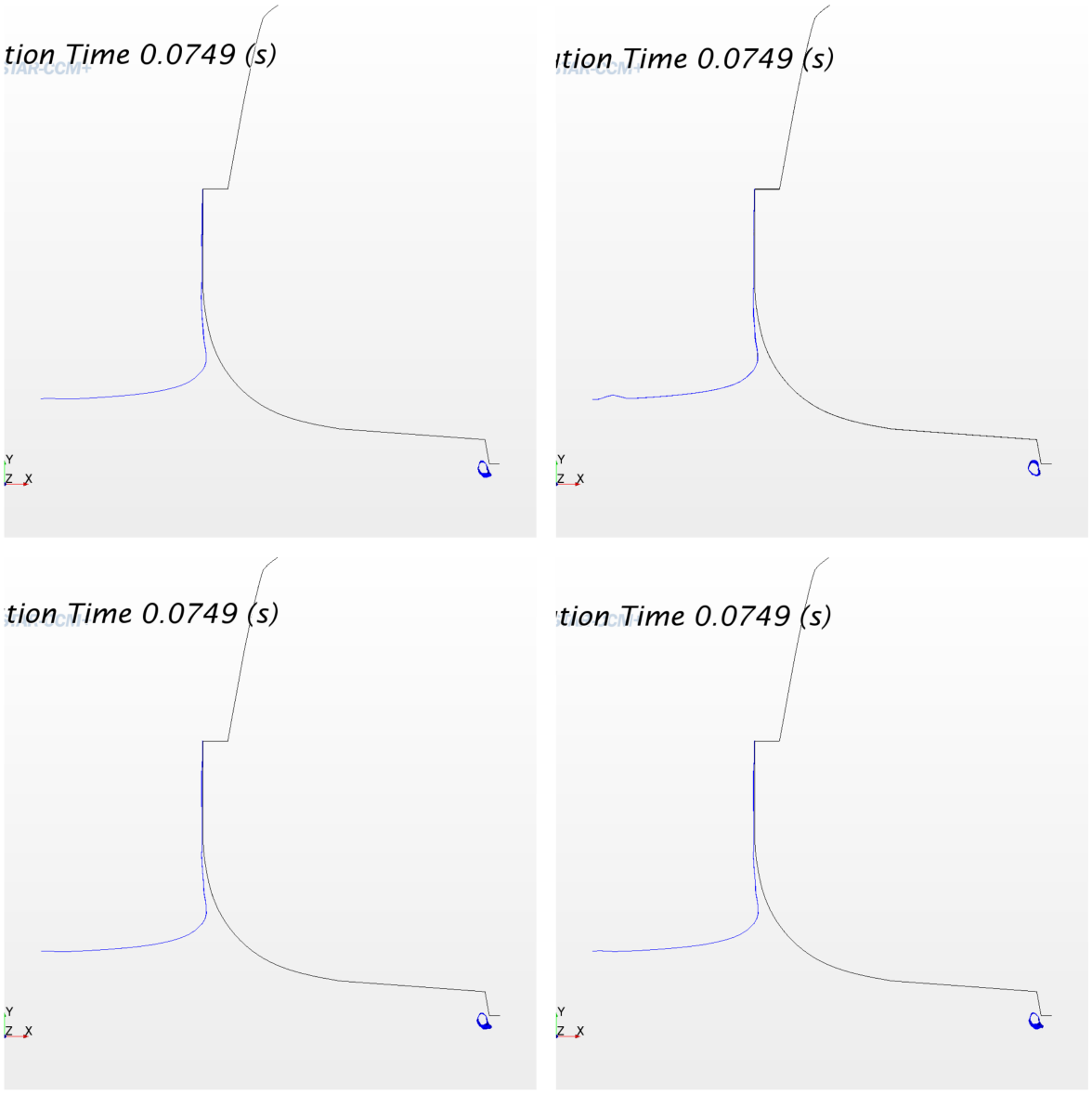

Figure 7.4: Snapshot of the hull and the free-surface at a $t = 0.0749$ s. Top left is inviscid, top right is laminar, bottom left is turbulent flow with $\kappa - \varepsilon$ and bottom right is turbulent flow with $\kappa - \omega$

Chapter 8

Conclusion

The importance of hydroelasticity has been studied in this thesis. A model was reduced from 3D to 2D. Additional mass and springs were applied in order to model effects from the 3D hull and full-scale test. The acceleration was measured in the full-scale test and the co-simulation model was able to recreate the time history of the acceleration in a good manner. Questions have been raised regarding the validity of the results, as the mass has been tuned by using the maximum acceleration from the full-scale results to find an equivalent 2D-mass. This was necessary due to the pressure distribution in 3D. On the contrary, the oscillation period was similar and the numerical and benchmark results followed each other closely after the point of maximum acceleration. It is concluded that the co-simulation model is able to recreate the full-scale test.

In the parametric study is the maximum strain in a plate examined. It was found that as the deadrise angle gets smaller and the impact velocity increases, the importance of hydroelasticity increases. In addition, it was observed that as the rigidity of the structure gets lower, the influence of hydroelasticity increases. These findings are in accordance with Bereznitski (2001), Bereznitski (2002) and Faltinsen (1999b). It can appear in the parametric study that the maximum strains have converged when the deadrise angle is above 9 degrees. However, they have not converged to the quasi-static value. The quasi-static strains is found using Euler-Bernoulli beam theory. Even though the parameter by Faltinsen (1999b) suggest that the response should almost be quasi-static.

The goal of this thesis is to obtain a parameter or decision factor that can be used to decide when we should account for hydroelasticity in numerical simulation of complex low rigidity structures. Several parameters have been explored and two were examined more closely. The decision factor R_B suggests that the response should be dominated by hydroelasticity, while the factor R_F leads the user to believe that the response almost should be quasi-static. The results shows that the response still is dominated by hydroelasticity - see figure 6.41 and 6.42. Indications that R_F is a less suited parameter is further explored in figure 6.41, here the reduction in the maximum strain is very high (65 %) even though R_F suggests that the response should almost be quasi-static (the reduction should be about 20 %). It was found that R_F is too specific and is probably better to use when studying pure plate fields. The parameter by Bereznitski (2001) is further explored in another parametric study.We observe in figure 6.33, 6.39 and 6.40

that as R_B increases, will the influence of hydroelasticity decrease, this is in accordance with Bereznitski (2001). In the three figures the strains are scaled in two different ways, as defined in Faltinsen (1999b). The results supports that R_B is the better suited decision factor to explore when it is important to account for hydroelasticity on complex low rigidity structures in numerical simulations. The limitation of this study is that a quasi-static response was not obtained, with respect to R_B, due to a combination of a short load duration and a high eigenperiod. This combination made it difficult to achieve a high enough ratio R_B to fully explore the parameter. It is also discussed that if the assumption that the response is quasi-steady is reasonable, since the respons have a better fit when scaled as hydroelastic. Figure 6.10 demonstrates that the quasi-steady assumption still is reasonable. It is also observed that the when the importance of hydroelasticity increases, the maximum strain in the plate decreases in relationship to the quasi-static strain. This can be seen in figure 6.41. This is of great interest as a quasi-static analysis can give a quick and conservative estimate.

Some concerns regarding the stability of the simulations have been raised. This is based on both a repetition study and sensitivity study. It was discovered that in the repetition study, the two simulation followed each other closely in the beginning of the simulation, but a while after impact they took different paths while the trend is very similar. The observed difference in maximum strain was at a maximum 17.9 %. An uncertainty analysis was performed and it was discovered that the uncertainty of the mean of nine repetition simulations was 10.8 % within a 95 % confidence interval. The reason for this is concluded to be the presence of non-linear geometry features or bifurcations points. This means that the structure might have several different equilibrium positions and can therefore take different response paths each time. In the sensitivity study, it was shown that a small change in initial velocity was amplified during the simulation and the difference in maximum strain was at a maximum 18.8 %. In addition, many of the co-simulation did experienced failures. This demonstrates the sensitive nature of numerical FSI analysis and that general care should be taken. It is concluded that the presence of bifurcation points, interaction with the eigenmodes of the springs and the capabilities of the dynamic implicit solver in Abaqus are the main contributors to the instabilities. The difference appears during the free vibration phase, when the plate experiences fast vibrations. The chosen Abaqus solver may not be able to capture these fast vibrations or the present of bifurcation points can lead the structure to take a different path. These aspects in combination are probably the reason why the simulations are not consistent. Possible solutions have been presented and the best could be to change to an dynamic explicit solver. However, this would cause the loss of the implicit coupling which is not beneficiary for the co-simulation. As discussed in chapter 4.3, it has been shown that there exists a variance among the measured strain for a given impact velocity. This means that it can be expected that there exists a slight difference in the maximum strain when repetition is performed. It is therefore regarded that the model is able to describe a hydroelastic event satisfactory.

The influence of flow separation was explored. It was believed that the point of separation might alter the results. A series of simulations were performed with different flow models in Star-CCM+. The time step was altered in order to ensure that the numerical simulation was able to capture the spray root properly. The different flow models were two turbulent flows (RANS with $\kappa - \omega$-model and RANS with $\kappa - \varepsilon$-model), laminar and inviscid. It is concluded

that the point of flow separation is not affected by different viscous models as the flow follows the hull and only separates at the edge. The effect of different viscous regimes is not very clear on the translation, velocity or acceleration on the hull. This can be explained with that the pressure time history is fairly similar and only small differences in the magnitude of the pressure exists. The change in pressure from laminar to turbulent ($\kappa - \omega$) is not significant enough when considering the slamming response since it is the impulse that is important and the difference in average pressure is only 6.9 %. It is concluded that the difference can be dismissed and laminar is a suitable viscous model for this problem.

Chapter 9

Further Work

The reduction from 3D to 2D has yielded some problems. The problems are mainly related to the additional mass and the applied springs. The springs are probably one of the reasons for the observed instabilities as they interact dynamically during impact. For a future thesis it would be interesting to see if these problems would disappear if a fluid-structure interaction analysis is performed using a complete 3D model. It can be expected that the moment of inertia is not properly distributed, hence would the model not land completely flat as expected in this thesis. In addition, a complete 3D model could discover if the combination of Star-CCM+ and Abaqus is able to recreate a full-scale test without modifying the model. This thesis has its limitations as the mass have been tuned by utilizing the full-scale results.

A more suitable way to obtain the quasi-static strains should also be explored. In this thesis, plate beam theory from Faltinsen (1999b) has been applied. A better way would be to use the pressure from the rigid CFD analysis and export this to Abaqus. This was tried without success and should be further explored.

It could be interesting to apply a one-way approach to a hydroelastic problem in order to see how different the results would be. A series of different values of R_B should be analyzed with both a one-way and a two-way interaction method. With this approach, one can observe how this would affect the obtained results and if a one-way interaction method could be used at an earlier point than expected in this thesis ($R_B > 2$). This is regarded as an exploration of the procedure defined in figure 4.8. This is regarded as important; as the procedure appears for the author to be a good procedure to decide when to account for hydroelasticity.

One other question that arises, is if we can use a one-way interaction method when the response is regarded quasi-static or if we should use a two-way interaction method with a weak coupling. It should be further explored in order to investigate how we can simplify the problem when the response is regarded quasi-static.

A sufficiently high ratio of R_B was not achieved. A series of simulations should be constructed such that the ratio is sufficiently high - up to three. This can reveal if $R_B > 2$ is a necessary limit for when we could neglect hydroelasticity for a complex low rigidity structure.

In addition, it will be important to explore how the load duration of the rigid CFD analysis

is found. The hydrodynamic force along the hull has been utilized in this thesis. The results probably would be different if a different parameter (pressure or acceleration) had been applied. An obvious improvement in this thesis would be to use the load duration from the co-simulation, (Bereznitski, 2001). It would therefore be interesting to see how this would alter the ratio.

It would also be interesting to see what differences would occur, if the improvements that are mentioned in chapter 6.7 were introduced. This is mainly related to the increase in the number of springs and the way the spring stiffness constant is found. A higher number of springs would be an obvious improvement. Since non-linear interaction effects most likely exist, it would be more correct to apply several different loads. The resulting stiffness constant could be the mean of the obtained values or we could apply a non-linear spring. In addition, it would be interesting to see the difference when applying a dynamic explicit step in Abaqus, instead of a dynamic implicit. However, this would result in the loss of the implicit coupling. Which according to CD-Adapco (2014) is not beneficiary.

It should be noted that Abaqus and Star-CCM+ both have the possibility to perform FSI analysis within the code itself. This has not been explored by the author, but it is believed that they have some limitations. This is something that can be further explored, as this might reduce the instability in the co-simulation engine itself.

Bibliography

Aagaard, O. (2013). Hydroelastic analysis of flexible wedges. (June).

Arai M., M. T. (1998). Numerical study of the impact of water on cylindrical shell, considering fluid-structure interaction. *Practial design of ships and mobile units - Development in Marine Technology*, 11.

Bereznitski, A. (2001). Slamming: The role of hydroelasticity. *International Shipbuilding Process*, 48.

Bereznitski, A., K. M. (2002). Practical implications of hydroelasticity in ship design.

Blazek, J. (2005). *Computational fluid dynamics: principles and applications*. Amsterdam - Elsevier.

Bloxom, Andrew L., N. W. L. (2012). Fluid-structure interaction of a surface effect ship bow seal and a free surface. *Aerospace and Ocean Engineering, Virginia Tech*.

Causin, P., G. J. N. F. (2005). Added-mass effect in the design of partitioned algorithms for fluid–structure problems. *Computer Methods in applied mechanics and engineering*, 194.

CD-Adapco (2014). Star-ccm+ documentation.

Cengel, Yunus A., C. J. M. (2010). *Fluid Mechanics: Fundamentals and Applications, Second Edition in SI units*. McGraw Hill.

Dejhalla, R. (2006). A review of the state-of-the-art in marine hydrodynamics.

Faltinsen, O. (1999a). *Sea Loads on Ships and Offshore Structures*. Cambridge University Press.

Faltinsen, O. (2005). *Hydrodynamics of High-Speed Marine Vehicles*. Cambridge University Press.

Faltinsen, O. M. (1999b). Water entry of a wedge by hydroelastic orthotropic plate theory. *Journal of Ship Research*, 43.

Faltinsen, O. M. (2000). Hydroelastic slamming.

Fedem (2011). Slamming capacity - ***** boat.

Fish, J. and Belytschko, T. (2007). *A First Course in Finite Elements*. John Wiley and Sons, Ltd.

Forster, C., W. W. R. E. (2006). The artificial added mass effect in sequential staggered fluid-structure interaction algorithms. *European Conference on Computational Fluid Dynamics*.

Gere, J. and Timoshenko, S. (1997). *Mechanics of Materials*. PWS Publishing Company.

Gorski, J. (2001). Present state of numerical ship hydrodynamics and validation experiments. *OMAE 2001*.

Greco, M. (2012). Lecture notes in sea loads.

Haidari, Ahmad, M. B. (2013). Future trends for computational fluid dynamics in the process industry. *CFD in the Minerals and Process Industies*.

Handeland, M. P. (2014). Project thesis - importance of fluid-structure interaction on free-fall lifeboats. *NTNU - Department of Marine Technology*.

Johannessen, S. R. (2012). Use of cfd to study hydrodynamic loads on free-fall lifeboats in the impact phase. *Master Thesis, NTNU*.

Kapsenberg, G. K. (2011). Slamming on ships: where are we now? *Philophical Transactions of The Royal Society*.

Khabakhpasheva, T. and a.a. Korobkin (2013). Elastic wedge impact onto a liquid surface: Wagner's solution and approximate models. *Journal of Fluids and Structures*, 36:32–49.

Kyriazoglou, C., G. F. (2007). Finite element prediction of damping of composite gfrp and cfrp laminates – a hybrid formulation – vibration damping experiments and rayleigh damping. *Composites Science and Technology*.

Langen, I. and Sigbjornsson, R. (1986). *Dynamisk Analyse av Konstruksjoner*. Fagbokforlaget.

Larsen, E. (2013). Impact loads on circular cylinders. (June).

Lomax, H., P. T. and Zingg, D. (1999). *Fundamentals of Computational Fluid Dynamics*.

Luo, H. and Wang, H. (2014). Comparative study of hydroelastic impact for one free-drop wedge with stiffened panels by experimental and explicit finite element methods. *OMAE 2011*, (2006):1–9.

Ma, S. and Mahfuz, H. (2012). Finite element simulation of composite ship structures with fluid structure interaction. *Ocean Engineering*, 52:52–59.

Maki, K. J., Lee, D., Troesch, A. W., and Vlahopoulos, N. (2011). Hydroelastic impact of a wedge-shaped body. *Ocean Engineering*, 38(4):621–629.

Marintek (2011). Acceleration tests for the conventional lifeboat *******.

Moan, T. (2003). *TMR4190 - Finite Element Modeling and Analysis of Marine Structures*. NTNU - Institutt for Marin Teknikk.

Panciroli, R., G. M. (2005). Hydroelastic slamming of composite plates.

Panciroli, R. (2012). Water entry of flexible wedges: Some issues on the fsi phenomena. *Applied Ocean Reasearch*, 39:72–72.

Panciroli, R. (2013). *Hydroelastic Impacts of Deformable Wedges*, volume 192 of *Solid Mechanics and Its Applications*. Springer Netherlands.

Panciroli, R., Abrate, S., and Minak, G. (2013). Dynamic response of flexible wedges entering the water. *Composite Structures*, 99:163–171.

Panciroli, R., Abrate, S., Minak, G., and Zucchelli, A. (2012). Hydroelasticity in water-entry problems: Comparison between experimental and sph results. *Composite Structures*, 94(2):532–539.

Piro, D. J. and Maki, K. J. (2013). Hydroelastic analysis of bodies that enter and exit water. *Journal of Fluids and Structures*, 37:134–150.

PTIL (2014). `http://www.ptil.no/livbaater/category856.html`,`http://www.ptil.no/livbaater/hoeringsfrist-i-livbaatsaken-article10879-856.html`,`http://www.ptil.no/beredskap/livbaatene-lang-kamp-for-trygg-evakuering-article7654-854.html`.

Rosis, A. D., Falcucci, G., Porfiri, M., Ubertini, F., and Ubertini, S. (2014). Hydroelastic analysis of hull slamming coupling lattice boltzmann and finite element methods. *Computers & Structures*, 138:24–35.

Safety, O. W. (2015). `http://www.oceanwidesafety.nl/news/archive/10-years-ocenwide-safety-at-sea.html`.

Shim, V.P.M., T. Z. L. C. (1999). Two-dimensional response of crushable polyurethane foam to low velocity impact. *International Journal of Impact Engineering*, 24:703–731.

Steen, S. (2014). *Lecture Notes: Experimental Methods in Marine Hydrodynamics*. Department of Marine Technology.

Vinson, J. R. (1999). *The Behavior of Sandwich Structures of Isotropic and Composite Materials*. CRC Press.

Yettou, E.-M., Desrochers, A., and Champoux, Y. (2006). Experimental study on the water impact of a symmetrical wedge. *Fluid Dynamics Research*, 38(1):47–66.

Yettou, E.-M., Desrochers, a., and Champoux, Y. (2007). A new analytical model for pressure estimation of symmetrical water impact of a rigid wedge at variable velocities. *Journal of Fluids and Structures*, 23(3):501–522.

Zienkiewicz, O. C., Taylor, R. L., and Nithiarasu, P. (2013). *The Finite Element Method for Fluid Dynamics, Seventh Edition*. Butterworth-Heinemann.

Appendix A

Material Properties in FEM-model

Table A.1: Material properties

	E_x	E_y	E_z	ν_{xy}	ν_{yz}	ν_{xz}	G_{xy}	G_{yz}	G_{xz}	ρ	α	β
Spray Laminate	8100	8100	5000	0.30	0.30	0.30	3115	1500	1500	1560	0.21	[-]
CSM	8500	8500	5000	0.30	0.30	0.30	3269	1500	1500	1560	0.21	[-]
UD E-glass	26800	5400	5400	0.28	0.28	0.28	2400	1500	1500	1750	0.21	[-]
Buoyancy Foam	5	5	5	0.4	0.4	0.4	[-]	[-]	[-]	30	[-]	0.001

E is Young's modulus [MPa], ν is Poisson ratio, G is the shear modulus [MPa], ρ is the density [$\frac{kg}{m^3}$], α is the mass damping coefficient and β is the stiffness damping coefficient in the Rayleigh damping model.

Appendix B

Quasi-Static Pressure

Pa	0.5	1.5	3	9	14	22
V1	1156653	696562	350502	172623	106695	65017
V2	1818385	1295853	795923	315863	224034	122002
V3	2510231	1866336	1249158	471840	355551	194184
V4	3201347	2709651	1813218	736455	508946	280030
V5	4026555	3374387	2512938	1021043	700426	405166

Figure B.1: Space-averaged pressure over the plate, when the space-averaged pressure on the hull is at maximum. From rigid CFD analysis of the models applied in the parametric study

Appendix C

Load Duration and Ratio

	Duration						
		0.5	1.5	3	9	14	22
	3.726	0.005	0.00675	0.0125	0.04	0.0725	0.125
	5.589	0.0045	0.0065	0.00875	0.02375	0.04375	0.085
	7.452	0.004	0.005	0.0075	0.022	0.035	0.06
	9.315	0.0035	0.0045	0.007	0.021	0.03	0.05
	11.178	0.00325	0.004	0.00675	0.02	0.0225	0.0425
Ratio							
		0.5	1.5	3	9	14	22
D3	3.726	0.014916	0.020137	0.03729	0.119328	0.216282	0.3729
	5.589	0.013424	0.019391	0.026103	0.070851	0.130515	0.253572
	7.452	0.011933	0.014916	0.022374	0.06563	0.104412	0.178992
	9.315	0.010441	0.013424	0.020882	0.062647	0.089496	0.14916
	11.178	0.009695	0.011933	0.020137	0.059664	0.067122	0.126786
D4	3.726	0.015545	0.020985	0.038861	0.124356	0.225395	0.388613
	5.589	0.01399	0.020208	0.027203	0.073836	0.136014	0.264257
	7.452	0.012436	0.015545	0.023317	0.068396	0.108812	0.186534
	9.315	0.010881	0.01399	0.021762	0.065287	0.093267	0.155445
	11.178	0.010104	0.012436	0.020985	0.062178	0.06995	0.132128
D5	3.726	0.016039	0.021652	0.040096	0.128308	0.232558	0.400963
	5.589	0.014435	0.02085	0.028067	0.076183	0.140337	0.272655
	7.452	0.012831	0.016039	0.024058	0.070569	0.11227	0.192462
	9.315	0.011227	0.014435	0.022454	0.067362	0.096231	0.160385
	11.178	0.010425	0.012831	0.021652	0.064154	0.072173	0.136327
D60	3.726	0.028533	0.038519	0.071331	0.22826	0.413721	0.713313
	5.589	0.025679	0.037092	0.049932	0.135529	0.249659	0.485053
	7.452	0.022826	0.028533	0.042799	0.125543	0.199728	0.34239
	9.315	0.019973	0.025679	0.039946	0.119837	0.171195	0.285325
	11.178	0.018546	0.022826	0.038519	0.11413	0.128396	0.242526

Figure C.1: Load duration and ratios based upon D3, D4, D5 and D60 over the different velocities and deadrise angles

Appendix D

Importance of Hydroelasticity for D60

0,5	11,178	9,315	7,452	5,589	3,726
7195,8	0,008435	0,010122	0,012653	0,016871	0,025306

1,5	11,178	9,315	7,452	5,589	3,726
7195,8	0,025301	0,030361	0,037951	0,050602	0,075902

3	11,178	9,315	7,452	5,589	3,726
7195,8	0,050558	0,060669	0,075836	0,101115	0,151673

9	11,178	9,315	7,452	5,589	3,726
7195,8	0,150289	0,180347	0,225434	0,300579	0,450868

14	11,178	9,315	7,452	5,589	3,726
7195,8	0,230362	0,276435	0,345543	0,460724	0,691086

22	11,178	9,315	7,452	5,589	3,726
7195,8	0,348691	0,418429	0,523036	0,697381	1,046072

Figure D.1: Importance of hydroelasticity for D60 over the different velocities and deadrise angles from equation 4.2

Appendix E

FFT of Acceleration Time History of the FSI-analysis and Test Results

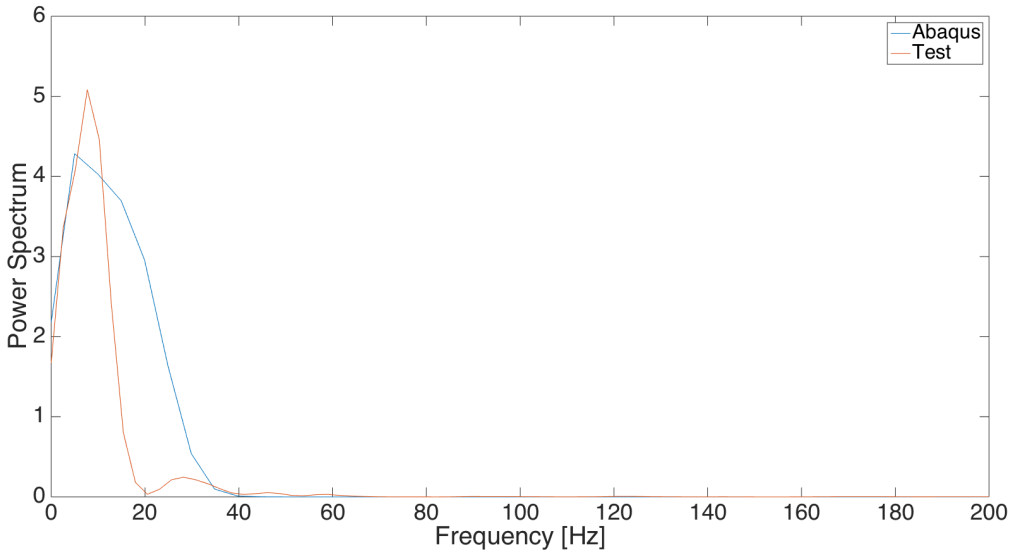

Figure E.1: Power spectrum of the acceleration time series from the FSI simulation and the benchmark test

Appendix F

Comparison between the obtained Acceleration in the FSI-analysis and Rigid CFD-analysis

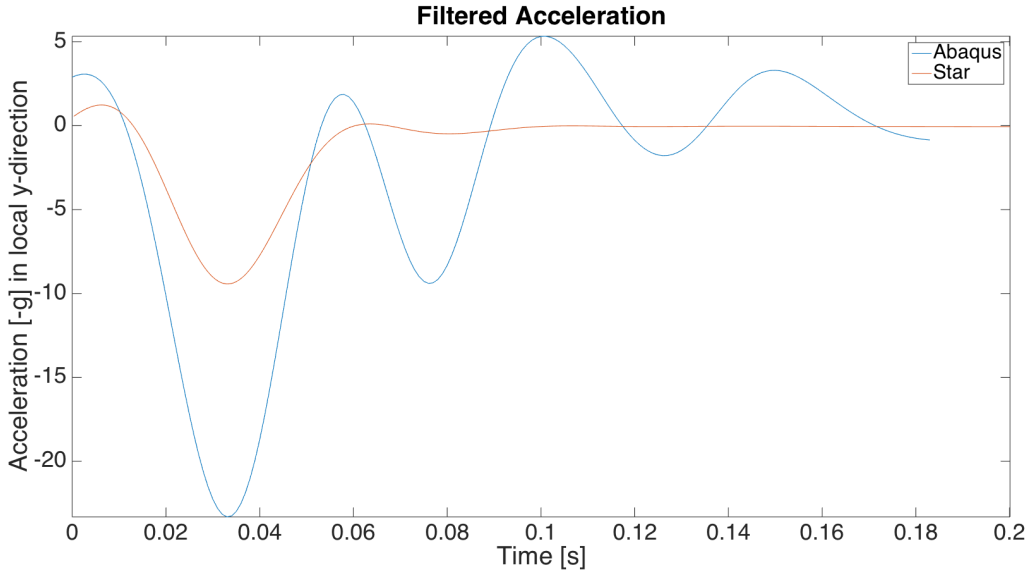

Figure F.1: Comparison of the acceleration in local Y-direction between FSI analysis and rigid analysis

Appendix G

Nine Repetition Simulations

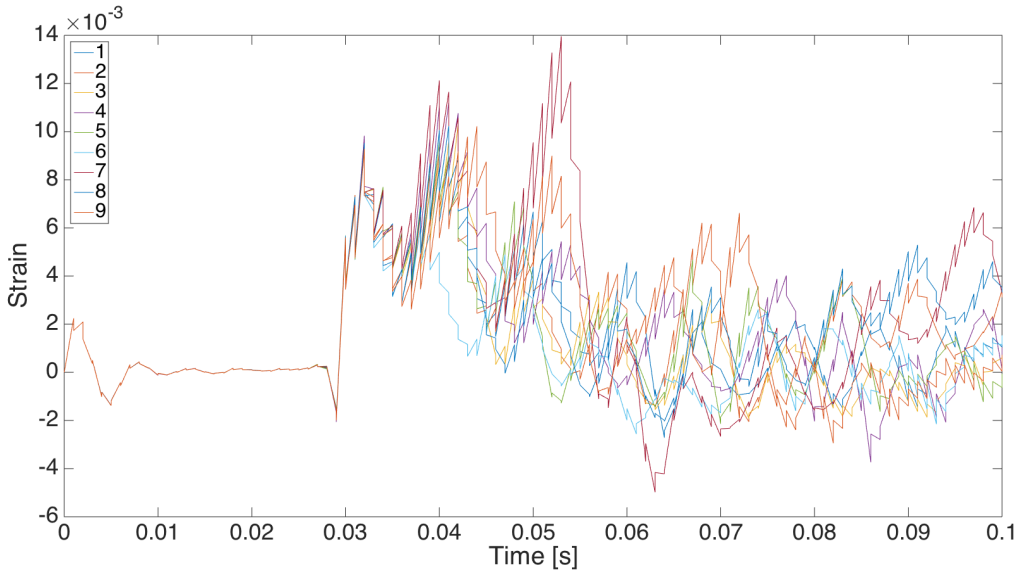

Figure G.1: Strain time history for nine repetition simulations

Appendix H

Electronic Appendix

Table H.1: Content in the attached zip-file

Poster
Star-CCM+ and Abaqus model used in chapter 5
Star-CCM+ and Abaqus model used in chapter 6
Abaqus input files used in chapter 6
Star-CCM+ simulation files used in chapter 7